Radiation Field in Low Earth Orbit: Measurements from MATROSHKA DOSTEL onboard ISS

Dissertation
zur Erlangung des Doktorgrades
der Mathematisch-Naturwissenschaftlichen-Fakultät
der Christian-Albrechts-Universität zu Kiel

vorgelegt von
Johannes Labrenz

Kiel, 2014

Referent/in: Prof. Dr. Bernd Heber

Koreferent/in: Prof. Dr. Sebastian Wolf

Tag der mündlichen Prüfung: 30.06.2014

Zum Druck genehmigt: 30.06.2014

gez. Prof. Dr. Wolfgang J. Duschl, Dekan

Zusammenfassung

Die Erde ist kontinuierlich der Galaktischen Kosmischen Strahlung (GCR) ausgesetzt. Die GCR besteht aus geladenen Teilchen, welche durch das Erdmagnetfeld und die Erdatmosphäre abgeschirmt werden, so dass sie für Menschen auf dem Erdboden nur zu einer geringen und damit zu vernachlässigenden Strahlenexposition führen. Verlässt man die schützende Erdatmosphäre steigt die Strahlenexposition durch die kosmische Strahlung an, was dazu führt, dass diese nicht mehr zu vernachlässigen ist und für Astronauten auf der internationalen Raumstation (ISS) deshalb von besonderer Bedeutung ist.
Das MATROSHKA Experiment hat sich zur Aufgabe gemacht die Strahlenexposition für Menschen auf der ISS möglichst genau zu bestimmen und hat zu diesem Zweck ein Phantom des menschlichen Oberkörpers mit Strahlungsdetektoren versehen und auf die ISS bringen lassen. Einer der Strahlungsdetektoren des MATROSHKA Experiments ist das DOSimetric TELescope (DOSTEL). Dieses aktive Instrument besteht aus Silizium Halbleiterdetektoren und ist in der Lage eine zeitaufgelöste Vermessung des Strahlungsfeldes auf ISS Flughöhen durchzuführen. Während der beiden MATROSHKA Experimentphasen MTR-1 und MTR-2B hat das DOSTEL Instrument außerhalb und innerhalb der ISS Daten aufgenommen. Die DOSTEL Messungen haben gezeigt, dass die Intensität der GCR Teilchen kaum durch die Hülle der ISS abgeschirmt wird und hauptsächlich von der solaren Modulation der GCR abhängig ist. Außerdem konnte die Winkelverteilung der GCR Teilchen mit Hilfe der DOSTEL Messungen abgeschätzt werden. Neben den GCR Teilchen tragen auch geladene Teilchen, welche im Erdmagnetfeld in den sogenannten Strahlungsgürteln gefangen sind, zur Strahlenexposition bei. Die Außenhaut der ISS schirmt diese Teilchen effektiv ab, so dass die Strahlenexposition durch diese Teilchen innerhalb der ISS deutlich geringer ist. Während der Messungen außerhalb der ISS konnte zudem eine Störung des Strahlungsfeldes auf ISS Höhen festgestellt werden. Im Juli 2004 wurde das Erdmagnetfeld mit relativistischen Elektronen gefüllt, welche einen quasi-stabilen Strahlungsgürtel bildeten. Die zusätzliche Strahlenexposition durch dieses zeitlich begrenzte Phänomen wurde mit DOSTEL bestimmt und lieferte damit wichtige Erkenntnisse zur Interpretation der Messwerte der passiven MATROSHKA Detektoren.

Abstract

The Earth is permanently exposed to Galactic Cosmic Radiation (GCR). The GCR consist of charged particles and are effectively shielded by Earth's magnetic field and atmosphere. Therefore the radiation exposure on ground is insignificant, but becomes important when leaving the protective atmosphere. Due to the increased radiation exposure, radiation protection is an important field for space exploration.

The MATROSHKA experiment was performed to investigate the radiation exposure to humans on the International Space Station (ISS). An anthropomorphic upper-torso phantom equipped with radiation detectors, named after the Russian nesting doll, was brought to space to perform measurements outside and inside the ISS. One of MATROSHKA's radiation detectors is the DOSimetric TELescope (DOSTEL), which is based on Silicon semiconductor technology. This active instrument allows a time resolved measurement of the radiation field at ISS altitudes.

DOSTEL measurements have shown that the spacecraft hull has only a minor effect on the intensity of GCR particles. The radiation exposure mainly depends on the solar modulation of the GCR. Furthermore, the angular distribution of the GCR particles could be estimated by using data obtained with DOSTEL.

Besides GCR particles, particles trapped in Earth's magnetic field in the so-called radiation belts contribute to the radiation exposure. These particles are effectively shielded by the ISS spacecraft hull, and thus, their contribution to the radiation exposure decreases for inside measurements.

During the outside measurement, DOSTEL observed a disturbance of the radiation field at ISS altitudes. In July 2004 Earth's magnetic field was filled with relativistic electrons. The electrons formed a quasi stable radiation belt in the slot region which was observable until November 2004. The additional radiation exposure induced by this temporal phenomenon was estimated and led to important scientific findings, which were necessary for the interpretation of the results of the other MATROSHKA detectors.

Contents

List of Acronyms

ADC	Analogue to Digital Converter	31
CAU	Christian-Albrechts-Universität	26
CIR	Co-rotating Interaction Region	12
CME	Coronal Mass Ejection	7
CSA	Charge Sensitive Amplifier	29
CRAND	Cosmic Ray Albedo Neutron Decay	14
DLR	German Aerospace Center	25
DST	Disturbance Storm Time	12
DOSTEL	Dosimetry Telescope	2
ESA	European Space Agency	2
GCR	Galactic Cosmic Ray	3
ICRP	International Commission of Radiation Protection	
IGRF	International Geomagnetic Reference Field	8
ISS	International Space Station	1
LEO	Low Earth Orbit	3
LET	Linear Energy Transfer	22
MIP	Minimal Ionizing Particle	66
MTR	MATROSHKA	
NASA	National Aeronautics and Space Administration	
PCMCIA	Personal Computer Memory Card International Association	
PIPS	Passivated Implanted Planar Silicon	
$\mathbf{R}_c$	Effective Vertical Geomagnetic Cutoff Rigidity	9
SAA	South Atlantic Anomaly	8
SAMPEX	Solar Anomalous and Magnetospheric Particle Explorer	91
SEP	Solar Energetic Particle	5
SRB	Slot Region Belt	93
TLD	Thermo Luminescent Detector	26

1. Introduction

Space exploration has always been and still is a challenging task for humans. To protect astronauts from the harsh environment in space, spacecraft provide Earth-like atmosphere and temperatures. But vacuum, low temperatures, microgravity, and not to forget psychological effects, are not the only health threats when it comes to manned space research – another force to deal with is cosmic radiation.

Even here on Earth humans are permanently exposed to cosmic radiation. Although this low level exposure of $\sim 0.8\,\frac{\mu Sv}{day}$ is generally not considered as harmful, ionizing radiation is proven to be capable of causing cellular DNA damages, i.e., heavy ions can cause DNA double strand breaks. The human body has a repairing mechanism for these kinds of damages, but unfortunately errors can occur during this DNA repairing process. These errors can result in cell death or in defective DNA which can cause harmful stochastic effects, better known as cancer for example. The probability of stochastic effects depends on the amount of DNA damage, which in turn depends on the dose of ionizing radiation.

Short time exposure with high radiation doses often leads to visible and sometimes even harmful deterministic effects such as radiation sickness, erythrodermia and anemia. The effects result from a significant amount of dead cells in the region of the exposure. The limit for deterministic radiation damage lies within 500 mSv during short time exposure, below this point an acute radiation damage is unlikely. However, the probability of stochastic effects increases with any exposure. Because the intensity of cosmic radiation increases with higher altitudes, radiation monitoring is of importance for air- and space-crews. Earth's atmosphere has a strong shielding effect against cosmic radiation, but once leaving the atmosphere the exposure to cosmic radiation is a grave danger for astronauts. Besides the APPOLO missions, most manned space flights have been performed in Low Earth Orbit (LEO). During the last decade the common destination of these flights has been the International Space Station (ISS). This manned space station is funded by international partners and has been continuously occupied since 2000. It is operating at a mean altitude between 330 km and 400 km with an orbit inclination of 51.6° and an orbital time of 91 minutes. The altitude decreases in time and the ISS has to be lifted back to higher altitudes by use of Space Shuttle engines (during the shuttle era) or by other support vehicles such as the Automated Transfer Vehicle (ATV) from the European Space Agency (ESA), for example. A detailed description of the ISS can be found on the official NASA website (www.nasa.gov/mission_pages/station/main). A photograph of the ISS from year 2004 can be seen in figure 1.1.

Figure 1.1.: Photograph of the ISS from 2004. Picture courtesy of NASA.

For a better understanding of radiation exposure in general and radiation exposure on the ISS in particular, the MATROSHKA experiment was conducted. An anthropomorphic upper-torso phantom was equipped with detectors and used as a simulated human body for measurements of the radiation exposure inside and outside the ISS. One of the used radiation detectors is the Dosimetry Telescope (DOSTEL), based on Silicon semiconductor technology. This active instrument provides time-resolved data and allows an analysis of the temporal variation and, due to the ISS orbiting Earth, the geographical distribution of the radiation field in Low Earth Orbit.

1.1. Structure of Thesis

In the next chapter, the radiation field in Low Earth Orbit (LEO) and the interaction of this radiation with matter will be described. Furthermore, relevant dosimetric quantities will be introduced there. The design, the working principle, and the data coverage of the DOSTEL will be explained in chapter 3. The data is analyzed in the chapters 4 to 7. In chapter 4 the data time correction based on the count rate dependence on the geomagnetic cutoff rigidity will be evaluated. This will be followed by the calculation of dose values in chapter 5. In chapter 6, the angular distribution of Galactic Cosmic Rays (GCRs) by using two different operational modes of DOSTEL and the distribution of inner radiation belt protons by using selected transits through the SAA region are investigated. The DOSTEL data of September and October 2004, recorded during disturbed conditions in the radiation belts, will be analyzed in chapter 7. Finally, chapter 8 will summarize important results acquired within this thesis and will give an outlook for possible future investigations.

Part of this work has been funded by the European Commission in the frame of the FP7 HAMLET project (Project # 218817).

2. Scientific Background

The MTR-DOSTEL is a dose-meter on board the ISS which is operating in LEO. The radiation field on ISS altitudes (330 km to 400 km for ISS) consists of two different populations of charged particles. The first population consist of charged particles from outside Earth's magnetosphere (chapter 2.1). They can have high enough energies to penetrate Earth's magnetic field (chapter 2.2) and reach ISS altitudes. The second particle population consists of magnetically trapped charged particles in Earth's radiation belts (chapter 2.3). The relevant interaction of charged particles with matter are discussed in chapter 2.4. DOSTEL measures the amount of energy deposited inside its detectors. From this energy deposition dose quantities (chapter 2.5) can be derived.

2.1. Energetic Particles Inside the Heliosphere

In addition to the solar wind, which can not penetrate Earth's magnetic field and can be neglected for this work, the heliosphere is populated with energetic particles (*Heber*, 2005). Among other sources, the particles consist of Galactic Cosmic Rays (GCRs) and Solar Energetic Particles (SEPs) produced during so-called solar particle events.

Galactic Cosmic Rays

GCRs were first discovered by Viktor Hess in 1912 (*Hess*, 1912). He used electrometers on board a balloon and discovered an increase of the ionization rate with increasing altitude. The assumption that he had discovered a new form of electromagnetic rays led to the name Galactic Cosmic Ray. Nowadays it is known that GCRs consist of 98% nuclei and 2% electrons. The nuclei consist mainly of protons (∼87%) and α particles (∼12%), while heavier nuclei contribute with ∼1% (*Simpson*, 1983). Figure 2.1 shows energy spectra of GCR nuclei.

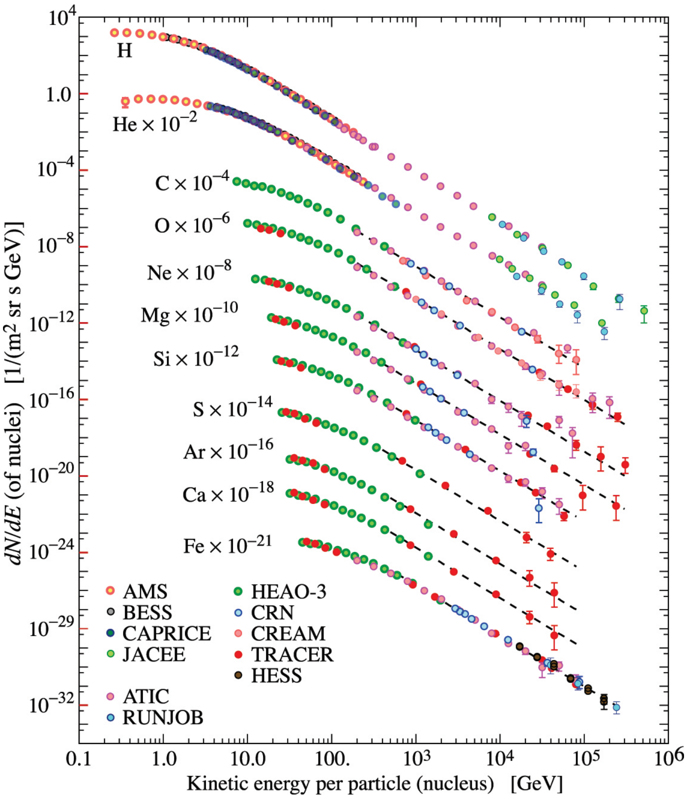

Figure 2.1.: Energy spectra of different components of the GCR. Protons as well as helium are the dominating particles. The intensity of the GCRs decrease with higher energies. This graph is taken from (*Beringer et al. (Particle Data Group)*, 2012).

The GCR particles cover energies from 10^6 to 10^{20} eV. They have a galactic origin and hit our heliosphere isotropically at a constant rate. Because the particles are charged, they move along the heliospheric magnetic field to get into the center of the solar system. During undisturbed heliosperic magnetic field conditions (solar minimum) it is easier for the GCRs to get into the the solar system and thus to Earth, than during disturbed magnetic field conditions (solar maximum). This leads to the effect that the GCR intensity is modulated by the solar cycle (*Heber and Potgieter*, 2006). The higher the solar activity the lower the flux of GCR. This solar activity modulation can be seen in figure 2.2. The count rate variation of the Kiel Neutron Monitor, which is a measure of the GCR flux, is anti-correlated to the number of sun spots, which are a measure of the solar activity. The variation of the GCRs is higher, the lower the particles' energies are. Particles reaching Earth are then again modulated by Earth's magnetic field.

Solar Energetic Particles

Impulsive solar eruptions (flares) can produce a broad spectrum of energetic particles (*Reames*, 2004). Protons can reach energies in the GeV range, which, however, happens very seldom. The particles are mostly ejected in a narrow cone and then follow the magnetic field lines of the sun. This means that only particles from a certain region of the sun (50° and 60° of solar longitude) can reach Earth. Latest observations have shown that some solar particle events, called wide spread events, can be observed over a large longitudinal range (*Dresing et al.*, 2012).

Particles can also be accelerated by shock waves driven by Coronal Mass Ejec-

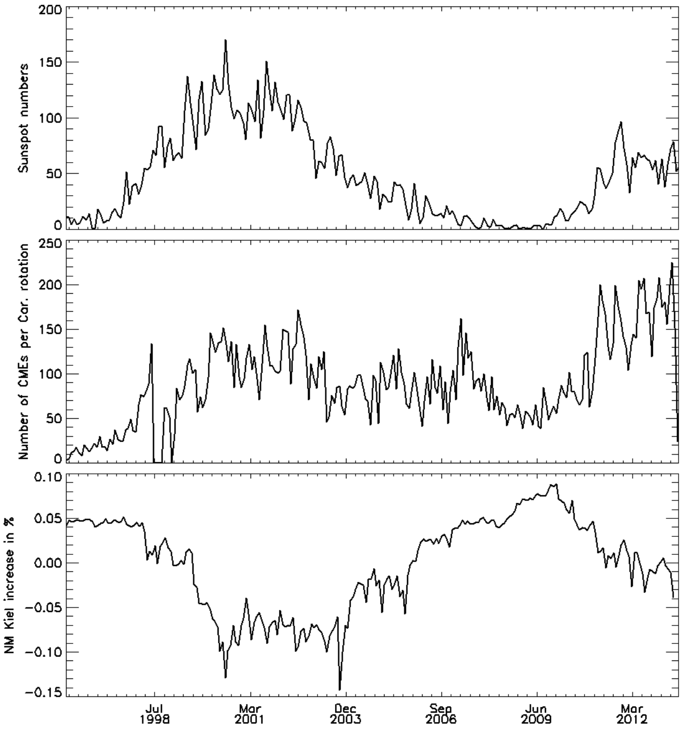

Figure 2.2.: The number of sunspots are an indicator of the solar activity and are shown over time in the upper panel. The number of CME's per Carrington rotation (mid panel) correlates with the solar activity. The intensity of GCRs anti correlates with the solar activity. This can be seen in the lower panel where the count rate variation of the Kiel Neutron Monitor is shown.

tions (CMEs) (*Cane and Lario*, 2006). The expansion of a CME can last several days, therefore particles accelerated by their shocks can also be observed up to several days. The highest energy a proton can reach due to acceleration at CME driven shocks is in the 100 MeV range. In addition CMEs have the capability of disturbing Earth's magnetic field (*Brueckner et al.*, 1998). The occurrence of solar events is correlated with the solar activity. Figure 2.2 shows the number of CMEs per Carrington rotation (mid panel) as an example. The number of CMEs is correlated with the number of sun spots (upper panel). The influence of solar events on the geomagnetic field field will be described later in chapter 2.2.

2.2. Earth's Magnetic Field

Earth has a magnetic field. This field has a complex structure, especially for the part further away from Earth. The magnetic field close to Earth, which means in this case less than 6 Earth radii (R_E) away from the surface, can be approximated by a dipole field (*Proelss*, 2008). This distance (6 R_E) in which the approximation is valid depends on the geomagnetic conditions and on the geographic location. Nevertheless, the ISS ,with an altitude of 330 to 400 km, definitely is situated in the close-to-Earth region, and thus, the magnetic field in ISS altitudes in principle has a dipole structure. The magnetic field lines are perpendicular to the surface at the magnetic poles and parallel to the surface at the equator. A more accurate description of the magnetic field can be made by using the International Geomagnetic Reference Field (IGRF) (*International Association of Geomagnetism and Aeronomy, Working Group V-MOD. Participating members et al.*, 2010). This description contains higher moments of the magnetic field and thus contains the decreased magnetic field strength in the region of the South Atlantic Anomaly (SAA) and the tilt of the magnetic axis, for example. The magnetic field of Earth plays a central role for the radiation field in LEO. The fact that charged particles interact with a magnetic field, due to the Lorentz force, leads to different phenomena determining the structure of the radiation field in LEO.

Cutoff Rigidity

Charged particles interact with Earth's magnetic field. The Lorentz force exerts a deflection force perpendicular to the particle velocity and perpendicular to the magnetic field lines. This deflection force results in turbulent particle trajectories inside Earth's magnetic field. The particles move in spirals along the magnetic field lines and perform drift motions before reaching Earth. The deflection force depends on the magnetic field strength and on the particle's rigidity, which is the momentum per charge of the particle. The lower the rigidity of a particle the stronger is the deflection by a magnetic field. This means a particle can not penetrate a perpendicular magnetic field, if its rigidity is too low.

Charged particle motion in a dipole field was first investigated by Størmer (*Størmer*, 1933). From his calculations a formula for the minimal required rigidity that a particle with perpendicular incident needs to penetrate Earth's magnetic field can be derived.

$$R_c = \frac{M}{4 \cdot r_E^2} \cdot cos^4(\alpha) \tag{2.1}$$

This relation depends, besides the Earth's radius r_E and Earth's dipole moment M, on the geomagnetic latitude α, as the magnetic field strength parallel to Earth's surface, which has a shielding effect against charged particles, depends on the geomagnetic latitude. At the geomagnetic poles, where the magnetic field lines are perpendicular to the surface, the parallel component is zero, and it is easy for charged particles to penetrate the magnetic field. At the geomagnetic equator, where the magnetic field line component parallel to the surface has its maximum, it is hardest for charged particles to penetrate the magnetic field. The required rigidity R_c a particle needs to reach a certain location is called geomagnetic cutoff rigidity and strongly depends on the geomagnetic latitude. For a location with a cutoff rigidity R_c, only particles with higher rigidities than $R = \frac{p \cdot c}{z \cdot e}$ are able to reach this location. In this work the Effective Vertical Geomagnetic Cutoff Rigidity (R_c), calculated by K. Herbst (*Herbst*, 2009), will be used for further analysis. A geographic distribution of these R_c values is shown in figure 2.3. For the R_c calculation negatively charged particles with different rigidities were shot vertically upwards. The minimal rigidity a particle then needs to leave the magnetic field, in this case the IGRF field, is also the minimal rigidity a positive charged particle would need to reach this location from outside the magnetic field. This calculation was done for a 5°×5° grid with latitudes between ±50° and for

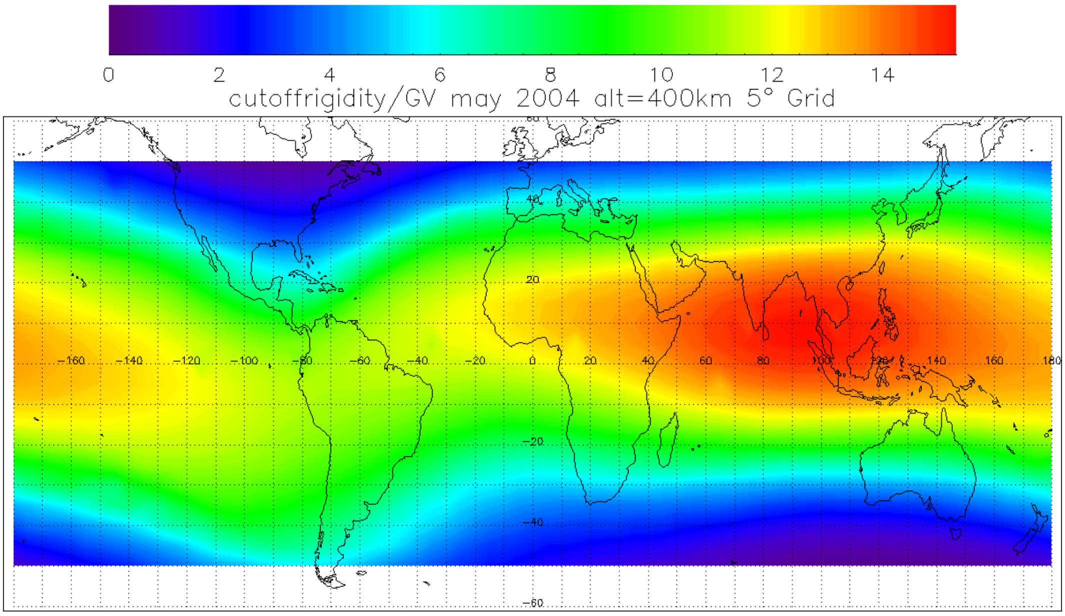

Figure 2.3.: Effective vertical geomagnetic cutoff rigidity for the year 2004 at an altitude of 400 km. The data were calculated by K. Herbst (*Herbst*, 2009).

an altitude of 400 km using the IGRF for the year 2004. A detailed description of this calculation can be found in (*Herbst*, 2012). A description of the general method using negative particles which are shot upwards to determine R_c is given by (*Smart and Shea*, 2009).

McIlwain L-parameter

The McIlwain L-parameter (*McIlwain*, 1961) is a useful parameter of categorizing charged particles trapped in the magnetic field of Earth. The L-parameter or L-shell describes magnetic field lines of Earth's magnetic field. They are numbered by their distance to the dipole center at the geomagnetic equator in units of Earth radii as illustrated in Figure 2.4. A magnetic field line which crosses Earth's surface at the geomagnetic equator has an L-parameter of $L \sim 1$. The whole magnetic field line is then numbered with this L-value. Charged particles gyrate around magnetic field lines and thus are trapped by this specific field line. Due to this the L-parameter is a suitable parameter of describing different populations of trapped particles. In this work the L-parameters are calculated from the Effective

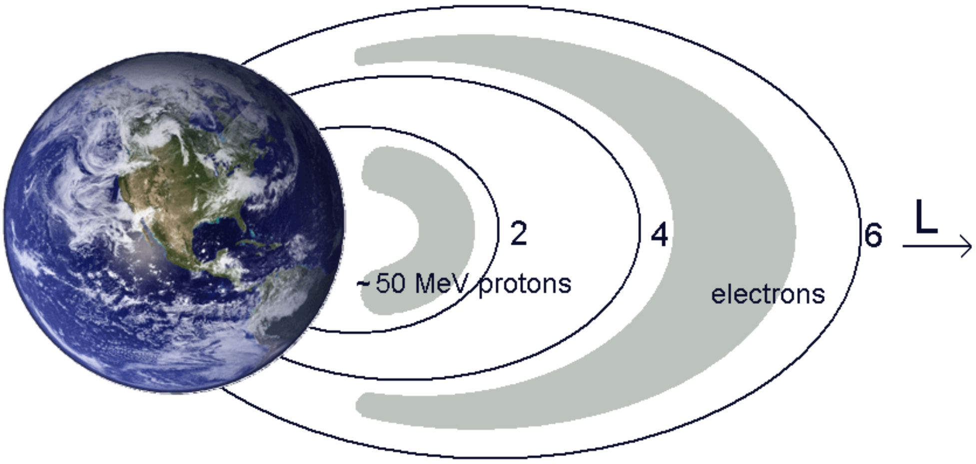

Figure 2.4.: Illustration of the McIlwain L-parameter. The magnetic field lines are numbered by their distance to the dipole center in units of Earth radii. The gray area below L=2 sketches the inner radiation. The outer radiation belt is sketched in gray between L=4 and L=6.

Vertical Geomagnetic Cutoff Rigidity (R$_c$), as described in *Shea et al.* (1987):

$$L = \frac{R_c}{16.237}^{\frac{-1}{2.0352}} \tag{2.2}$$

The ISS at its altitude of ~350 - 400 km and orbital inclination of 51.6° covers L-parameters from close to 1 at the geomagnetic equator up to L ~ 6 at highest geomagnetic latitudes.

Geomagnetic Storms

Geomagnetic storms are temporary sporadic fluctuations in the geomagnetic field. These changes can result in different phenomena which are often summarized under the term space weather. Prominent space weather phenomena are for example:

- Geomagnetically induced currents in long electrical conductors (e.g., power networks or pipelines)
- Ionospheric disturbances causing radio and radar dysfunctions
- Aurorae at unexpected low geomagnetic latitudes

Geomagnetic storms are defined by changes in the Disturbance Storm Time (DST) index which describes the geomagnetic activity. It is an hourly averaged value derived from horizontal magnetic field variations measured with a network of near equatorial geomagnetic observatories (*Sugiura*, 1964). Under normal conditions the DST index varies between ± 20 nT. Geomagnetic activities with an DST index below -50 nT are classified as geomagnetic storms. Major or intense geomagnetic storms is a common name for storms with DST indices below -100 nT (*Zhang et al.*, 2007).

Another often used parameter for describing disturbances in the geomagnetic field is the planetary K-index (Kp). The Kp index is the mean standardized K-index from 13 geomagnetic observatories. The local K-index is a quasi-logarithmic value from 0 to 9 describing the fluctuation of the horizontal magnetic field during a three hour time interval. These fluctuation are converted to K-indices by using different relations for different geomagnetic observatories. The relation between magnetic fluctuation and K-index is done in a way that all geomagnetic observatories show a comparable rate of occurrence of certain levels of K-indices. Geomagnetic storms with Kp indices greater or equal 7 are often categorized as major/intense storms.

It is known that geomagnetic storms are caused by magnetic structures evolving from events on the sun (*Brueckner et al.*, 1998). The intensity of the geomagnetic disturbance correlates with a negative interplanetary magnetic field component perpendicular to the ecliptic (B_z) combined with fast solar wind speeds (*Yermolaev et al.*, 2012). There are two main sources of magnetic structures with negative B_z components. Major geomagnetic storms are predominantly caused by Interplanetary Coronal Mass Ejections (ICME's) and their related magnetic structures. Between 1996 and 2005, $\sim$ 85 % of the major geomagnetic storms were driven by ICME's (*Zhang et al.*, 2007). Co-rotating Interaction Regions (CIRs) can also cause geomagnetic storms. These storms in general show smaller DST indices. As shown in *Zhang et al.* (2007), $\sim$ 15 % of the major storms between 1996 and 2005 were driven by CIRs. CIRs can be stable over month, and thus, can cause periodic geomagnetic storms occurring every 27 days (period of solar rotation).

2.3. Earth's Radiation Belts

In 1958 scientists under the lead of James A. van Allen discovered two regions with high intensities of corpuscular radiation around Earth (*Van Allen and Frank*, 1959). These so called van Allen radiation belts consist of charged particles, mainly electrons and protons, trapped in Earth's magnetic field. The electrons have energies of up to several MeV and the protons can reach energies of a few hundred MeV. The energies of these particles are too low to enter Earth's magnetic dipole field. But when they are inside Earth's magnetic field they are trapped, because Earth's magnetic field act as a magnetic bottle. The particles with mass number m and charge number q gyrate in spirals with a gyro radius of $r_B = \frac{m \cdot v_\perp}{q \cdot B}$ and a parallel velocity $v_\|$ around a guiding field line (with magnetic flux density B). With increasing geomagnetic latitude the magnetic flux density increases and the charged particles pass regions with magnetic field line components perpendicular to the guiding field line. These perpendicular magnetic field components lead to a mirror force which decelerates the particle's velocity component parallel to the guiding field line. The parallel velocity component $v_\|$ is transferred to the perpendicular velocity component $v_\perp$ until reaching the mirror point, where $v_\| = 0$. Then $v_\|$ changes its sign and the particle moves back to lower geomagnetic latitudes. When reaching the opposite hemisphere of the dipole field the magnetic flux density increases again and the described effect starts again. The particle is reflected back and forth at magnetic mirrors close to the magnetic poles. The position of these magnetic mirrors depends on the pitch angle, and thus, on the ratio of the perpendicular and parallel particle velocity $\frac{v_\perp}{v_\|}$, at the geomagnetic equator. For particles with low pitch angles the mirror points can be on Earth's surface or below. These particles can not be trapped in Earth's magnetic field. For every L-parameter a different minimal pitch angle is required to let the mirror points be above the atmosphere, so that the particle remains trapped in Earth's magnetic field. There are two regions with high intensities of such trapped charged particles - the inner and the outer radiation belt (illustrated in figure 2.4 in gray).

Inner Radiation Belt

The inner radiation belt consists mainly of protons and electrons. It typically lies in the region $1.2 < L < 2.0$ and is very stable over time (*Durante and Cucinotta*, 2011). Significant short time variations of electron intensities can only be observed during the most powerful geomagnetic storms (*Baker et al.*, 2007). This stability results from the main origin of the inner radiation belt particles, the Cosmic Ray Albedo Neutron Decay (CRAND) process (*White*, 1973). High energy GCR particles hit Earth's atmosphere and produce neutrons. They decay to one proton, one electron, and one anti-neutrino. If this decay takes place in the region of the inner radiation belt, the electron and the proton are trapped. In addition, during geomagnetic storms, a directly entering of solar protons is possible (*Kress et al.*, 2005). The loss processes for protons are Coulomb collisions with electrons, charge exchange with hydrogen atoms and atmospheric absorption (*Singh et al.*, 2011). Due to the source and loss processes a variation of the inner radiation belt proton flux with the solar cycle can be observed (*Miyoshi et al.*, 2000). The CRAND process is driven by GCR particles, whose intensity varies with the solar cycle. The proton loss due to atmospheric interactions also depends on the solar cycle. During high solar activity the increased irradiance heats and expands the upper atmosphere which leads to higher probability of particle-atmosphere interactions.

The relevant particle species for dosimetry in the inner radiation belt are protons. The highest particle flux for 50 MeV protons can be observed at $L=1.8$ (*Proelss*, 2008). The importance of the inner radiation belt for dosimetry in LEO results from the structure of Earth's magnetic field. There is a region over the coast of Brazil with reduced magnetic field strength, which results from the 11° inclination and the 500 km shift of the geomagnetic dipole axis towards the western Pacific as well as from higher moments of the geomagnetic field. This region is the so called SAA (*Reitz*, 2008). Here the inner radiation belt extends down to altitudes of 200 km. Proton energy spectra measured by the PAMELA experiment in the region of the SAA are shown in figure 2.5. The highest particle flux can be observed in the center of the SAA. At ~ 10 GeV particle energy the effect of the geomagnetic cutoff rigidity (~ 10 GV in the SAA-region) can be seen. Outside particles with energies below ~ 10 GeV are deflected by Earth's magnetic field and are not able to reach ISS altitudes in the SAA region.

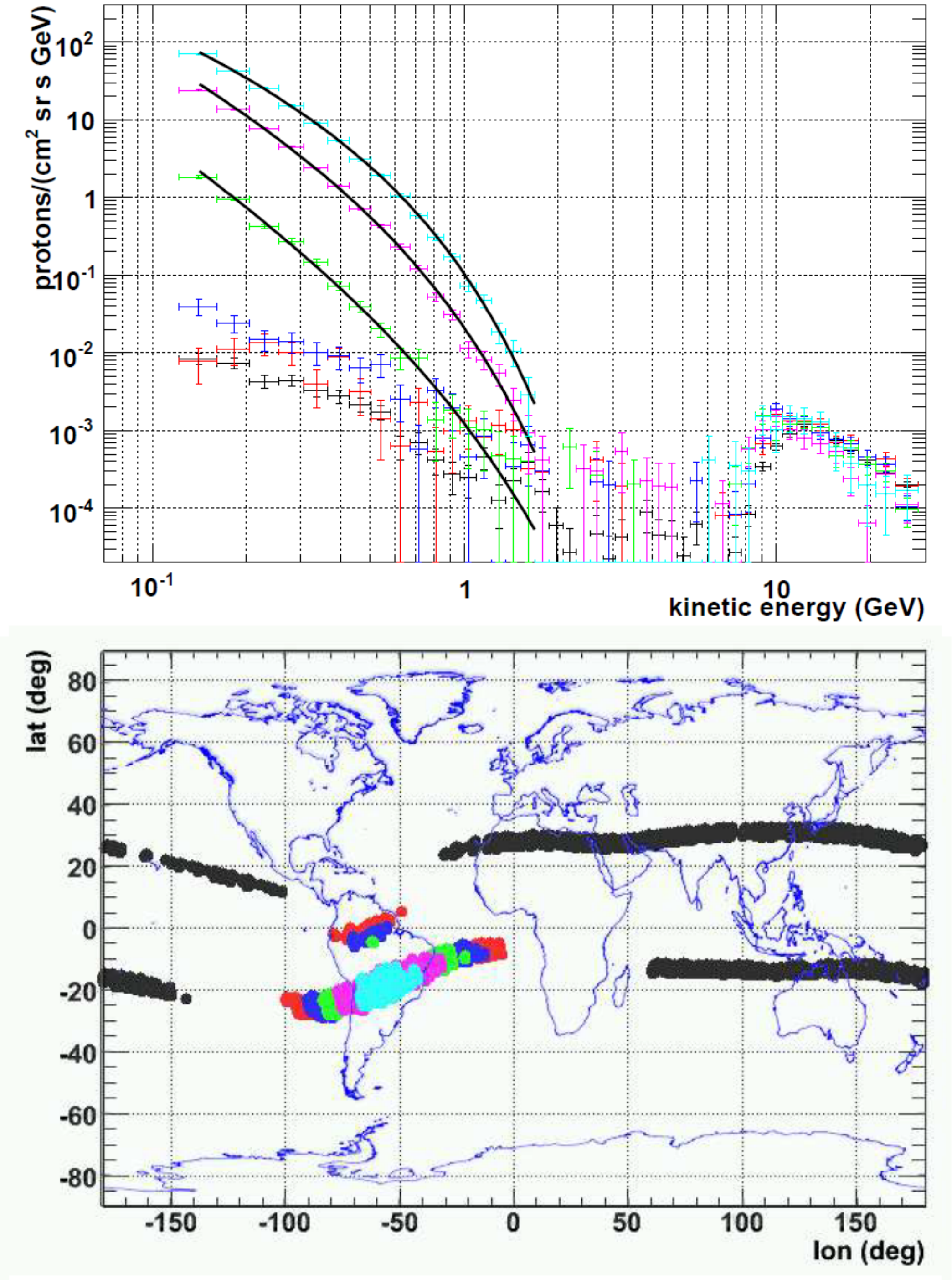

Figure 2.5.: Proton energy spectra of SAA crossing measured by PAMELA (*Casolino et al.*, 2008). The color code of the energy spectra in upper panel correlates with the geographic position of measurement (lower panel).

The ISS has 6-8 orbits per day crossing the inner radiation belt in the region of the SAA. The ISS altitude with ∼ 400 km is close to the mirror point of the inner radiation belt particles. Due to this the particles have high pitch angles (close to 90°) and the particle flux has its maximum in a plane perpendicular to the local geomagnetic field (*Sakaguchi et al.*, 1999). Particles arriving from the East have their gyro center below the point of observation, whereas the particles from western direction have their gyro center above the point observation. Particles which would enter the point of observation from the East have a higher probability of interactions with the atmosphere than the particles from the West. This primarily leads to the East-West effect, where more particles arrive from western directions. The gyro radius of a particle increases with its energy, and thus, the East-West effect is increasing for increasing particle energies (*Badavi et al.*, 2011). A sketch of the incidence directions of SAA protons is shown in figure 2.6.

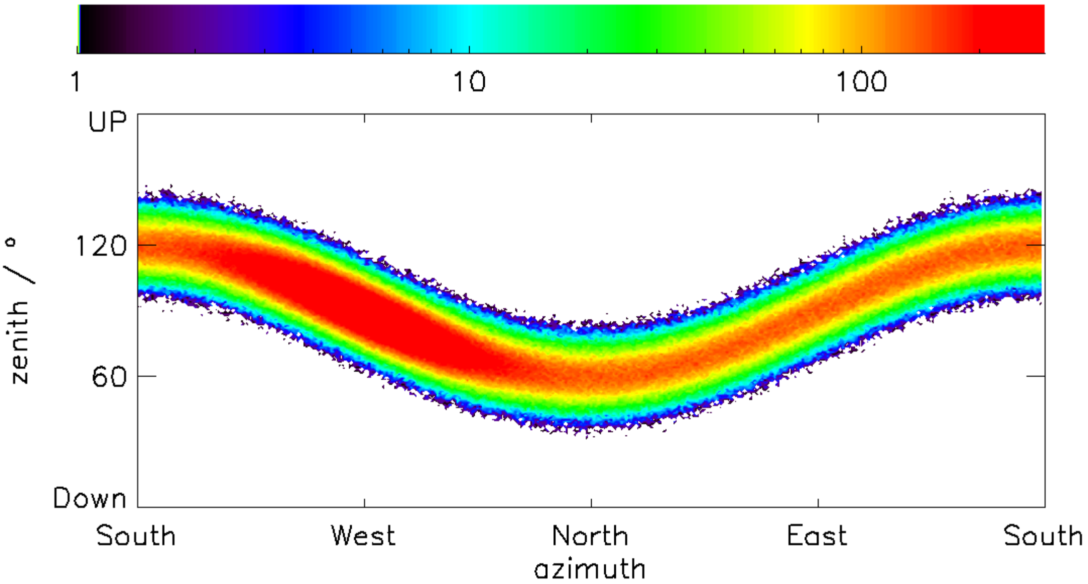

Figure 2.6.: Sketch of angular proton distribution in the SAA region. The particles mostly reach a location from a plane perpendicular to the local geomagnetic field. Due to the East-West effect more particle arrive from western directions (adapted from *Sakaguchi et al.* (1999) and *Badavi et al.* (2011)).

Outer Radiation Belt

The outer radiation belt lies in the region $3 < \mathrm{L} < 7$ and is dominated by electrons. The electron intensities are highly dynamic and show short term variations especially during geomagnetic storms by several orders of magnitude (*Durante and Cucinotta*, 2011). For dosimetry in LEO the outer radiation belt is of less interest, as only very few electrons of the outer radiation belt reach ISS altitudes under normal conditions and can be effectively shielded by the ISS hull, for example.

Slot Region

The slot region is the region between the inner and outer radiation belt. It extends from $2 < \mathrm{L} < 3$ and is characterized by a low flux of trapped radiation. The depletion of relativistic electrons in this region results from the equilibrium between inward radial diffusion and effective pitch angle scattering loss (*Lyons and Thorne*, 1973). The pitch angle scattering is mainly driven by resonant wave particle interactions with whistler mode waves generated by wave turbulence in space, the so called plasmaspheric hiss (*Millan and Thorne*, 2007). Due to enhanced inward transport and local particle acceleration, the particle flux can be dramatically increased during strong geomagnetic storms, such as the so-called Halloween storms in 2003 (*Baker et al.*, 2004), for example. The occurrence of increased electron intensities in the slot region corresponds to extreme solar wind conditions (very large negative B_z, high solar wind speed, density and dynamic pressure, etc.). The L-parameter to which the electrons reaches down shows a good correlation with the DST index (with a delay time of 3 days) of the corresponding geomagnetic storm (*Zheng et al.*, 2006). Due to the effective pitch angle scattering in the slot region, the electron flux decays on time scales of days to weeks back to pre-storm conditions (*Meredith et al.* (2009) and *Meredith et al.* (2007)).

2.4. Interaction of Ionizing Radiation with Matter

Radiation detectors use the fact that ionizing radiation interacts with the detector material. During this interaction the incoming radiation is depositing energy in the detector. In the following the physical process of this energy deposition will be described (following the text books (*Allkofer*, 1971), (*Grupen*, 1993) and (*Knoll*, 2000)).

Heavy charged particles

During a passage through matter charged energetic heavy particles mostly interact via Coulomb collisions with the shell electrons of the material's atoms. In this process they lose energy. Spoken from the material point of view, they deposit energy in the material. The energy of the charged particles relevant for this work is of magnitudes higher than the binding energy of the detector material's shell electrons. Due to this the target material electrons can be assumed to be free and initially at rest in comparison to the incoming heavy charged particle and the mean energy loss per distance ($-\frac{dE}{dx}$) can be calculated by using the Bethe-Bloch formula 2.3:

$$-\frac{dE}{dx}_{(col)} = \rho \cdot N_A \cdot \frac{e^4}{4\pi \cdot \varepsilon_0^2 \cdot m_e} \cdot \frac{Z}{A} \cdot \frac{z^2}{v^2} \cdot \left[\ln \left(\frac{2 m_e c^2 \beta^2}{\langle I \rangle \cdot (1-\beta^2)} \right) - \beta^2 - \frac{\sigma}{2} \right] \quad (2.3)$$

The variables and constants in the Bethe-Bloch formula are explained in table 2.1. For non-relativistic particles ($\langle I \rangle <<$ E $<< mc^2$) the term in square brackets shows marginal variations and the energy loss of these particles is proportional to the square of the ratio of particle charge and velocity and thus proportional to the mass and inversely proportional to the energy of the particle:

$$\frac{dE}{dx}_{(col)} \propto \frac{z^2}{v^2} \propto \frac{m \cdot z^2}{E} \quad (2.4)$$

The energy loss of a charged particle in an absorber results from many single distant Coulomb encounters. These interactions are stochastic events, and thus, the energy losses follow a probability distribution, distributed around the mean energy loss resulting from formula 2.3. For a long path of charged particles in the material the number of interactions is large and the energy loss shows a Gaussian distribution. For a thin absorber the number of collisions decreases and the energy loss distribution becomes asymmetric. Single collisions with high energy

Table 2.1.: Variables and constants in the Bethe-Bloch formula

β	$\frac{v}{c}$
v	particle velocity / $\frac{m}{s}$
c	speed of light / $\frac{m}{s}$
z	particle charge number ($z \cdot e =$ particle charge)
m	particle mass in atomic mass units
e	elementary electric charge
N_a	Avogadro's number
Z	absorber charge number
A	absorber mass in atomic mass units
ρ	absorber density / $\frac{kg}{m^3}$
$\langle I \rangle$	mean ionization potential of the absorber / eV
m_{e}	electron rest mass $/kg$
ε_0	permittivity / $\frac{F}{m}$
σ	density correction

transfers lead to long tail towards high energy deposition. For this so-called Landau distribution the mean energy loss does not match the most probable energy loss, which is shifted to lower energy depositions.

Electrons

Formula 2.3 describes the energy loss due to collisions for heavy charged particles. The mass of these particles is of magnitudes higher than the mass of the absorber atom's electrons, and thus, their direction is not influenced during the collisions. This is not the case for incoming electrons interacting with matter. The identical mass of incoming and absorber electrons lead to strong deviations of the incoming particles direction. This leads to two major effect. First, electrons with identical energies and identical incident angles can have different path lengths while penetrating the detector, due to scattering. These unequal path lengths lead to differing number of collisions, and thus, to different energy losses. The second effect is the Bremsstrahlung, which has to be considered for electrons. Charged particles accelerated in a Coulomb field lose energy by emitting Bremstrahlung.

$$-\frac{dE}{dx}_{(Brems)} = 4\alpha \cdot \rho \cdot N_A \cdot \frac{Z^2}{A} \cdot z^2 \cdot r_e^2 \cdot E \cdot \ln\left(\frac{183}{Z^{\frac{1}{3}}}\right) \tag{2.5}$$

$$r_e = \frac{1}{4\pi \cdot \varepsilon_0} \cdot \frac{e^2}{m_e \cdot c^2} \tag{2.6}$$

The variables and constants are identical to the one used in equation 2.3 and are shown in table 2.1. In contrast to the energy loss by ionization the energy loss due to Bremsstrahlung is proportional to the particle's energy and inversely proportional to square of the particle's mass:

$$\frac{dE}{dx}_{(Brems)} \propto \frac{E}{m^2} \tag{2.7}$$

Due to the dependence on m^{-2}, the energy loss induced by Bremsstrahlung is very important for electrons. For heavy charged particles the Bremsstrahlungs induced energy loss can be neglected. For electrons the importance of Bremsstrahlung increases with energy and the total energy loss of electrons has to be calculated by the sum of energy loss from collisions and Bremsstrahlung.

$$\frac{dE}{dx}_{(total)} = \frac{dE}{dx}_{(col)} + \frac{dE}{dx}_{(Brems)} \tag{2.8}$$

Photons

To detect photons with a solid state detector they have to produce charged particles inside the detector's material. During these stochastic processes the photons get absorbed or deflected to large angles of scattering. This leads to exponential decay of the photon intensity while penetrating matter. There are three main effects in which charged particles are produced by photons. The first is the photo effect, in which the photon energy is completely absorbed by an atom's electron. For photon energies $(h \cdot \nu)$ greater than the binding energy of the electron (E_e), the electron is emitted from the atom and has a kinetic energy of $E_{kin} = h \cdot \nu - E_e$. In silicon the photo effect is dominant up to photon energies of ~0.06 MeV. For higher photon energies up to ~16 MeV the Compton effect is the dominating photon interaction. Photon energy is transferred to electrons due to inelastic scattering. The maximal energy transfer $E_{e,max}$ for back scattered photons with an energy E_ν is:

$$E_{e,max} = \frac{2E_\nu^2}{2E_\nu + m_e c^2} \tag{2.9}$$

The pair production is the third possibility to create charged particles inside a detector. Photons with higher energies than twice the rest mass of an electron ($2 \cdot m_e c^2$) can interact with the Coulomb field of an atom by producing an electron positron pair. This effect supersedes the Compton effect in silicon for photon energies above ~16 MeV.

Neutrons

Neutrons are uncharged, and thus, do not interact via Coulomb forces but directly, through short ranged forces, with an absorber atom. These interactions can be classified in two main effects - elastic collision and compound nuclear reactions. Both of these effects have very low cross sections for interacting with silicon, whereas in a simplification the probability for elastic collisions predominates for fast neutrons with energies above 0.5 eV. An elastic scattered neutron transfers energy to an absorber atoms, which then interacts with the absorber material as described in formula 2.3. The energy transfer depends, as in the classical elastic collision, on the scattering angle and on the mass number of the absorber atom. For silicon with a mass number of 28 the maximal transferred energy is ~ 13% of the neutron energy. Due to the low cross section a solid state detector is not well suited for the measurement of neutrons and underestimates the energy deposition due to neutrons.

2.5. Dose Quantities

This section gives an overview about the dose quantities which can be obtained by the DOSTEL measurements. A more detailed description of all dose quantities commonly used in radiation protection (e.g., the effective dose, which can not be measured with DOSTEL) can be found in (*ICRU*, 1984).

Absorbed Dose

The absorbed dose D is the amount of energy dE deposited in a mass element dm. The unit of the absorbed dose is Gray (1 Gy = $\frac{J}{kg}$).

$$D = \frac{dE}{dm} \tag{2.10}$$

The absorbed dose depends on the absorber in which the energy is deposited. In this work D is generally used for the absorbed dose in water. If it is in regard to the absorbed dose in silicon, D_{Si} will be used.

Linear Energy Transfer (LET)

The Linear Energy Transfer (LET) is the the amount of energy (dE) deposited by ionizing radiation inside the absorber material along the pathlength (dl).

$$LET = \frac{dE}{dl} \tag{2.11}$$

The SI unit of the LET is $\frac{J}{m}$ but for dosimetric purpose the atomic unit $\frac{keV}{\mu m}$ is used. The LET strongly depends on the type and energy of the radiation. For charged particles the LET approximates the electronic stopping power.

Quality Factor

To take the biological effectiveness of different types of ionizing radiation into account a dimensionless quality factor (Q) is used. For charged particles the approach described in the ICRP Publication 60 (*ICRP*, 1991) is used. In this method the Q of charged particles depends on their LET. The Q dependence on the LET is given by the following function:

$$Q(LET) = \begin{cases} 1 & \text{for } LET < 10 \text{ keV} \cdot \mu m^{-1} \\ 0.32 \cdot LET - 2.2 & \text{for } 10 \text{ keV} \cdot \mu m^{-1} \leq LET \leq 100 \text{ keV} \cdot \mu m^{-1} \\ 300/\sqrt{LET} & \text{for } LET > 100 \text{ keV} \cdot \mu m^{-1} \end{cases} \tag{2.12}$$

The characteristics of this Q-function can be seen in figure 2.7. The function is 1 for LET below 10 keV $\cdot$ μm^{-1}. The function then increases up to a value of ∼30 for 100 keV $\cdot$ μm^{-1} as the higher ionization density can produce more cell damage, especially DNA double stand breaks. These damaged cells can have

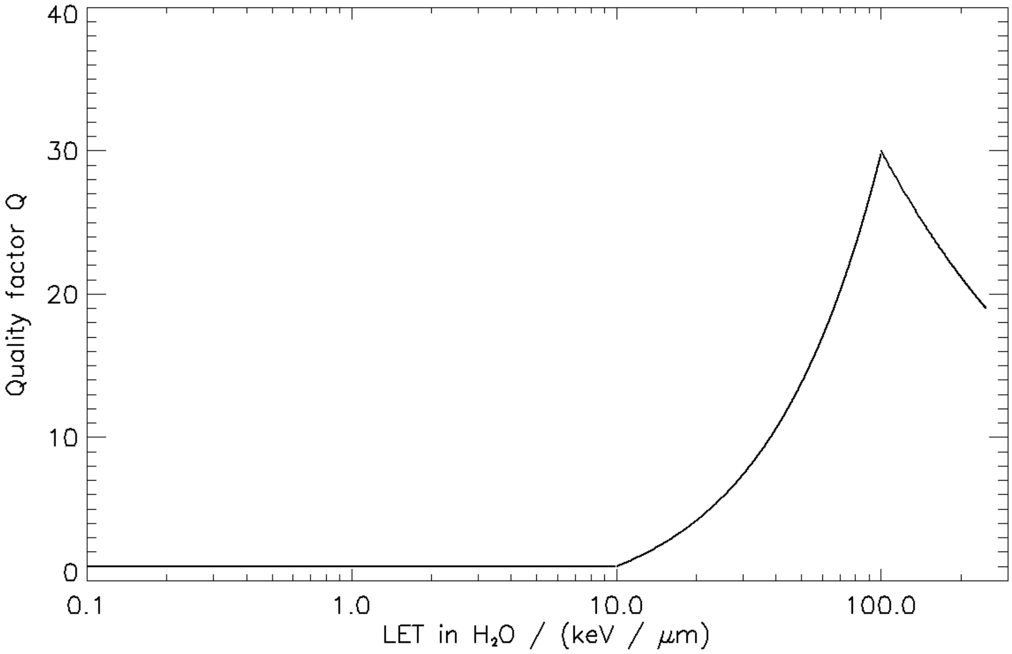

Figure 2.7.: This figure shows the LET-dependent Quality factor function, defined after ICRP60. Equation 2.12 shows the formula of this function.

defective DNA and can cause mutation effects such as cancer. For higher LET, the Q-function decreases again. This is due to the fact that such high ionization densities can lead to cell death. A dead cell will not show mutation which is better than a damaged cell.

Dose Equivalent

The dose equivalent (H) is a value which is used in radiation protection. It takes the biological effectiveness of the ionizing radiation into account. H is the product of the absorbed dose D and the mean quality factor $\langle Q \rangle$.

$$\langle Q \rangle = \frac{\int D_{LET} \cdot Q(LET) \cdot d_{LET}}{\int D_{LET} \cdot d_{LET}}$$

$$H = D \cdot \langle Q \rangle \tag{2.13}$$

Due to the dimensionlessness of Q, the dose equivalent H has the same unit $\frac{J}{kg}$ as the absorbed dose D. To distinguish H from D its quantity is called Sievert (1 Sv $= 1 \, \frac{J}{kg}$).

3. Instrumentation

MATROSHKA is an ESA experiment under the project lead of the German Aerospace Center (DLR) Cologne. The experiment simulates the radiation exposure to an Astronaut as exact as possible. For this purpose a phantom of an upper human torso equipped with radiation measurement devices (see figure 3.1) was brought to the ISS to measure the radiation exposure inside and outside the phantom. A detailed description of the MATROSHKA experiment is given in *Dettmann et al.* (2007). The radiation measurement devices of MTR can be grouped in passive and active detectors. The passive detectors are mainly

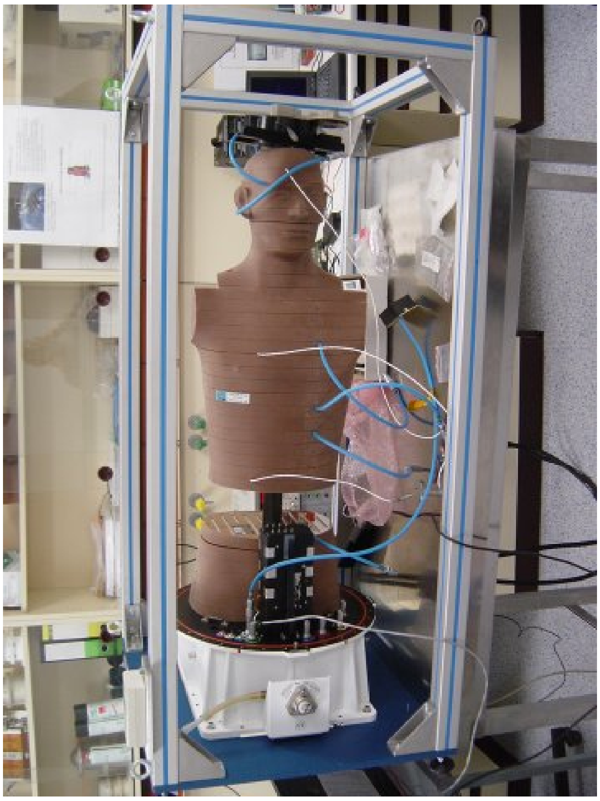

Figure 3.1.: Photograph of the MTR experiment. The human torso is build of slices equipped with radiation detectors. Picture courtesy of DLR.

Thermo Luminescent Detectors (TLDs) and Plastic Track Etch detectors (CR39). Descriptions and results of the passive detectors can be found in *Reitz and Berger* (2006), *Reitz et al.* (2009), *Zhou et al.* (2010) and *Berger et al.* (2013), and will not be further evaluated in this thesis.

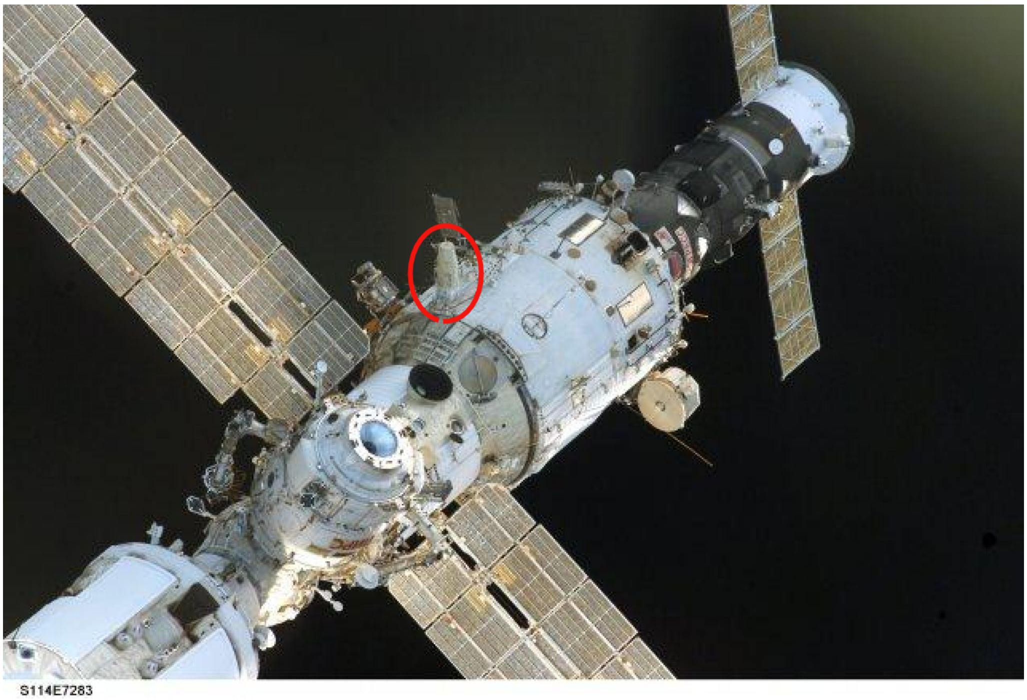

Figure 3.2.: Photograph of the MTR experiment (see red mark) during the MTR-1 mission phase. The experiment was mounted outside the Zvezda module (Service Module SM) of the ISS. Picture courtesy of NASA.

The active instrumentation of MTR consist of the Tissue Equivalent Proportional Counter (TEPC) operated by NASA, four Silicon Scintillator Devices (SSD), and the Dosimetry Telescope (DOSTEL). The SSD's and the DOSTEL were built and operated by the Christian-Albrechts-Universität (CAU) zu Kiel. In this work the data obtained with the DOSTEL are analyzed. A detailed description of this detector follows in chapter 3.1. The MTR experiment was brought to the ISS by the Russian expendable freighter spacecraft Progress 13P launched at January 29th 2004 from Baikonur Cosmodrome. Since then, 4 MTR mission phases took place (MTR-1, MTR-2A, MTR-2B, MTR-2 KIBO). The active instrumentation was used during the first and the third mission phase. During MTR-1 the experiment was mounted outside the Zvezda module (Service Module SM) of the ISS

Figure 3.3.: Photograph of the MTR experiment during the MTR-2B mission phase. The MTR experiment was located inside the Zvezda module (Service Module SM) of the ISS. Picture courtesy of DLR.

from February 2004 to August 2005 (see figure 3.2). The active instrumentation was again in operation during the MTR-2B mission phase, where the experiment was again mounted inside the Zvezda (see figure 3.3). This mission phase lasted from October 2007 to November 2008. The DOSTEL data is not covering the whole mission times of MTR-1 and MTR2-B. Its time coverage will be shown in chapter 3.1.

3.1. DOSTEL

The Dosimetry Telescope (DOSTEL) is a particle telescope built of Silicon detectors to measure dose quantities. It is designed for the operation in LEO and flight altitudes. The first DOSTEL was flown in the ESA Biorack on the Shuttle-to-MIR mission STS 76 in March 1996 (*Beaujean et al.* (1999b) and *Beaujean et al.* (1999c)). Since then, different DOSTEL units were used for measurements on aircraft (*Beaujean et al.*, 1999a), the Russian MIR station (*Beaujean et al.* (2002) and (*Badhwar et al.*, 2002)) and on the ISS during the DOSMAP experiment (*Reitz et al.*, 2005) as well as the MATROSHKA experiment (2004,2008) and the DOSIS and DOSIS 3D experiments (since 2009) (*Burmeister et al.*, 2012).

MATROSHKA DOSTEL

The MATROSHKA (MTR) DOSTEL was especially designed for the MTR project. It differs from the original DOSTEL units as in addition to the Silicon semiconductor telescope, two Hamamatsu PIN diodes are mounted perpendicular to this telescope. A photo of the detector head can be seen in figure 3.4 and a sketch of the sensor head is shown in figure 3.5. The telescope is built of two Passivated

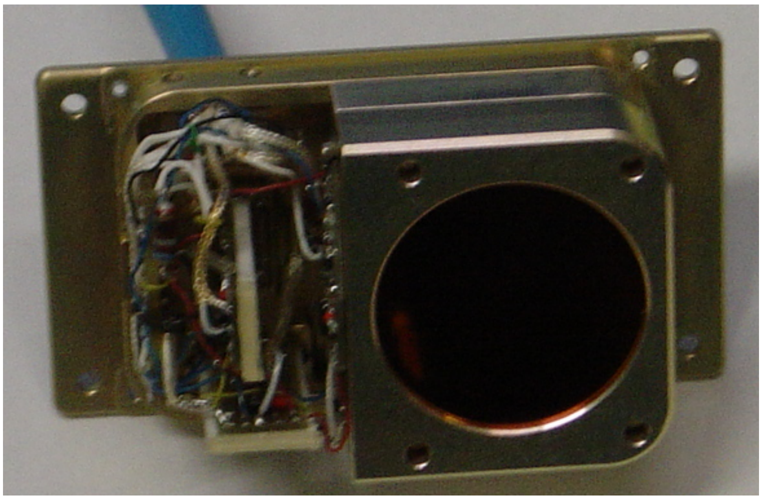

Figure 3.4.: Photograph of the DOSTEL detector head. Under the circular window covered with Kapton foil on the right side, two Canberra PIPS detectors form a telescope. On the left side two Hamamatsu PIN diodes mounted perpendicular to the telescope can be seen.

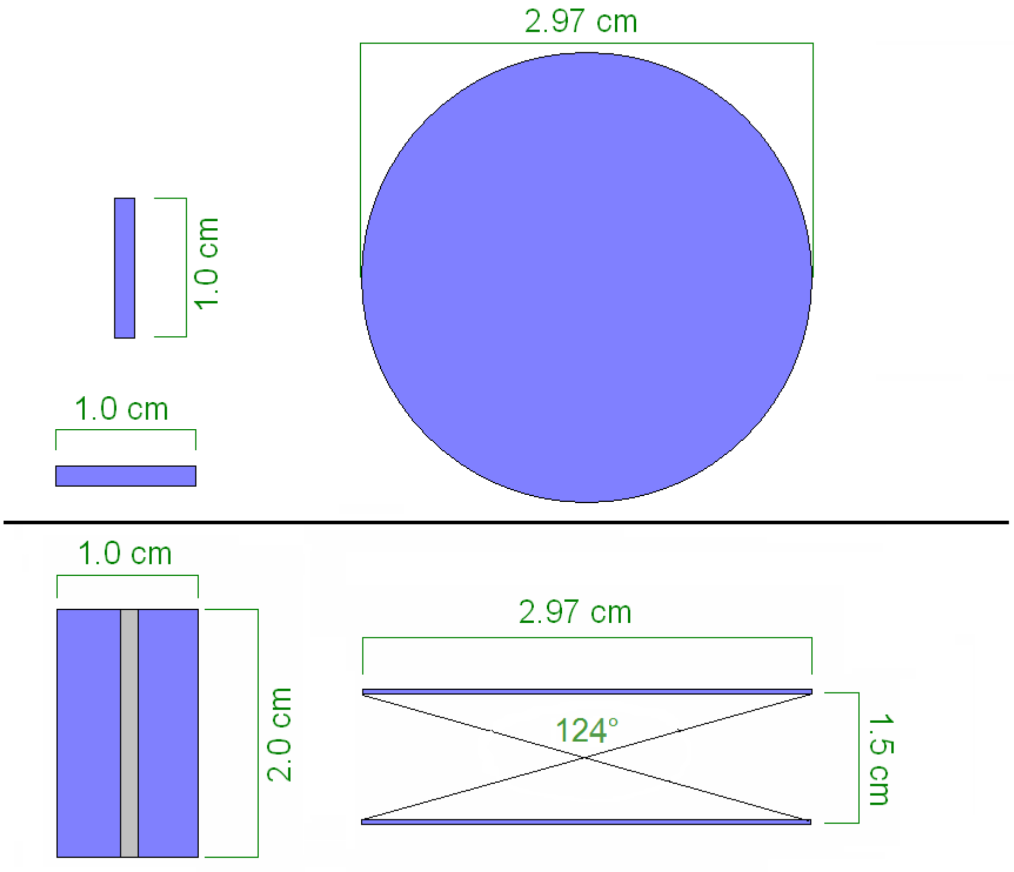

Figure 3.5.: Sketch of the DOSTEL detector head. The upper sketch shows the view from top and the lower sketch a side view on the detectors. The two PIPS detector form a telescope with an opening angle of 124°. The Hamamatsu PIN diodes are mounted perpendicular to the telescope.

Implanted Planar Silicon (PIPS) detectors manufactured by Canberra Semiconductors. Both detectors have a sensitive area of 6.93 cm^2, each. The upper detector (D4) has a thickness of 154 μm whereas the lower detector (D1) is 315 μm thick. The detectors are mounted in a distance of 1.5 cm, which leads to a telescope with an opening angle of 124° and a geometric factor of 824 $mm^2 \cdot sr$ for particles coming from the top. The Hamamatsu PIN diodes (D2,D3) have a sensitive area of 2.31 cm^2 and a thickness of 300 μm. Each of the silicon detectors is connected to a signal processing logic. A sketch of the signal processing logic can be seen in figure 3.6. A charged particle produces free charge carriers in the detector. These free charge carriers are collected by the Charge Sensitive Amplifier (CSA), which amplifies and transfers the signal in a voltage pulse.

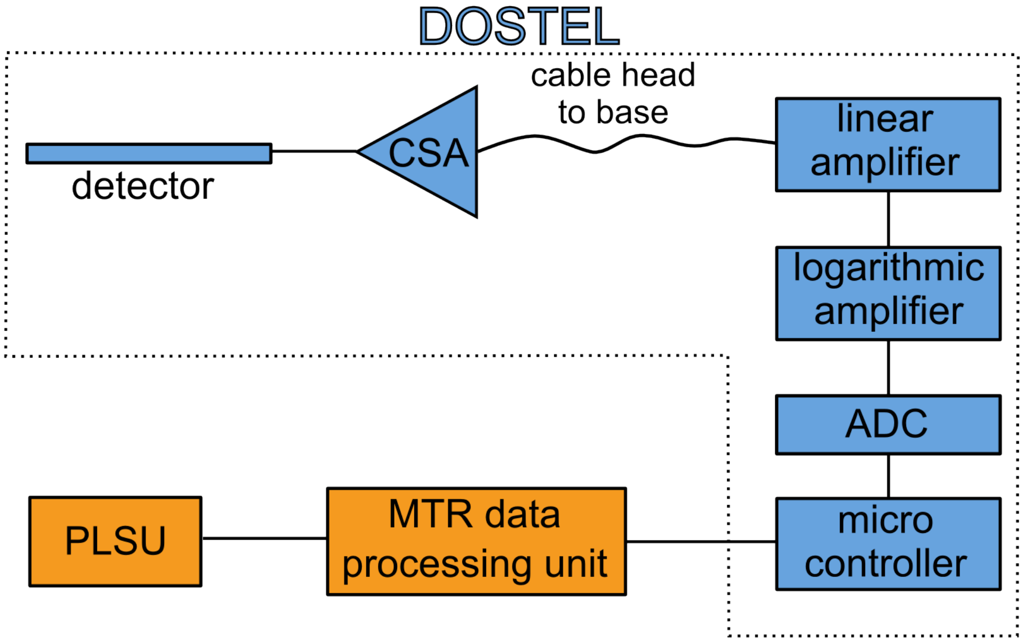

Figure 3.6.: Sketch of the DOSTEL electronics and data path. The charge signal from the detector is amplified and converted to a voltage pulse by a CSA. The voltage pulse is then again amplified by a linear amplifier and a logarithmic pulse amplifier and digitized by an ADC. The micro-controller stores the data. Every six hours the data is downloaded by the MTR data processing unit in a binary data format and stored on the Russian station computer (PLSU).

Table 3.1.: Energy calibration functions of the four DOSTEL detectors. The functions lead to the energy deposition ranges measurable with the detectors shown in column 3. For the telescope detectors (D1,D4) these energy ranges can be converted to LET in water.

Detector	Energy calibration function $/keV$	dE range / keV LET range / $(\frac{keV}{\mu m}$ in water)
Upper tele. detector (D4)	$dE_i = e^{(\frac{ch_i+117.83}{35.09})}$	$dE_i = [28.7, ..., 22612]$ $LET_i = [0.084, ..., 66.3]$
Lower tele. detector (D1)	$dE_i = e^{(\frac{ch_i+132.18}{35.24})}$	$dE_i = [42.5, ..., 51248]$ $LET_i = [0.061, ..., 73.5]$
Pin diodes (D2,D3)	$dE_i = e^{(\frac{ch_i+132.2}{34.85})}$	$dE_i = [44.4, ..., 56292]$ no path lenght limitation

The voltage pulse is then amplified by a linear preamplifier, before the final amplification by a logarithmic amplifier is conducted. The amplified signal is then digitized to 256 pulse height channels by a multiplexed 8-bit Analogue to Digital Converter (ADC). This signal processing allows a pulse height analysis of the detector signals with 256 logarithmic channels, which can be transferred to energy loss in the detectors with use of the energy calibration function shown in table 3.1. Due to a faulty design of the electronics not all 256 ADC channels can be used. The linear preamplifier reaches its upper limit of amplification which leads to clipping of the signal height. Due to the fact that the CSAs are dimensioned in a way that identical dE/dx in the detectors result in comparable pulse heights after the CSAs, the upper dE/dx limit for all detectors is $\sim 150 \, \frac{kev}{\mu m}$ in silicon (LET $\sim 70 \, \frac{kev}{\mu m}$). The ADC channel numbers are stored in a histogram (energy deposition histogram) by the micro-controller. The micro-controller further counts the total number of events in all detectors. This sum trigger is increased by 1 if there is a signal in any of the four detectors (in the later text the number of events counted during the acquisition time with the sum trigger of the DOSTEL will be called count rate). Every six hours the histograms and count rates are sent to the MTR data processing unit in binary data format. These binary data files are then sent to the ISS computer in the Russian segment (PLSU) and stored on a PCMCIA card. For MTR-1 the PCMCIA card was brought to ground by Soyuz TMA-6 on October 10th 2005. For the MTR-2B mission phase the return to ground was executed via Space Shuttle flight STS-126 on November 30th 2008.

DOSTEL Data Format

The MTR DOSTEL data is stored in 6-hour data files containing count rates and energy deposition histograms. There are two different modes for these 6-hour data packages: telescope-mode and single-mode (between which the DOSTEL switches alternately). It is important to point out that in Telescope-mode, only particles hitting both telescope detectors (D1,D4) are stored in the energy deposition histograms of D1 and D4. In Single-mode no coincidence condition is required. The PIN diodes (D2,D3) always act in Single-mode thus all particles hitting the PIN diodes are stored with no coincidence condition required for either of the PIN diodes.

The DOSTEL scientific data inside the 6-hour data packages is organized in blocks

for each integration period. Integration period in this case means the measurement time for one energy deposition histogram. During single and coincidence mode the DOSTEL can again operate in two different modes. These define the integration period, as well as the period for the sum trigger, and which energy deposition histograms are stored.
The standard mode is the GCR mode. During this mode the integration period of the energy deposition histograms is ~ 45 minutes starting and ending at the geomagnetic equator. This procedure is done on board by using the minimum in the count rates at the geomagnetic equator. The count rates during GCR mode are integrated over 100 seconds. The data Block size in GCR mode is 2 KBytes. They include one energy deposition histogram of one of the telescope detectors (D1,D4) and one energy deposition histogram of one of the PIN diodes (D2,D3). Each of these histograms has a size of 512 Bytes. The Block also contains a 48 Byte info part and 975 Byte of count rate data.
The SAA mode is designed to get separate data for crossings of the inner radiation belt in the region of the SAA. This mode is started by a threshold of the count rate slope. If the count rate increases stronger than the defined threshold the DOSTEL switches in SAA mode. This mode is ended if the count rate falls below an ending threshold. During this mode the integration period of the energy deposition histograms is defined by the start and the end of this mode. The integration period for the count rates is 20 seconds to get a higher time resolution. The Block size during SAA mode is 4 KBytes. The 512 Bytes energy deposition histograms of all four detectors are stored. These Blocks also contain a 48 Byte info part and have 1999 Byte reserved for count rate data.
When the DOSTEL switches to SAA mode one GCR data Block is interrupted. After the SAA mode the DOSTEL then switches back to GCR mode and writes the data in the same data Block as before. Thus, the data Block then contains two energy deposition histograms (one telescope detector, one PIN diode) with an integration time of ~ 45 minutes minus the integration time of the interrupting SAA mode Block.
To illustrate the different modes of data collection by DOSTEL an overview is given in table 3.2. Each 6-hour data package contains a time stamp of the data download from the MTR data processing unit. This time stamp is used to calcu-

Table 3.2.: Overview of different operation modes of DOSTEL. The single and telescope mode are alternately changing for the 6-hour data packages. The GCR and SAA modes can change during one 6-hour data package.

	Telescope mode (coincidence condition D1 and D4)	**Single mode** (no coincidence condition)
GCR mode	energy deposition histograms of D1,D2 or D4,D3 (alternating)	energy deposition histograms of D1,D2 or D4,D3 (alternating)
SAA mode	energy deposition histograms of D1,D2,D3 and D4	energy deposition histograms of D1,D2,D3 and D4

late the absolute time from the relative time in the data package. A more detailed presentation of the data time calculation follows in chapter 4.

DOSTEL Data Time Line

This section gives an overview about the DOSTEL data coverage during the MTR mission phases MTR-1 and MTR-2B. As already mentioned in the introduction of the MTR experiment the active instruments were used during these mission phases. The exposure time during MTR-1 started on February 26 in 2004 and ended on August 18 in 2005. This time period is sketched blue in figure 3.7. During this whole time period the passive detectors of MTR were exposed to the radiation field outside the ISS. Unfortunately the DOSTEL data do not cover the whole time period. The data recording started in April 2004. There is data available for April 13th, April 20th to June 9th and June 19th to June 30th 2004. After June 2004 a communication problem between the MTR data processing unit and the PLSU occurred and no new files for new DOSTEL data package were started. Nonetheless some of these data files could be recovered and data are available for 4 days in July (19th to 22nd) and from September 24th to October 8th 2004. These time periods are sketched red in figure 3.7. The DOSTEL data coverage for the MTR-2B mission phase inside the ISS is shown in figure 3.8 in the same color code as in figure 3.7.

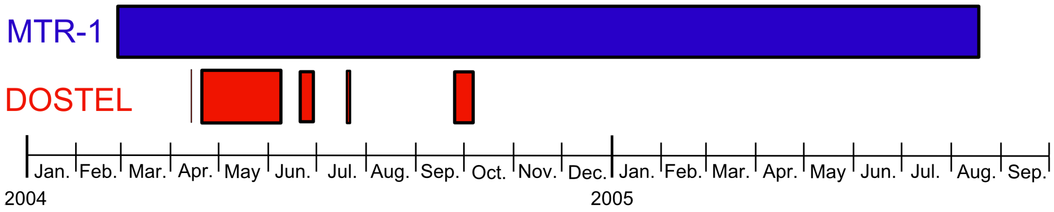

Figure 3.7.: Sketch of data coverage of DOSTEL during the MTR-1 mission phase. The exposure lasted from February 26th 2004 to August 18th 2005. DOSTEL recorded data on April 13th, from April 20th until June 9th, from June 19th to June 30th, from July 19th to 22nd and from September 24th to October 8th 2004. Additionally there are smaller data gaps between April 20th and June 30th, as well as between September 24th and October 8th. The total measurement time of DOSTEL during MTR-1 was 71 days.

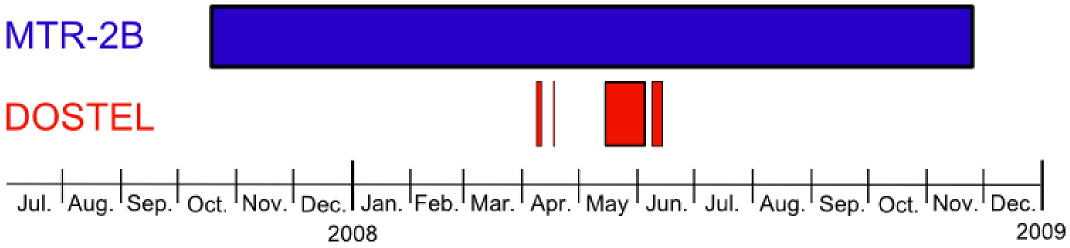

Figure 3.8.: Sketch of data coverage of DOSTEL during MTR-2B mission phase. The exposure lasted from October 18th 2007 until November 25th 2008. During this time the passive detectors of MTR were exposed to the radiation field inside the ISS. The DOSTEL has recorded data from April 8th to April 11th, April 17th and 18th, May 14th to June 6th and June 9th until June 15th. Due to additional data gaps the total measurement time of DOSTEL during MTR-2B was 31 days.

The exposure time started on October 18 2007 and ended on November 25 in 2008. For this mission phase DOSTEL data are available from April 8th until June 15th. For later comparison of results from DOSTEL and the passive detectors of MTR it is important to keep the different exposure times into account. The DOSTEL results reflect the radiation conditions during the time period of the measurement. The results for the passive detectors are integrated over the whole exposure time during the mission phases.

4. DOSTEL Data Time Correction

This chapter describes the time correction of the DOSTEL data packages. The relative time in the data has to be converted in an absolute time. As mentioned in the previous chapter, the absolute time can be calculated by using the download time of the data packages. The problem with this method is, that the download of the packages does not start exactly 6 hours after the start of the data acquisition. Every data package has a different time offset, which can be positive or negative. These time offsets result in an uncertainty of the absolute data time of around ± 15 minutes. Taking into account the periodicity of the ISS orbiting Earth, this time uncertainty would result in a angular deviation of 60° in longitude and 35° in latitude, and would make a angular correlation of the DOSTEL data meaningless. Therefor a time correction method was developed to lower the uncertainty in time to about 1 minute (4° longitude and 2° latitude). This was achieved by using the count rate dependence on the Effective Vertical Geomagnetic Cutoff Rigidity (R_c) and will be described in this chapter.

4.1. Count Rate Dependence on Geomagnetic Cutoff Rigidity

The number of particles detected in Low Earth Orbit (LEO) strongly depends on R_c and thus on the position of the measurement in LEO. At locations with a high R_c, fewer particles of the GCR are able to reach this place, and so a lower count rate is measured than at locations with a lower cutoff rigidity. In this analysis, theoretical GCR rigidity spectra j(R) are used to get an estimation for the count rate dependence on R_c. The used rigidity spectra for this investigation are illustrated in figure 4.1. Theoretical energy spectra were taken from *Usoskin et al.* (2005) and transferred to rigidity spectra by using equation 4.1.

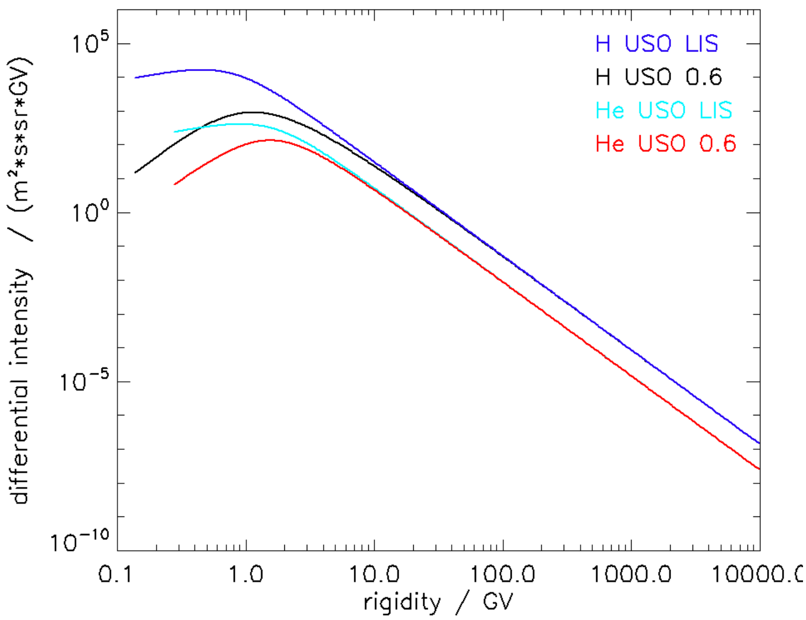

Figure 4.1.: Theoretical rigidity spectra of hydrogen and helium (*Usoskin et al.*, 2005). The differential intensity (particles per $m^2 \cdot s \cdot sr \cdot GV$) is shown as a function of the particle rigidity. The spectra marked with LIS are the Local Interstellar Spectra. The spectra for 1 AU were calculated from the LIS by using the force field method with a modulation potential of $\Phi = 0.6\ GV$.

The rigidity of a particle depends on the particle energy and particle species.

$$R = \frac{\sqrt{((E+E_0))^2 - E_0^2}}{z} \tag{4.1}$$

$$R = \text{ rigidity}/GV$$

$$E = \text{ energy}/GeV$$

$$m = \text{ mass number}$$

$$E_0 = \text{ rest energy} = m \cdot 0.94 GeV$$

$$z = \text{ charge number}$$

Local Interstellar Spectra (LIS) are transferred to rigidity spectra at 1 Astronomical Unit (AU) by using the force field method with a modulation potential of $\Phi = 0.6\ GV$. The modulation parameter and a description of the force field method are also explained in *Usoskin et al.* (2005). The modulated rigidity spectra show decreased differential intensities in comparison to the LIS. This

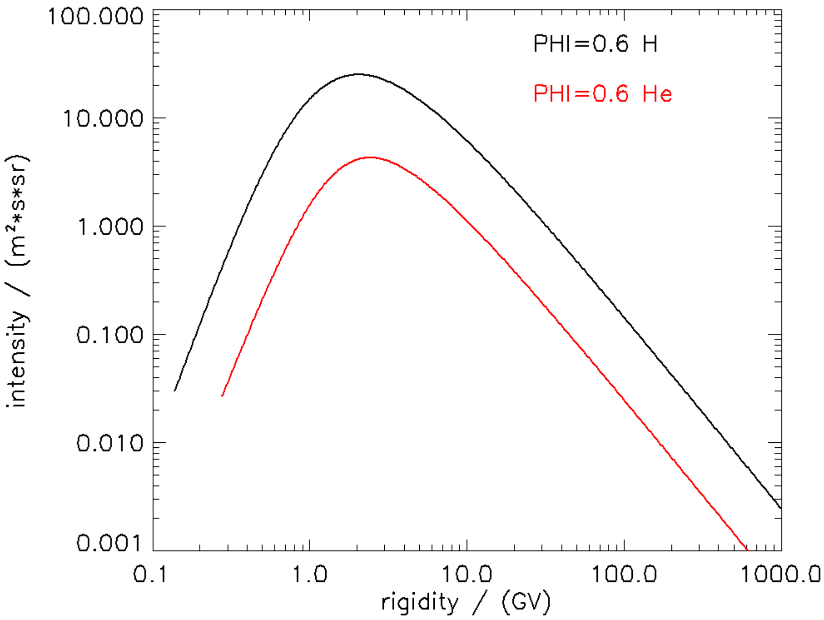

Figure 4.2.: Theoretical GCR intensity for hydrogen (black) and helium (red) at 1 AU in dependence on the particle rigidity R. The intensity is given in particle per $m^2 \cdot s \cdot sr$.

modulation is strongest for GCR particles with low rigidities and decreases with increasing particle rigidity. The high rigidity part of the differential intensity can be described by a power law with a spectral index of -2.77.

The goal of this analysis is to estimate dependency of the count rate on the vertical cutoff rigidity. It is suitable to convert the differential intensity into an intensity by a multiplication of the differential intensity with the bin width dR used in figure 4.1. The intensity (particles per $m^2 \cdot s \cdot sr$) of GCR particles in dependence of the particle rigidity is shown in figure 4.2. A multiplication by the bin width is an approximation for the integral of a function as the multiplication of the function values by the bin width gives the area below the function for these data points. Due to this, the intensity over rigidity shows a less steep decrease with increasing rigidity. For high rigidities the intensity can be described by a power law with the spectral index of -1.77. The spectral index is decreased by 1 compared to the spectral index of the differential intensity. This decrease can directly be calculated by building the antiderivative from a power law. The count rate dependence on the geomagnetic cutoff rigidity R_c can be derived from the intensity dependence on the particle rigidity R. For this, one has to make the assumption that only particles with rigidities greater or equal R_c can reach a detector placed at a location with R_c. This means the intensity spectra are cut off completely for rigidities below R_c. With this assumption the count rate dependency on the geomagnetic cutoff rigidity can be derived from figure 4.1 by summing up all count rates greater R_c:

$$N(R_c) = \int_{R_c}^{\inf} j(R) \cdot dR = \sum_{R_c} N(R) \text{ ; for } R \geq R_c \tag{4.2}$$

The result of equation 4.2 is the integrated intensity over the geomagnetic cutoff rigidity R_c. This means, for $R_c = 3$ GV all particles with rigidity greater or equal 3 GV are counted. Due to the fact that the intensity in figure 4.2 is given in particles per $m^2 \cdot s \cdot sr$ the integrated intensity describes the theoretical dependence on R_c for a detector with a geometric factor of 1 $m^2 \cdot sr$. To scale this result to any detector the geometric factor of this detector has to be multiplied with the result. The DOSTEL count rate describes the amount of particles hitting any of the four DOSTEL detectors. The geometric factor for this setup can be estimated by summing up all geometric factors of the single detectors and subtract the geometric factors for detector combinations.

$$\begin{aligned} G_{sum} &= G_{PIPS} + G_{PIPS} + G_{PIN} + G_{PIN} - G_{telescope} \qquad (4.3) \\ G_{sum} &= (21.77 + 21.77 + 7.26 + 7.26 - 8.24)\ cm^2 \cdot sr = 49.8 cm^2 \cdot sr \\ G_{sum} &\sim 0.005 m^2 \cdot sr \end{aligned}$$

In equation 4.3 the geometric factor for the DOSTEL count rate is calculated. The geometric factors for the PIPS detectors (21.77 $cm^2 \cdot sr$) and the PIN diodes (7.26 $cm^2 \cdot sr$) are summed up and the geometric factor for the telescope, formed by the PIPS detectors (8.24 $cm^2 \cdot sr$), is subtracted. The detector combinations including the PIN diodes were not included. Due to the fact that the PIN diodes are perpendicular to the PIPS detectors and to each other their combinations have very low geometric factors and therefor can be neglected for this calculation. The integrated intensity multiplied by the geometric factor of the DOSTEL (theoretical count rate) in dependence of the vertical geomagnetic cutoff rigidity is shown in figure 4.3. It shows the count rate dependencies for hydrogen (black), helium (red), as well as their sum (dark blue) in the R_c range covered by the ISS orbit (3 GV to 15 GV). The count rate cutoff dependence shows the expected behavior of highest count rates at lowest cutoff rigidities. The functional relation can be described by a power law with a spectral index of -1.55 (light blue). The spectral index is lower as the one expected for high rigidities (-1.77). This difference can be explained with the intensity spectra from figure 4.2. For rigidities between 3 GV and 15 GV the intensity spectra are less steep than for higher rigidities which means the spectral index for these rigidities is lower.

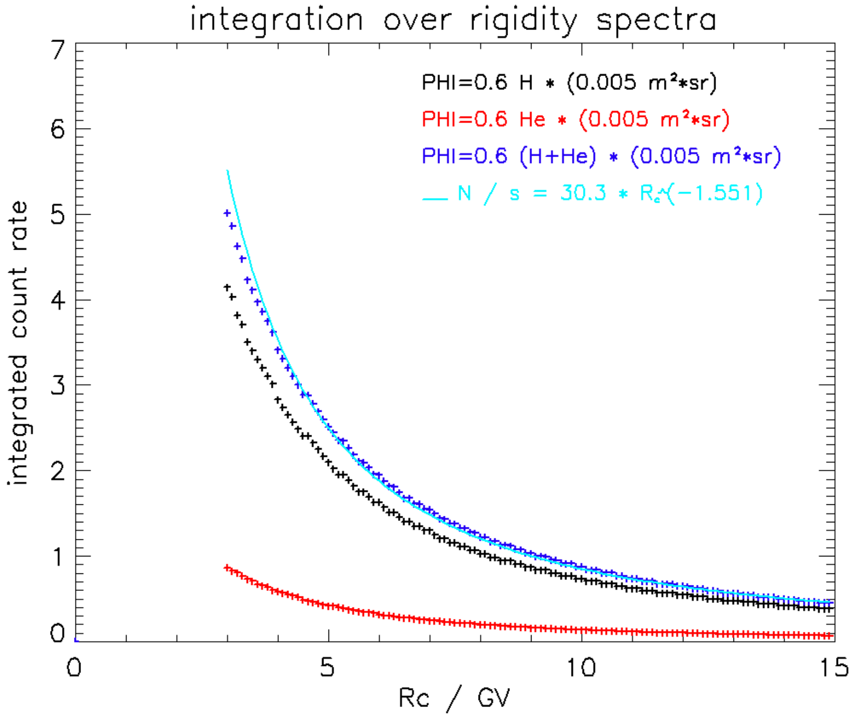

Figure 4.3.: Theoretical DOSTEL count rate dependence on the geomagnetic cutoff rigidity. The count rate dependence for hydrogen (black), helium (red), and their sum (blue) are shown. The functional relation of integrated count rate and cutoff rigidity can be described by a power law with a spectral index of -1.55 (cyan).

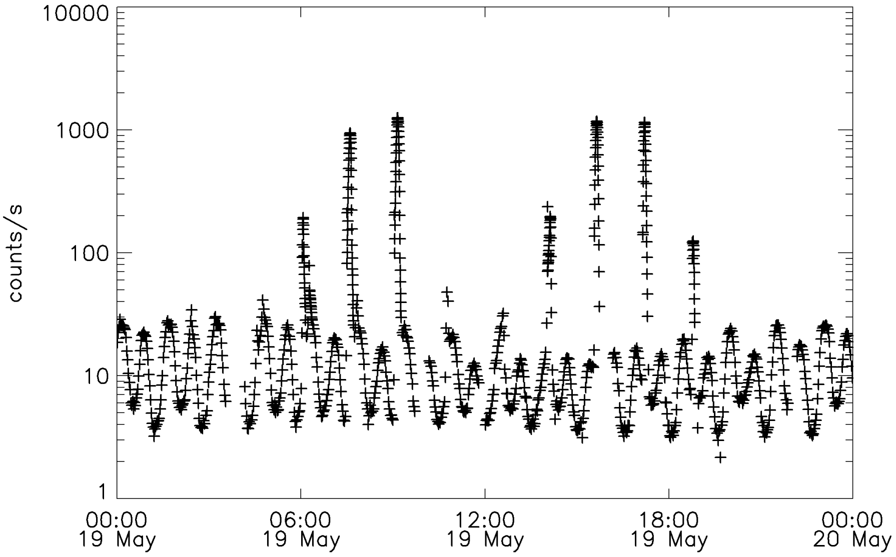

Figure 4.4.: Time profile of count rates measured by DOSTEL on May 19th 2004. The dependence on the geomagnetic cutoff rigidity can be seen in the 45 minutes modulation of the data. The spikes in the count rate result from crossings of the inner radiation belt in the region of the SAA.

4.2. Count Rate R_c Dependence for MTR-DOSTEL

The count rate measured with DOSTEL depends on the geomagnetic cutoff rigidity. This can be seen in figure 4.4. Excluding the count rate spikes correlated to passages through the inner radiation belt one gets the count rate profile of GCR particles. This time profile shows a wave like behavior with maxima every 45 minutes. This is the time span of one half-orbit of the ISS, this means the time between the northernmost and southernmost position of the ISS. At highest latitude the R_c is the lowest and the highest count rate is expected. This count rate R_c dependence can be used to apply a time correction method on the DOSTEL data. The relation between count rate and R_c can be generated for every 6-hour data file for different time offsets applied on the DOSTEL data. For this, orbit data of the ISS is used to get the location and thus the R_c values (shown in figure 2.3) of the measurement interval. With this approach it is possible to plot the measured count rate against the effective vertical geomagnetic cutoff rigidity, as can be seen in figure 4.5. This plot shows a broad distribution - the count rate cutoff relation is not comparable to the theoretical relation shown in figure 4.3.

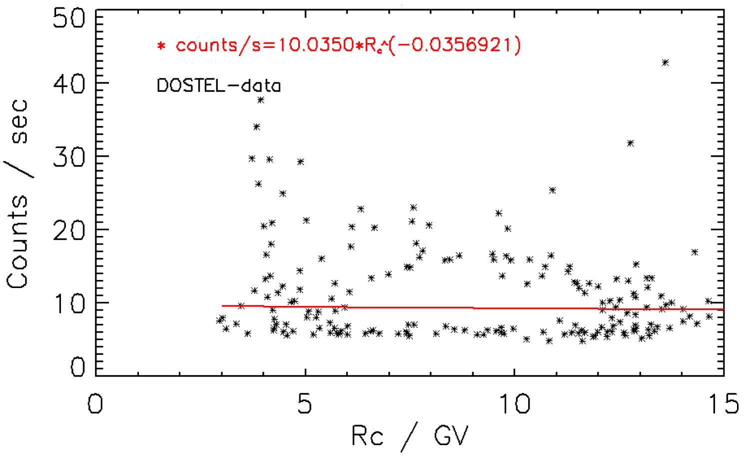

Figure 4.5.: Count rate cutoff relation measured by DOSTEL. One can see a broad distribution, which is not comparable with the theoretical relation from figure 4.3. For this data package an offset time of +30 minutes was used. The red line shows a power law fit through the data points.

To get a measure for the narrowness of the distribution, the data is fitted, in consideration of the theoretical relation, with a power law (in red in figure 4.5) and the mean distance of the data points in respect to the fit were used as a degree of narrowness. The used fitting function has the form:

$$N = A \cdot R_c^B \tag{4.4}$$

$$\begin{aligned} \mathrm{N} &= \text{counts per second} \\ \mathrm{R}_c &= \text{vertical cutoff rigidity} \end{aligned}$$

This function was fitted through the data points for time offsets between +30 and -30 minutes in one minute steps. For every data package 61 time offsets were used to plot the count rates against the cutoff rigidity. For each plot the narrowness was measured by the chi square of all data points to the fitting function. A result of this narrowness over time offset can be seen in figure 4.6. The time offset with the lowest chi square should be the one with the narrowest distribution and so the suitable time offset for the calculation of the absolute data time. Figure 4.7 shows the same plot for the same data package but for the time offset found in figure 4.6 (-5 minutes), as figure 4.5. The narrow distribution shows that the chosen time offset is appropriate. The figures 4.5 to 4.7 show the time correction for one MTR-DOSTEL 6-hour data package as an example. The time correction was

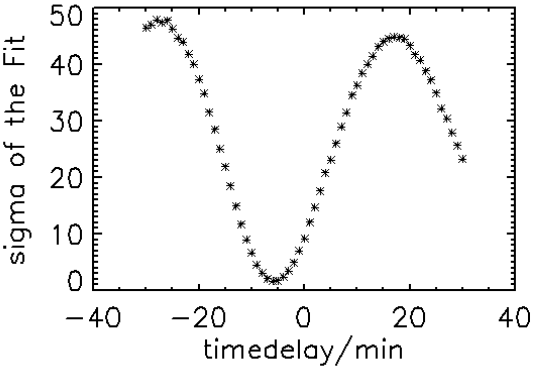

Figure 4.6.: Fit quality against the used time offset. The closest distribution to the fitting function results from a time offset of -5 minutes.

applied to all 6-hour data packages for the MTR-1 mission phase (see Appendix C) and the determined time offsets were applied to the data (count rate and energy loss spectra).

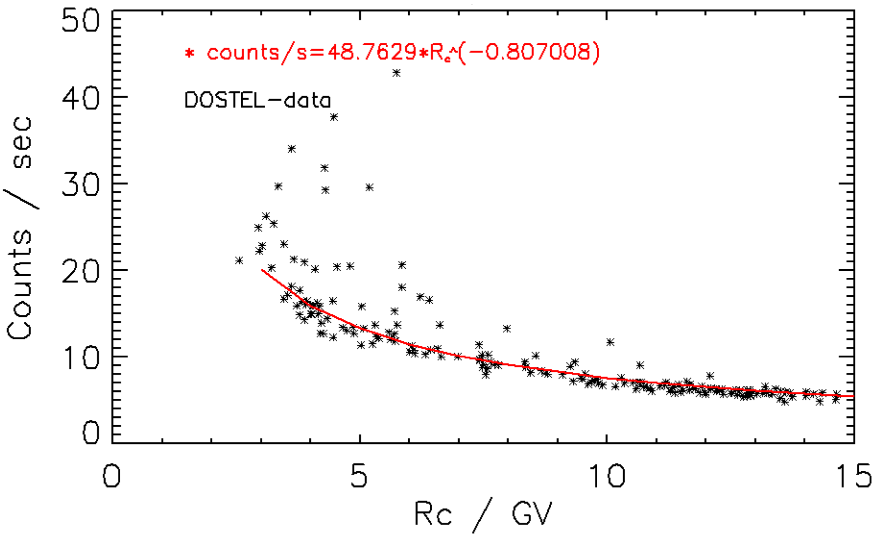

Figure 4.7.: Count rate cutoff relation for the same data package as in the previous figure. An offset time of -5 minutes results in a narrow distribution. This time offset of -5 minutes is the correct one for this data package. In red one can see a power law fit (with spectral index of -0.8) through the data points.

4.3. Comparison of Measured and Theoretical Count Rate R_c Dependence

Before starting the analysis of the time corrected DOSTEL data, a comparison of the measured count rate dependence on the effective vertical geomagnetic cutoff rigidity with the theoretical one will be conducted. The theoretical count rate R_c dependence derived from GCR energy spectra is shown in chapter 4.1.

$$N(R_c)_{theo} = 30.3 \cdot R_c^{-1.551} \tag{4.5}$$

The measured count rate R_c dependence can be seen in figure 4.7.

$$N(R_c)_{DOSTEL} = 48.8 \cdot R_c^{-0.8} \tag{4.6}$$

To compare the two results both are presented in figure 4.8 in double log scale.

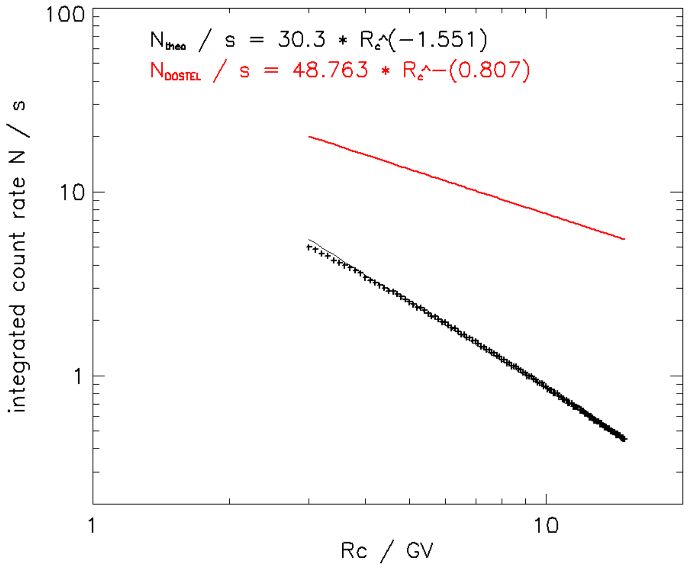

Figure 4.8.: The theoretical count rate R_c dependence (black) is compared to the measured one with DOSTEL (red).

The count rate R_c dependence measured with DOSTEL (red) has a lower spectral index (-0.8) than the theoretical one (-1.55). In addition DOSTEL generally shows higher count rates than expected from the theoretical result. The higher count rate can be explained by secondary particle production in the material of the ISS. To give a qualitative estimation of the number of secondary particles per

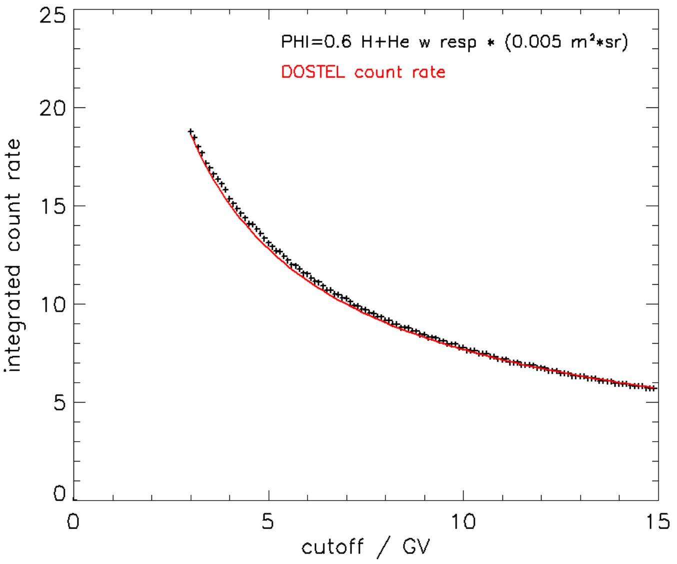

Figure 4.9.: Theoretical count rate R_c dependence for energy spectra multiplied by the DOSTEL yield function (in black). As comparison the relation measured with DOSTEL is shown in red.

primary particle, the GCR particle spectra in figure 4.1 can be multiplied by a function F(R) to repeat the analysis of chapter 4.1 with these new spectra. This approach was taken from (*Caballero-Lopez and Moraal*, 2012).

$$N(R_c)_{yield} = \int_{R_c}^{\mathrm{inf}} j(R) \cdot F(R) \cdot dR \tag{4.7}$$

Figure 4.9 shows the integrated count rate plotted against R_c for GCR energy spectra multiplied by a yield function F(R) in black. The comparison with the measured relation (red) shows a good agreement - which means it is possible to describe the measured count rate R_c dependence with this method. The used function F(R) depends on the particle rigidity and can be seen in equation 4.8.

$$F(R) = 1 + 0.33 * R \tag{4.8}$$

For example, one primary GCR particle with a rigidity of 3 GV generates two counts in the DOSTEL detectors. This ratio increases for increasing particle rigidity, as higher energetic particles can produce more secondary particles.

4.4. Corrected Count Rate Profiles Measured by MTR-DOSTEL

The time corrected DOSTEL data can be used for further analysis. One example is the geographic distribution of the count rates. For this the time corrected count rate data and ISS orbit data are used to find the position corresponding to each count rate value. The geographic distribution for the count rates of May 2004 during MTR-1 mission phase is shown in figure 4.10. The dependency on the geomagnetic cutoff can be seen in this plot as well. The lowest count rates are found at the geomagnetic equator and the highest count rates can be observed closest to the magnetic poles, over North America and south of Australia. The count rates at the geomagnetic equator are depending on the longitude. The count rates over India are lower than the ones on the opposite side of the Earth. This is due to the shift of the magnetic dipole axis towards the western Pacific (see chapter 2.2).

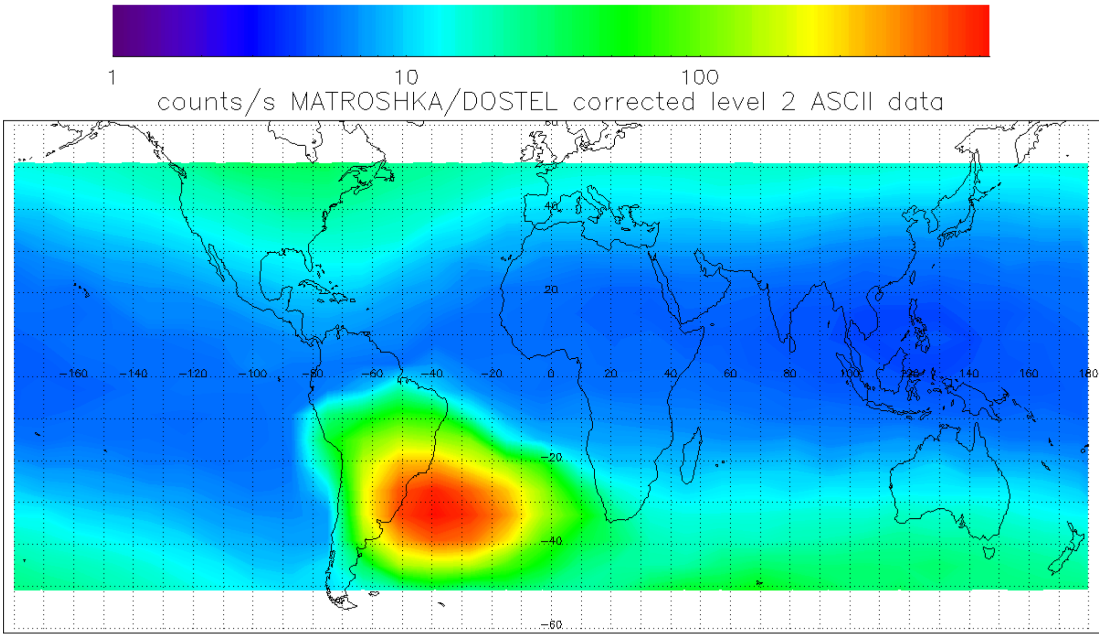

Figure 4.10.: Geographical count rate distribution for May 2004 during the MTR-1 mission phase. The shown count rate is the sum trigger rate mentioned in chapter 3.1. This means all particles hitting any of the four detectors are counted.

Furthermore the passages through the inner radiation belt in the region of the SAA clearly dominates the count rate distribution. The count rates in this region are more than one order of magnitude higher than the count rates close to the poles.

The corrected count rate can also be used to investigate the count rate dependence on the McIlwain L-parameter. For this, the effective vertical geomagnetic cutoff rigidity R_c (shown in figure 2.3) can be converted into the McIlwain L-parameter as described in formula 4.9.

$$L = \left(\frac{R_c}{16.237} \right)^{\frac{-1}{2.0352}} \tag{4.9}$$

The dependence of the DOSTEL count rate measured in May 2004 on the L-parameter is shown in figure 4.11. The count rate contribution of GCR particles (black) increases for increasing L-values. Low L-parameters belong to equatorial regions and thus show the lowest count rate. This behavior can not be seen in the trapped particle contribution (shown in red). The increased count rates of crossings of the inner radiation belt in the region of the SAA belong to L-parameters between 1.2 and 2.0. This is the typical L-value for the inner radiation belt found in literature, for further description see chapter 2.3. In addition increased count rates at L-values between 3 and 5 can be seen. They belong to edge crossings of the outer radiation belt.

Unfortunately the time correction procedure was not possible for the MTR-2B mission phase. Due to noise problems in one of the detectors the count rate was increased by one order of magnitude and thus the count rate modulation by the geomagnetic cutoff rigidity could not be resolved anymore. Therefore a time correction and thus a calculation of second level count rate data products, e.g. 2-D distribution or the dependence of the McIlwain parameter, is not possible. Nevertheless, the time corrections offsets does not affect the daily dose rate calculations which will be presented in the next chapter (5).

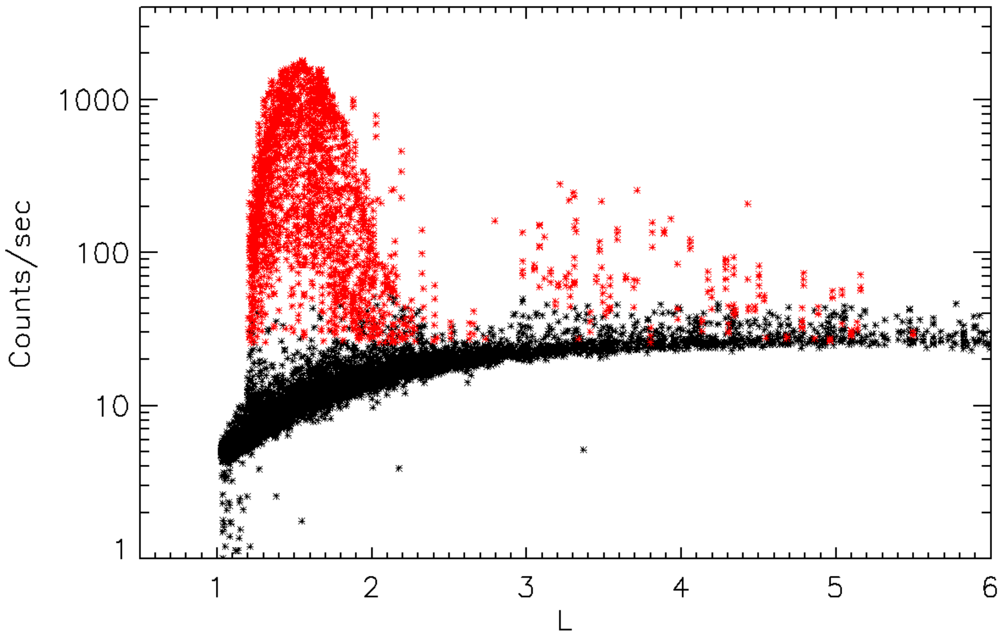

Figure 4.11.: MTR-DOSTEL count rate over the McIlwain L-parameter for May 2004 during the MTR-1 mission phase. The GCR component is shown in black. The trapped particle component is shown in red. The highest count rates belong to L-values between 1.2 and 2.0, which is the region of the inner radiation belt (see chapter 2.3).

5. DOSTEL Dose Measurements and Calculations

In this chapter the calculation of the absorbed dose D and the dose equivalent H based on the DOSTEL data products will be described. As already mentioned in chapter 3.1, DOSTEL measures energy deposition spectra separately for the GCR and the trapped particle component (SAA). The recorded count rates and energy deposition spectra are written to 6 hour data files (see chapter 3.1). Furthermore, DOSTEL operates in two different modes. In telescope mode DOSTELs telescope detectors work in coincidence, which means that only particles hitting both PIPS detectors are stored in their energy deposition spectra. In single mode, no coincidence condition is requested. Thus, all particles contribute to the energy deposition spectra. DOSTEL changes its mode after each 6 hour data package. A more detailed description of the count rate, as well as absorbed dose rate differences between the two modes, is given in chapter 6.

5.1. Absorbed Dose Calculation

The absorbed dose can be calculated from the energy deposition spectra recorded in single mode. The energy loss of all particles hitting the detector is stored in these spectra. To calculate the absorbed dose for one integration period one has to integrate the product of the deposited energy (dE_i) times the number of particles (N_i) over all ADC channels and divide this by the detectors mass dm (see formula 5.1). To convert the ADC channel into the energy deposit the calibration functions shown in chapter 3.1 are used.

$$D_{Si} = \sum_{i=0}^{255} \frac{dE_i \cdot N_i}{dm} = \sum_{i=0}^{255} \frac{dE_i \cdot N_i}{dV \cdot \rho} = \sum_{i=0}^{255} \frac{dE_i \cdot N_i}{A \cdot d \cdot \rho} \tag{5.1}$$

In formula 5.1 dV is the volume of the detector, ρ the density of silicon ($2.33 \frac{g}{cm^2}$), A the area of the detector (e.g., 6.93 cm^2) and d the thickness of the detectors (e.g., 154 μm). To end up with the SI-unit Gray it is necessary to convert the deposited energy from keV into Joule ($keV = 1.6022 \cdot 10^{-16} J$) and to use the mass dm in kg. The absorbed dose rate ($\dot{D}$), relevant for radiation protection, can be calculated by dividing the absorbed dose by the time of measurement (for measurements in LEO, the absorbed dose rate is usually given in $\mu Gy \cdot day^{-1}$). To convert the absorbed dose in silicon D_{Si} into absorbed dose in water D the following equation is used:

$$D = D_{Si} \cdot F_{Si->water} = D_{Si} \cdot 1.21 \tag{5.2}$$

The factor $F_{Si->water}$ of 1.21 results from different stopping powers (*ICRU*, 1984) for electrons and protons in silicon and water. This constant factor is an average over all LETs for protons and electrons and is described in (*Beaujean et al.*, 1999a).

5.2. Dose Equivalent Calculation

To calculate the dose equivalent H the LET dependent quality factor Q(LET) (see formula 2.12) is needed. Due to LET dependence of Q the energy deposition spectra measured in the telescope mode have to be used. In the telescope mode particles have to hit both telescope detectors. This limits the incident angle (α) of the particle to 62° (see chapter 3.1). The limited incident angle α also limits the possible path length dl in the detector ($dl = d \cdot cos(\alpha)^{-1}$, where d is the detector thickness). For isotropic particles the mean incident angle is $\langle \alpha \rangle = 30°$ (see chapter 6.2.2) and the mean path length in the detector is $dl = 1.15 \cdot d$. This limited path length allows to determine the LET by dividing the deposited energy by the mean path length in the detector. Every ADC channel i is converted to dE_i by using the energy calibration function (see chapter 3.1). For the calculation of the LET in water the conversion factor (equation 5.2) and the density ratio of water and silicon is needed:

$$LET_i = \frac{dE_i}{dl} \cdot F_{Si->water} \cdot \frac{\rho_{H_2O}}{\rho_{Si}} = \frac{dE_i}{dl} \cdot 1.21 \cdot \frac{1}{2.33} \tag{5.3}$$

An LET spectrum showing the differential particle intensity over the LET in water is presented in figure 5.1 (in black). In addition, the quality factor function (equation 2.12) is plotted in red. Every LET$_i$ has a dedicated Q_i given by this

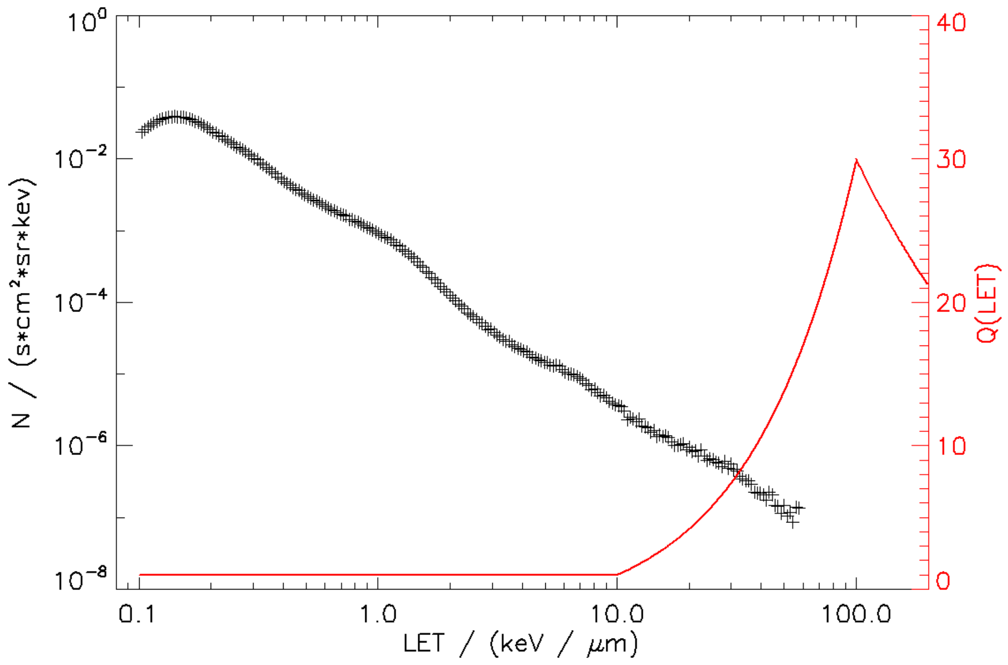

Figure 5.1.: LET spectrum of the GCR component. The differential intensity is plotted in black (quantity is shown on the left y-axis) against the LET in keV / μm in water (on the x-axis). In addition the ICRP60 Quality factor function (equation 2.12) is shown in red. One can see on the right y-axis that the maximum of this function is 29.8 and corresponds to the LET value of 100 keV / μm.

function. The dose equivalent measured in telescope mode can be calculated in the same way as the absorbed dose in the previous section:

$$H_{Si-tele} = \sum_{i=0}^{255} \frac{dE_i \cdot N_i \cdot Q_i}{dm} = \sum_{i=0}^{255} \frac{dE_i \cdot N_i \cdot Q_i}{dV \cdot \rho} = \sum_{i=0}^{255} \frac{dE_i \cdot N_i \cdot Q_i}{A \cdot d \cdot \rho} \tag{5.4}$$

$$H_{tele} = H_{Si-tele} \cdot F_{Si->water} = H_{Si-tele} \cdot 1.21 \tag{5.5}$$

This calculated dose equivalent H_{tele} is indexed with the word *tele* to distinguish it from the real dose equivalent H. For the calculation of H_{tele} only particles hitting both telescope detectors were used. To scale this value to the whole amount of particles the ratio of the geometric factors (see chapter 3.1) from the single and the telescope detector would be necessary. But this can only be achieved if the radiation field is isotropic (see chapter 6). To avoid this scaling factor, an other approach was used. The absorbed dose in water for particles hitting both telescope detectors (D_{tele}) is calculated from the energy deposition spectra measured in telescope mode. By dividing H_{tele} by D_{tele} one gets the mean quality factor $\langle Q \rangle$, which is the ratio between dose equivalent and absorbed dose for particles hitting both telescope detectors of DOSTEL.

$$\langle Q \rangle = \frac{H_{tele}}{D_{tele}} \tag{5.6}$$

This ratio can also be assumed as to be the ratio between dose equivalent and absorbed dose for all particles measured with DOSTEL. With this assumption one can calculate the real dose equivalent H for all particles by using the following formula.

$$H = D \cdot \langle Q \rangle \tag{5.7}$$

This mean quality factor $\langle Q \rangle$ was used to convert the absorbed dose in water D into dose equivalent H for all four detectors of DOSTEL.

To show the effect of Q(LET), figure 5.2 illustrates the integrated absorbed dose (black) and the integrated dose equivalent (red) rate. The integrated absorbed dose for example means that for LET_k the sum in equation 5.1 is calculated from 0 to k. At 10 $keV \cdot \mu m^{-1}$ the integrated dose equivalent rate increases stronger than the integrated absorbed dose rate due to the quality factor Q. The last data points in figure 5.2 then show the total (k=0 to 250) dose equivalent and absorbed dose rates. Their ratio gives the mean quality factor $\langle Q \rangle$.

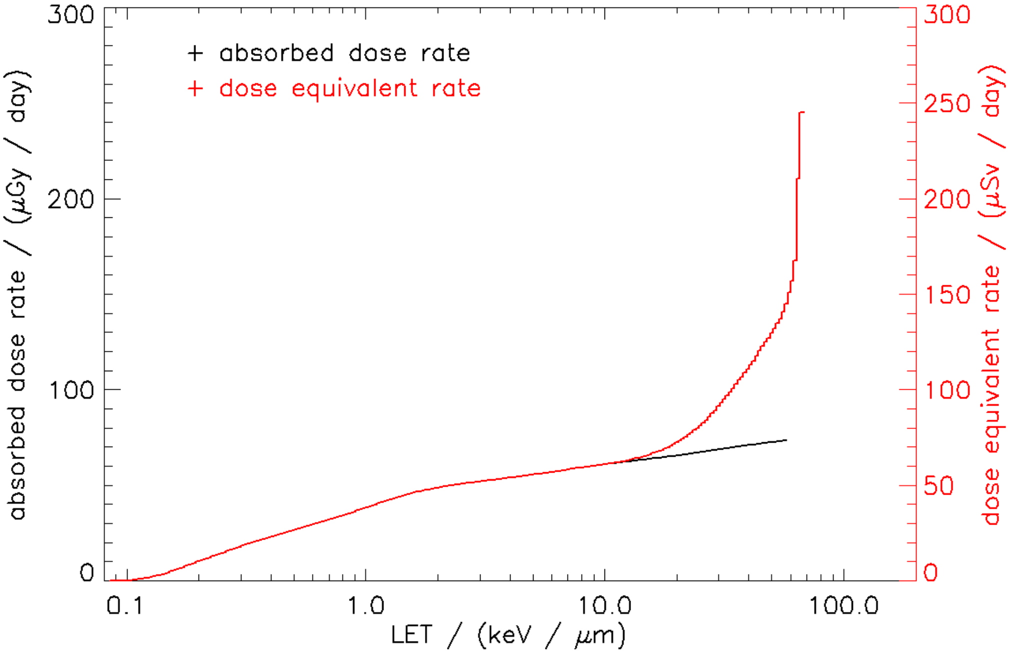

Figure 5.2.: Integrated absorbed dose rate $\dot{D}_i$ and integrated dose equivalent rate $\dot{H}_i$ of the GCR component. On the X-axis the LET is shown in keV / μm in water. At 10 (keV / μm) the increase of $\dot{H}$ is higher than the increase of $\dot{D}$. This is due to the quality factor Q which starts to increase at this LET.

5.3. Dose Values

In this section the final MTR dose values are presented. For MTR-1 the data from April 13th to June 30th 2004 were analyzed, while the data from September and October 2004 will be discussed in chapter 7. From April to June 2004 no major solar event occurred and the solar cycle was decreasing from solar maximum. For MTR-2B the whole DOSTEL data set from April 8th to June 15th 2008 was used. In this time Sun was near solar minimum condition.

The dose values have been calculated as described in the previous sections for every 6-hour data package. From this values daily averages were determined and dead-time corrected as described in Appendix B. Daily averages in this case means the amount of dose measured at that day, e.g., the daily absorbed dose for trapped particles (SAA) is the amount of dose deposited during the crossings of the inner radiation belt ($\sim$ 80 minutes). The daily averaged absorbed dose induced by the GCR component for all four DOSTEL detectors for May 2004 during MTR-1 mission phase is shown in figure 5.3. The four detectors show comparable absorbed dose values. The differences can be explained by different times of the measurements. In GCR mode the DOSTEL measures the energy deposition spectra of one of the telescope detector and one of the PIN diodes at the same time. In the next 45 minute measurement interval the energy deposition spectra of the other telescope detector and PIN diode are stored. This alternating data collection can lead to differences in the daily averages, especially during days with incomplete data coverage, due to the longitudinal variation of R_c. To minimize the described effects for further analysis the daily mean values have been averaged over all four DOSTEL detectors. The averaged absorbed dose values for the GCR and the trapped particle (SAA) contribution for both MTR mission phases are shown in figure 5.4. To obtain better statistic, especially for the trapped component, these plots show data averaged over 2 days. A comparison between MTR-1 and MTR-2B shows an enhanced contribution from the GCR component during the MTR-2B mission phase, where the MTR phantom was inside the Zvezda module of the ISS. The higher absorbed dose with respect to the outside measurement during MTR-1 can be explained by the solar cycle. During MTR-2B in 2008 the sun was in solar minimum condition, which leads to higher absorbed doses due to higher GCR fluxes. The shielding of the ISS has a minor effect on the GCR contribution to the absorbed dose. The trapped

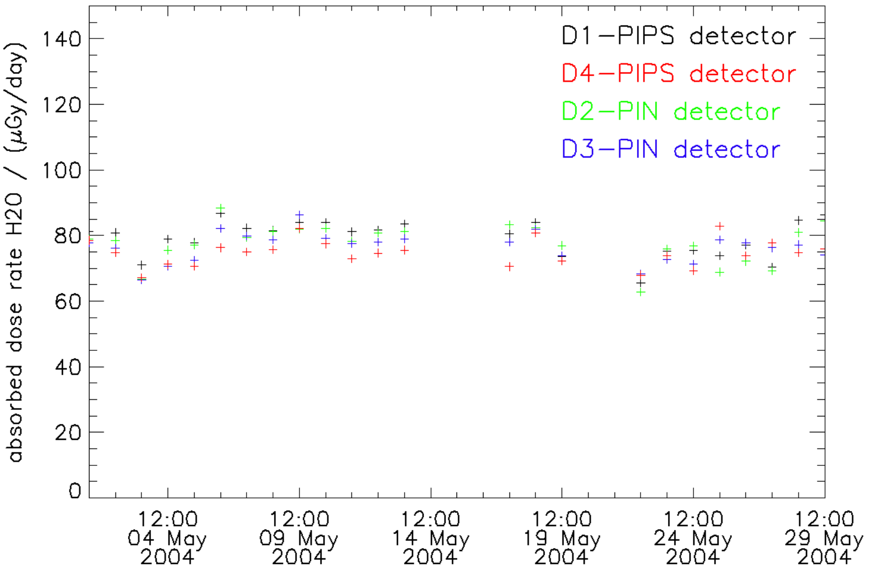

Figure 5.3.: Daily averaged GCR induced absorbed dose rate of all four DOSTEL detectors for May 2004 during the MTR 1 mission phase. All four detectors show comparable results.

component shows a strong decrease from outside to inside measurements. For the trapped protons, which have energies of up to a few hundred MeV, the shielding of the station hull is very effective. The absorbed dose induced by trapped particles of the inner radiation belt in the region of the SAA show a strong variation. This variation results from geographical differences of the ISS orbit when crossing the SAA region. Figure A.5 in appendix A shows that the absorbed dose per count (in this case the sum trigger) averaged over a whole day can be approximated as a constant value ($1.85 \cdot 10^{-4} \frac{\mu Gy}{count}$). The daily absorbed dose variation thus results from variations of the total number of particles measured during SAA crossings. The geographical count rate distribution (figure 4.10) shows a maximum count rate in the center of the SAA region decreasing to the rim. The ISS orbits through the SAA region (7 to 8 orbits) show diurnal geographical variations and thus the number of particles and the measured absorbed dose show these variations, too. The mean dose values, averaged from April 13th to June 30th 2004 for MTR-1 (53 days of data) and from April 8th to June 15th 2008 (31 days of data), are shown and discussed in the following section. The mean values of the absorbed dose rate, the dose equivalent rate and the mean quality factors are shown in table 5.1

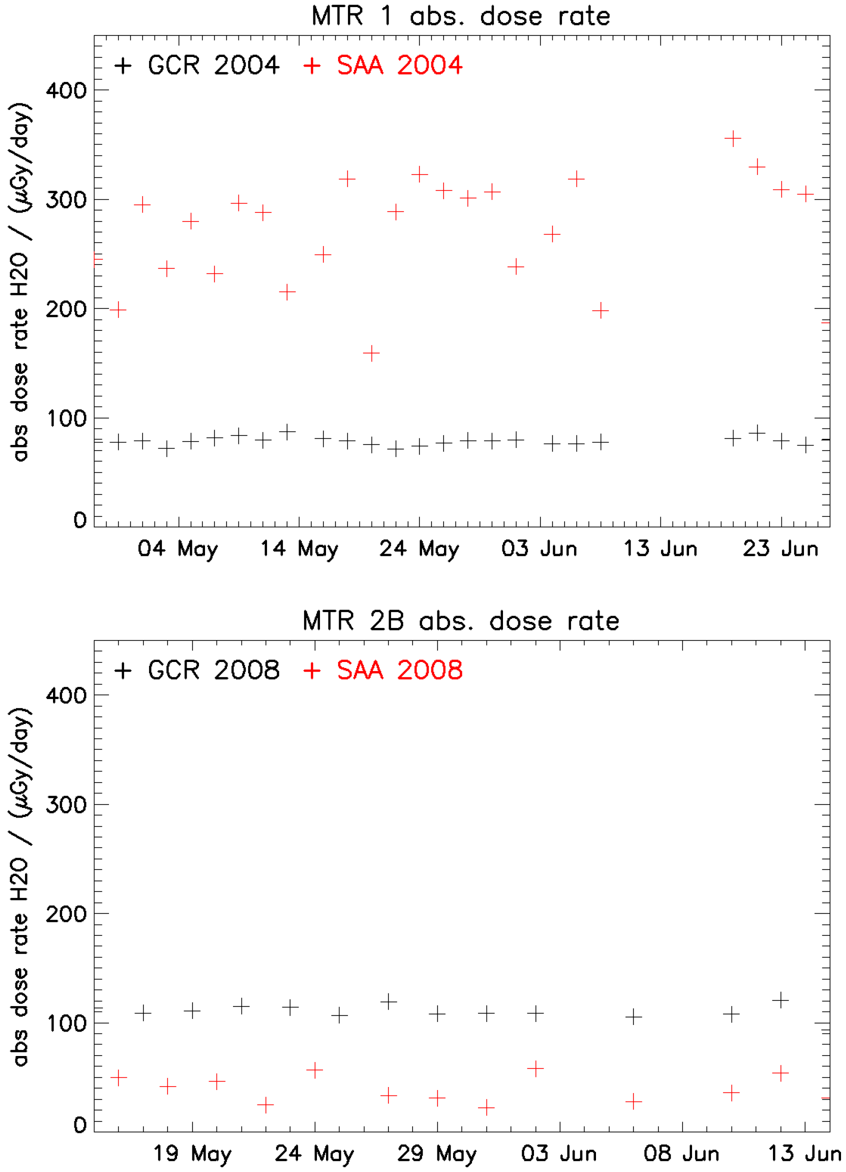

Figure 5.4.: Absorbed dose rate for MTR-1 (April 27th to June 27th) and MTR-2B (May 15th to June 14th) (averaged over all four DOSTEL detectors and two days).

for the MTR-1 and in in table 5.2 for the MTR-2B data. The contribution of the GCR and the trapped component as well as their sum (total radiation exposure) are shown.

5.3.1. MATROSHKA-1

Table 5.1.: Absorbed dose rate $\dot{D}$ and the dose equivalent rate $\dot{H}$ for the GCR and the SAA component as well as the sum of both (total) for the time period from April 13th to June 30th 2004 during the MTR-1 mission phase.

MTR 1	$\dot{D}$ / $(\mu Gy \cdot day^{-1})$	$\dot{H}$ / $(\mu Sv \cdot day^{-1})$	$\langle Q \rangle$
GCR	77.6	245.5	3.16
SAA	296.1	367.1	1.24
total	373.7	612.3	1.64

During the MTR-1 mission phase, where the MTR phantom was mounted outside the Zvezda module in 2004, the dominant contribution to the absorbed dose was induced by trapped particles during crossings of the inner radiation belt in the region of the SAA. This contribution with 296 $\mu Gy \cdot day^{-1}$ deposits 80% of the absorbed dose rate, while the contribution of GCR particles, 78 $\mu Gy \cdot day^{-1}$, only amounts to 20% the total absorbed dose rate. Due to the lower LET of the trapped protons (LET $> 10 \frac{keV}{\mu m}$) with respect to the GCR, the mean quality factor for the trapped contribution is lower. With a mean quality factor of 1.24 the dose equivalent rate from trapped particles is 370 $\mu Sv \cdot day^{-1}$ which is 60% of the total dose equivalent rate. The higher biological effectiveness of the energy deposition by GCR particles can be seen in the higher mean quality factor of 3.16. This quality factor leads to a dose equivalent rate from the GCR contribution of 245 $\mu Sv \cdot day^{-1}$, which is 40% of the total dose equivalent rate.
MTR was the only experiment with instrumentation for dose measurement mounted outside the ISS in the mission time of MTR-1. A comparison to similar data sets is only possible with data from the passive dose meters of the MTR experiment (*Reitz et al.*, 2009) and (*Berger et al.*, 2013). The passive detectors in similar position as the DOSTEL show higher absorbed dose rates than DOSTEL.

The absorbed dose for the skin of the MTR phantom (944 $\frac{\mu Gy}{day}$) is more than two times higher than the results obtained with DOSTEL (*Reitz et al.*, 2009). The DOSTEL is slightly better shielded in respect to the skin detectors, so that the expected results for DOSTEL should be lower than skin dose measured with the passive dosimeters. But even the absorbed dose measured with TLDs next to DOSTEL at the head of the phantom is higher (540 $\frac{\mu Gy}{day}$) than the absorbed dose measured with DOSTEL (*Berger et al.*, 2013), although the TLDs can only measure up to 10 $\frac{keV}{\mu m}$. These differences in the absorbed dose follow from temporal changes of the radiation field in LEO and are discussed in detail in chapter 6.

5.3.2. MATROSHKA-2B

Table 5.2.: Absorbed dose rate $\dot{D}$ and the dose equivalent rate $\dot{H}$ for the GCR and the SAA component as well as the sum of both (total) for the time period from April 8th to June 15 th 2008 during MTR-2B mission phase.

MTR 2B	$\dot{D}$ / $(\mu Gy \cdot day^{-1})$	$\dot{H}$ / $(\mu Sv \cdot day^{-1})$	$\langle Q \rangle$
GCR	115.6	309.8	2.79
SAA	45.8	72.4	1.58
total	161.4	382.2	2.37

The MTR phantom was mounted inside the Zvezda module of the ISS during the MTR-2B mission in 2008. The dose values obtained with DOSTEL are shown in table 5.2. A noise problem in one of the telescope detectors made DOSTEL switch into the mode for trapped particles randomly and thus led to a problem in the separation between GCR and trapped particles. The separation was therefore done by using the differences in the shape of the LET spectra of the GCR and the trapped particle component. This method enables to identify GCR and SAA energy deposition spectra. Due to the random mode switch from GCR mode to SAA-mode, some energy deposition spectra, dominated by the GCR or trapped particle component, can additionally contain a smaller amount of the other component's particles. These "‘mixed"’ spectra can not be distinguished from "‘pure"’ spectra, and thus, some of the GCR contribution is counted as trapped and some of the trapped component is counted as GCR component. This effect leads to uncertainties in the ratio of GCR and trapped component, whereas the total absorbed dose and dose equivalent rates are not effected.

During the MTR-2B mission phase 4 Russian DB-8 dosimeter units, based on Silicon semiconductor detectors, were operating inside the Zvezda module (*Lishnevskii et al.*, 2010). All four devices measured an absorbed dose rate induced by GCR particles of 100 $\mu Gy \cdot day^{-1}$. These results are 15 % lower than the absorbed dose rate measured with DOSTEL during the same time period. This can be explained by the lack of accuracy in the separation of the two contributions to the absorbed dose by DOSTEL. For example, some of the absorbed dose induced by trapped particles might have been counted as GCR contribution, and thus, the measured absorbed dose rate is too high for the GCR and too low for the trapped component.

The four DB-8 units show strong variations in-between their measured dose induced by trapped particles. The dose value strongly depends on the shielding at the location of the instrument. The measured absorbed dose rate varies from 60 $\mu Gy \cdot day^{-1}$ for the best shielded to 180 $\mu Gy \cdot day^{-1}$ for the least shielded instrument. The total absorbed dose rate measured with the best shielded DB-8 unit (100 $\mu Gy \cdot day^{-1}$+ 60 $\mu Gy \cdot day^{-1}$ = 160 $\mu Gy \cdot day^{-1}$), which is located closest to DOSTEL, is in very good agreement with the total absorbed dose measured with DOSTEL (115 $\mu Gy \cdot day^{-1}$ + 45 $\mu Gy \cdot day^{-1}$ = 160 $\mu Gy \cdot day^{-1}$).

The passive detectors of MTR which were located close to the DOSTEL have measured an absorbed dose rate of 189 $\mu Gy \cdot day^{-1}$ (*Berger et al.*, 2013). This value is slightly higher than the one measured with DOSTEL. The differences result from temporal changes of the radiation field. The DOSTEL measurements were taken between April and June 2008 and the passive detectors measured from October 2007 to November 2008. The altitude of the ISS has been increased at the end of June 2008. This led to a higher contribution from trapped particles, which was also observed by (*Lishnevskii et al.*, 2010). The absorbed dose from GCR particles increased further due to the solar cycle in 2008. This and small differences in the shielding of the passive detectors and DOSTEL can qualitatively explain the higher dose rate measured with the passive detectors.

5.4. Error Estimation

A statistical approach was used to estimate the uncertainty of the dose measurement. For the absorbed dose calculation formula 5.1 was used. The absorbed dose is calculated for every energy channel and the sum over all energy channels gives the total absorbed dose. To obtain a statistical error for this total absorbed dose Poisson distributed noise has to be applied on the number of counts in every energy channel. An example of this procedure is shown in figure 5.5. In black the number of counts are plotted over the energy loss of all energy channels for detector D4 measuring in telescope mode at April 13th 2004. In red and blue two examples of the same energy loss spectrum with added Poisson noise are shown. For higher energy deposits the number of counts decreases and the relative differences between the original spectrum and the noise added spectra increase. For energy bins with no counts the expected value of particles was estimated with a power law fit. The fit was applied to energy losses above 1 MeV and is shown as a black line in figure 5.5. Furthermore, the energy bins were distributed according

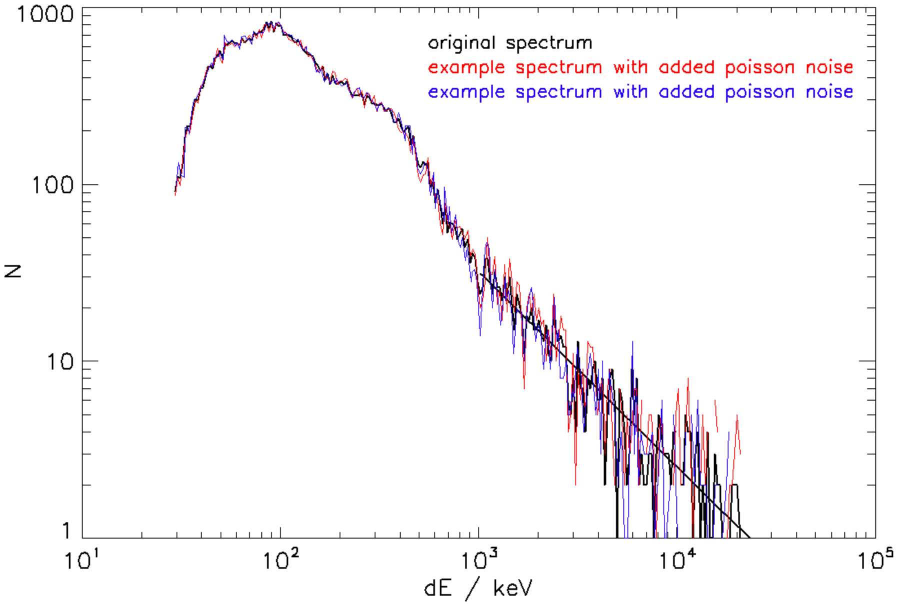

Figure 5.5.: This figure shows an energy deposition spectrum of April 13th of detector D4 recorded in single mode in black. The red and blue curves show two examples of the same spectrum with Poisson statistic noise added to every energy channel.

to a statistical approach. The energy bin $dE(ch)$ was converted to $\mathrm{dE}_{noise}(ch)$ by adding a uniformly distributed random number between -0.5 and 0.5 to the channel number and is described in formula 5.8.

$$
\begin{aligned}
dE_{noise}(ch) &= dE(ch + x) \\
x &\sim U([-0.5, 0.5])
\end{aligned}
\tag{5.8}
$$

The calculation shown in formula 5.1 was applied to Poisson noise added daily energy loss spectra in order to obtain the statistical error of the total absorbed dose per day. The result of this calculation for 100 noise added spectra is shown in figure 5.6. The absorbed dose values are shown in black. Their mean value is shown by the solid red line whereas the mean values ± the standard deviation are represented by the dashed red lines. The standard deviation in this case is $\approx 1.4\frac{\mu Gy}{day}$ which is $\approx$ 1.8 % of the mean value. The same investigation was done for two-daily energy loss spectra. The standard deviation of the 2-day averaged absorbed dose is $\approx 0.8\frac{\mu Gy}{day}$ ($\approx$ 1 %). The presented dose values in table 5.1 and 5.2 are mean values averaged over 53 days for MTR-1 and 31 days for MTR-2B. For such long time periods the statistical error is negligible. The method of using Poisson-noise-added energy loss spectra was also used to estimate the uncertainty of the quality factor Q. As an example the error estimation for the MTR-1 GCR mean quality factor will be presented. The MTR-1 GCR mean quality factor ($\langle Q \rangle = 3.16$, shown in table 5.1) was calculated from all energy deposition spectra containing GCR particles from April 13th to June 30th 2004. The sum of all of these energy spectra is shown in figure 5.7 in black. Two example of Poisson noise added to the original spectrum are shown in red and blue. Variations can only be seen in the highest energy bins. The quality factor Q was calculated for 100 noise-added spectra. The result can be seen in figure 5.8. The standard deviation of Q is 0.024 with a mean value of Q of 3.164. This is a variation of less than 1 % and can be neglected.

The quality factor strongly depends on the LET range an instrument covers. This can be seen in figure 5.2, where the ratio of integrated dose equivalent and absorbed dose increases with increasing LET. The quality factor calculation for the energy deposition spectrum shown in figure 5.7 without the highest energy bin leads to a mean quality factor of 2.95.

The calculated statistical errors are rather small and can be neglected for long

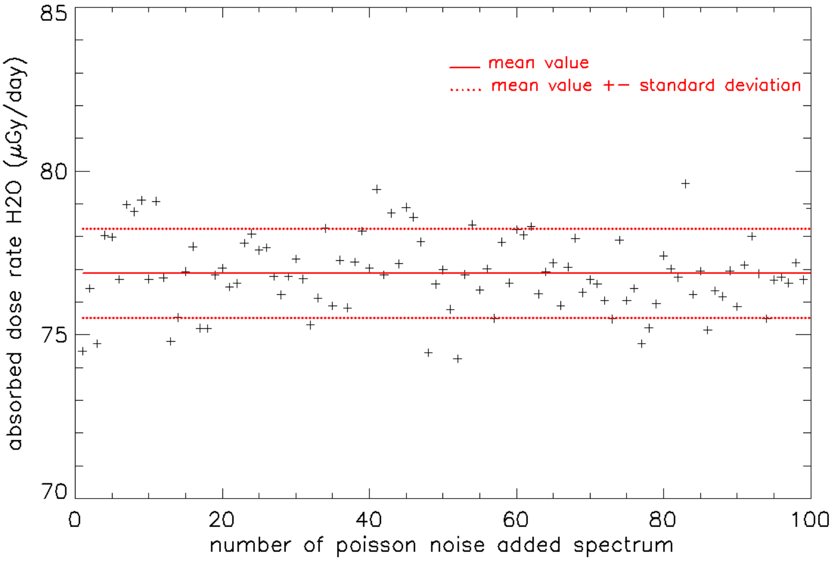

Figure 5.6.: Absorbed dose in water calculated for energy deposition spectra with added Poisson noise. The Y-axis shows the absorbed dose and the X-axis the number of the used spectrum. The solid red line shows the mean value of the absorbed dose, whereas the dotted red lines show the standard deviation.

time averaged data. The DOSTEL can measure the absorbed dose in silicon with high precision. Nevertheless, systematic errors were not considered in the calculations shown above. The dose values in chapter 5 were transferred from dose in silicon to dose in water by a constant conversion factor (see formula 5.2). This factor is also used to calculate the LET in water and thus the mean quality factor. The constant conversion factor used in this work (1.21) was calculated for protons and electrons (*Beaujean et al.*, 1999a). In literature different values of a mean factor for converting energy loss in silicon to energy loss in water can be found. A conversion factor of 1.193 (assuming only relativistic particles) was used in (*Doke et al.*, 2001) whereas 1.23 was calculated (for protons) in (*Pazmandi*, 2003). In both works the uncertainty for these values was estimated to be around 5 %. This uncertainty is assumed for this work, too. Because the absorbed dose, the LET, and the dose equivalent depend on the conversion factor , the 5 % uncertainty in the conversion of deposited energy in silicon to deposited energy in water results in an systematic uncertainty of 5 % for all dose values and mean quality factors presented in chapter 5.

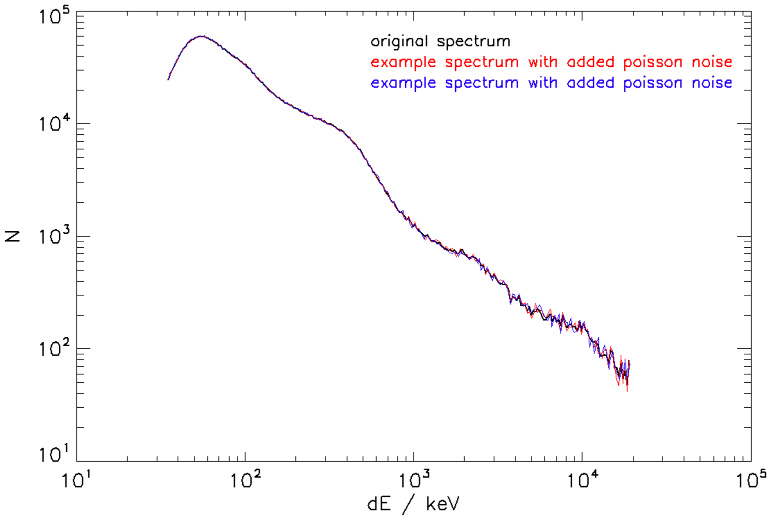

Figure 5.7.: This figure shows in black an energy deposition spectrum from April 13th to June 30th 2004 of detector D4 recorded in telescope mode. The red and blue curves show two examples of the same spectrum with Poisson statistic noise added to every channel.

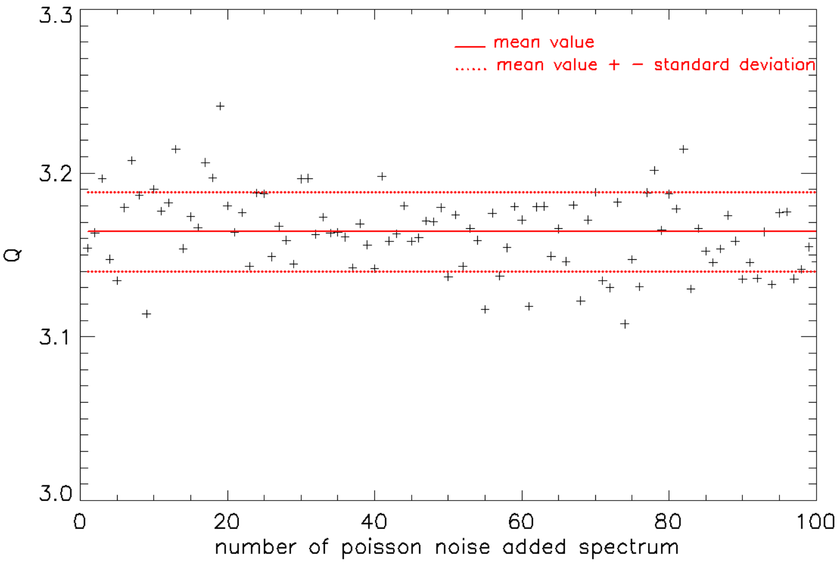

Figure 5.8.: Quality factor for noise added spectra. The energy deposition spectrum shown in figure 5.7 was used for the calculation of Q.

6. Comparison of Single- and Telescope Mode

As already mentioned in chapter 3.1, the DOSTEL operates in two different modes - single and telescope mode. In single mode all 4 detectors (PIPS detectors and PIN diodes) operate as single dosimeters, whereas in telescope mode the 2 PIPS detectors operate in coincidence mode as one telescope and the PIN diodes, like in single mode, as single dosimeters. The two DOSTEL modes allow a comparison of count rate and absorbed dose rate measured with 4 single detectors as well as a telescope detector in coincidence mode.

In this analysis the ratios of the count rates and the absorbed dose rates for the GCR component measured with the PIPS detectors in the two different modes between April 20th and June 30th 2004 are compared with the corresponding theoretical ratios obtained from the instrument geometry. For a first comparison the geometric factors calculated as described in *Sullivan* (1971) and *Sullivan* (1972) are used. For a deeper analysis a geometric Monte-Carlo model is used to simulate count- and absorbed dose rate ratios for different angular distributions of GCRs.

6.1. Ratio of the Single and Telescope Mode GCR Count Rates

The energy deposition spectra were used to obtain particle count rates for the DOSTEL detectors. To avoid geomagnetic differences between the different types of spectra, the energy deposition spectra of the four different detectors (2 PIPS detectors and 2 PIN diodes) and the two different modes (single / telescope) were summed up for the time period from April 20th to June 30th 2004. In this time period the radiation environment in LEO was stable (see chapter 5) and the DOSTEL data covers nearly the whole period.

Table 6.1.: Measured GCR count rate ratios for the different DOSTEL detectors.

Detector	$\frac{\text{count rate single mode}}{\text{count rate telescope mode}} \cdot \frac{sec}{sec}$	count rate ratio
D1 (lower PIPS)	$\frac{6.16}{2.89}$	2.13
D2 (PIN diode)	$\frac{1.59}{1.65}$	0.96
D3 (PIN diode)	$\frac{1.85}{1.84}$	1.01
D4 (upper PIPS)	$\frac{5.35}{2.80}$	1.91

The total number of particles in the energy deposition spectra was then divided by the total measurement time for the detectors and modes. For every detector we obtained two count rates, one for the single and one for the telescope mode. The count rates for the PIN diodes (D2, D3) should be identical for both DOSTEL modes, as they always act as a single dosimeter. The ratio of single mode and telescope count rates for the PIPS (D1, D4) detectors should represent the geometrical differences between a single and a telescope detector. The results for the different count rates and their ratios are shown in table 6.1. As expected the PIN diode count rates are close to identical for both modes, and thus, their ratios are close to 1 (within 5%). Unexpectedly, the count rate ratios for both PIPS detectors are not identical. For the upper (D4) and lower (D1) PIPS detector, the count rates in telescope mode are within 5% the same (2.89 and 2.80 counts per second), due to the coincidence condition. The discrepancy of 5% is resulting from different measurement times (alternating data collection). The count rates in single mode differ and are lower in detector D4 (5.35 counts per second) than in detector D1 (6.16 counts per second). This is due to the trigger used in the DOSTEL electronics. The sum pulse height of all four detectors after the Charge Sensitive Amplifier amplification is used as trigger. Due to the lower thickness of the upper PIPS detector D4 (this detector has only half the thickness compared to D1), the signals from this detector have only half of the height in comparison to the other DOSTEL detectors. The signal of Minimal Ionizing Particles (MIPs) which have a lower energy loss than the most probable energy loss of MIPs are not able to trigger the electronics if they only hit the upper PIPS detector D4. These particles can only be counted, if they hit both PIPS detectors. This results in identical count rates in telescope and single mode for energy losses below 0.18 $\frac{keV}{\mu m}$ for the upper PIPS detector D4 (see figure A.2 in appendix A).

The GCR particles, which are in the focus of this investigations, have energies high enough to penetrate both detectors. Due to this, the count rate ratio measured with the lower PIPS detector (D1) can be used for the following analysis. The measured count rate ratio for the lower DOSTEL PIPS detector is **2.13**.

6.1.1. Geometric Factor

The geometric factor G describes the area times the angular coverage of a particle detector and is given in $cm^2 \cdot sr$. This value is always calculated for isotropic particles incident from one hemisphere. For a planar detector the geometric factor is the area times the solid angle of one hemisphere (see formula 6.1). The geometric factors of the PIPS detectors can be calculated as described in (*Sullivan*, 1971). This results in a geometric factor for a single circular detector with an area A of 6.93 cm^2:

$$G_{single} = \pi \cdot A = 21.77 \ cm^2 \cdot sr \tag{6.1}$$

The geometric factor for the detectors in telescope mode with $R_1 = R_2 = 1.485$ cm and l = 1.5 cm is:

$$G_{telescope} = \frac{1}{2} \cdot \pi \cdot \left(R_1^2 + R_2^2 + l^2 - \sqrt{(R_1^2 + R_2^2 + l^2)^2 - 4 \cdot R_1^2 \cdot R_2^2} \right)$$

$$G_{telescope} = 8.24 \ cm^2 \cdot sr \tag{6.2}$$

The ratio of these geometric factors leads to the theoretical ratio of the count rates for a single and the count rates for a telescope detector.

$$R_{theoretical} = \frac{G_{single}}{G_{telescope}} = \frac{21.77 cm^2 \ \cdot sr}{8.24 cm^2 \ \cdot sr} = 2.64 \tag{6.3}$$

The theoretical ratio of **2.64** does not fit with the measured ratio of **2.13**. In the experiment data we observed a higher fraction of the incoming particles hits both detectors, and thus triggers the coincidence condition. An explanation for this could be a non-isotropic radiation field. If more particles are entering the instrument from above and less from the side, a higher fraction of the particles would trigger the coincidence condition and would lead to a smaller count rate ratio between single and telescope detectors. To investigate this anisotropy in more detail, a geometric Monte-Carlo model was set up. The principle of this model is described in (*Sullivan*, 1971).

6.1.2. Geometric Monte-Carlo Model

In this model particles are shot on the first detector. The trajectories of these particles are then tracked to see if the particles also hit the second detector and to calculate the theoretical count rate ratio between all particles and the particles hitting both detectors. A sketch of the used variables and the geometric tracking of the particles can bee seen in figure 6.1.

There are three particle variables used in the model. One variable describes the point of incidence on the first detector. Due to the cylindrical symmetry it is adequate to describe the point of incidence only by use of one variable r_1 describing the distance from the point of incidence to the center of the detector. Because the elemental area of a circle grows with the square of the radius, this higher probability of greater r_1 has to be taken into account, and thus, r_1 is distributed as follows:

$$r_1 = \sqrt{a} \cdot R \tag{6.4}$$

In this case R is radius of the DOSTEL PIPS detectors (1.485 cm). The variable **a** is a series of equally distributed random numbers between 0 and 1. By using the square root of **a** the higher probability for larger radii r_1 is taken into account. The direction of the particle is described by a zenith angle θ and an azimuth angle Φ. These two angles are calculated from two other series of equally distributed random number between 0 and 1, **b** and **c**. The three random number series (**a**,**b**,**c**) are independent of each other. The azimuth angle Φ is equally distributed between 0 and $2 \cdot \pi$.

$$\Phi = 2 \cdot \pi \cdot b \tag{6.5}$$

The zenith angle θ reaches from 0 (vertical to detector plane) to $\frac{\pi}{2}$ (horizontal to detector plane). To describe an isotropic particle incidence, the probability function of θ has to follow a $sin \cdot cos$ function. θ is distributed as follows for isotropic particle incidence:

$$P = \int \sin(\theta) \cdot \cos(\theta) \cdot d\theta = \frac{1}{2} \cdot \cos^2(\theta)$$

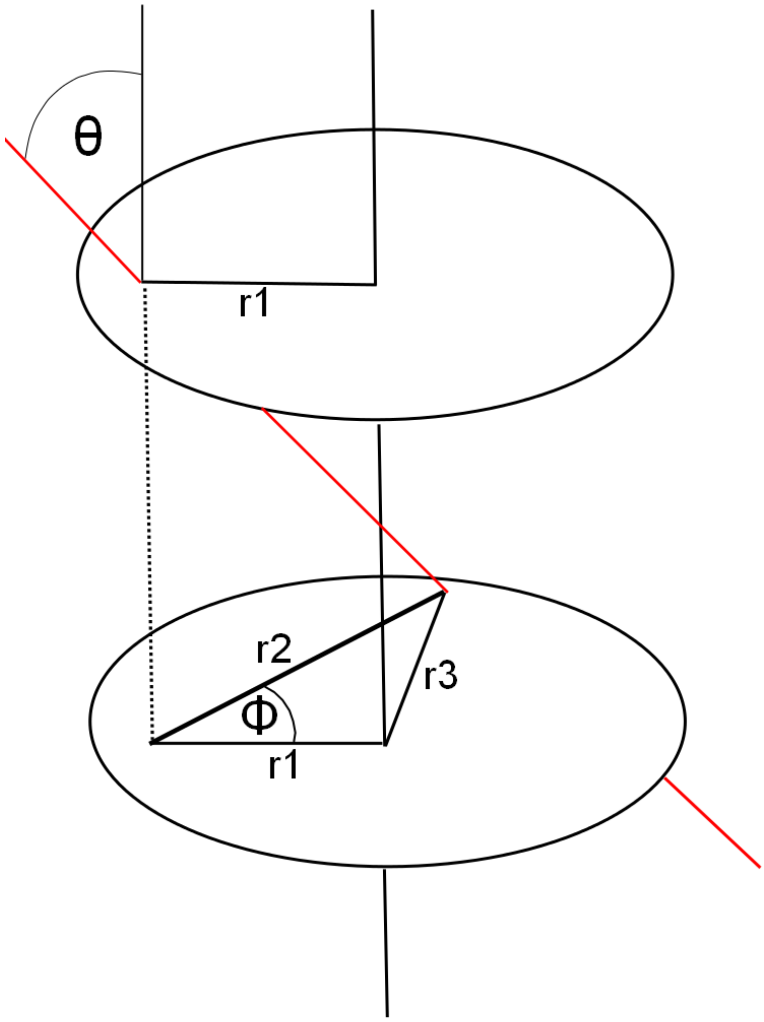

Figure 6.1.: Overview of the model setup. By use of three independent series of random numbers between 0 and 1, the radius on the first detector as well as two angles (θ and Φ) are simulated. The particle trajectory is then tracked to the second detector. If the particle also hits the second detector, the coincidence condition is true.

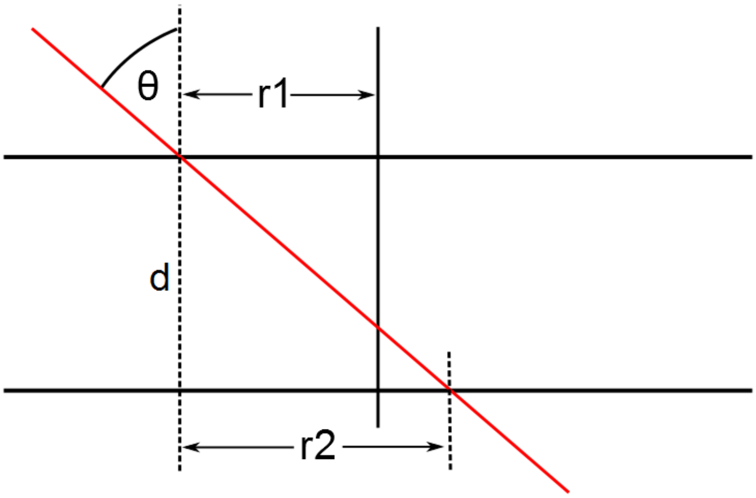

Figure 6.2.: Calculation of the projected distance between the incident points on the first and the second detector.

$$\theta \propto \arccos(\sqrt{P})$$

$$\theta = \arccos(\sqrt{c}) \tag{6.6}$$

For tracking the particle trajectory and getting the distance from the point of incidence on the second detector to its center (r_3) an interim value is needed. This interim value is the projected distance between the point of incidence on the first and on the second detector (r_2) and can be calculated by the product of the distance of the detectors (d) and the tangent of θ:

$$r_2 = \tan(\theta) \cdot d \tag{6.7}$$

The geometry which forms the basis of the r_2 calculation is visualized in the figure 6.2. The value of interest is the distance between the center of the second detector and the point where a particle hits this detector (r_3). This value tells us, if the particle hits both detectors, and thus fulfills the coincidence condition. The distance r_3 can be calculated by the law of cosine. The used angles and distances for this calculation are shown in figure 6.3.

$$r_3 = \sqrt{r_1^2 + r_2^2 - (2 \cdot r_1 \cdot r_2 \cdot cos(\Phi))} \tag{6.8}$$

When r_3 is less than the radius of the DOSTEL PIPS detectors (R = 1.485 cm),

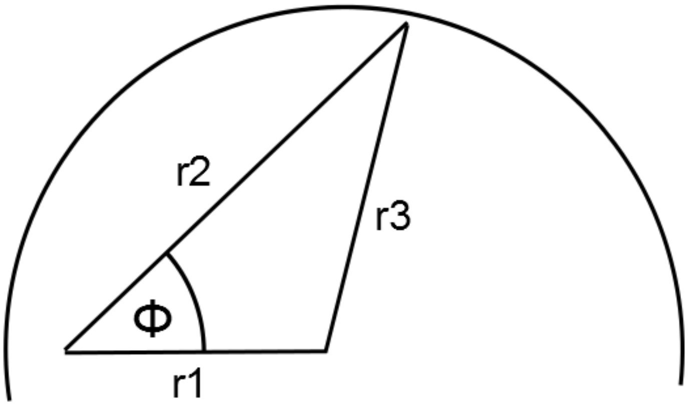

Figure 6.3.: Calculation of the distance between the incident point on and the center of the second detector (r_3).

this particle fulfills the coincidence condition and hits the second detector. The ratio between all particles and the particles hitting both detectors then gives the theoretical count rate ratio between a single mode and a telescope mode detector. To verify this model setup, the results for isotropic distributed particles are compared to the geometric factor ratio calculated above in chapter 6.1.1.

6.1.3. Model Verification

The Monte-Carlo model provides the ratio of particles detected on a single and a telescope detector. Furthermore, the incident angle (θ) distributions for a single and a telescope detector are provided by the simulation. These model results for an isotropic radiation field are shown in figure 6.4. The mean incident angle θ on a single detector is 45° and the θ angles are distributed according to a $\sin(\theta) \cdot \cos(\theta)$ function. This is the expected behavior for an isotropic field. The ratio of particles hitting the first detector (N_{single}) and both detectors in telescope mode (N_{tele}) is:

$$\frac{N_{single}}{N_{tele}} = \frac{100\%}{37.9\%} = 2.64 \tag{6.9}$$

The results agree very well with the theoretical count rate ratio calculated with the geometric factors. The model yields the expected results for the angular distribution and for the count rate ratios. Thus, this setup will also be used to calculate the responses for anisotropic particle distributions.

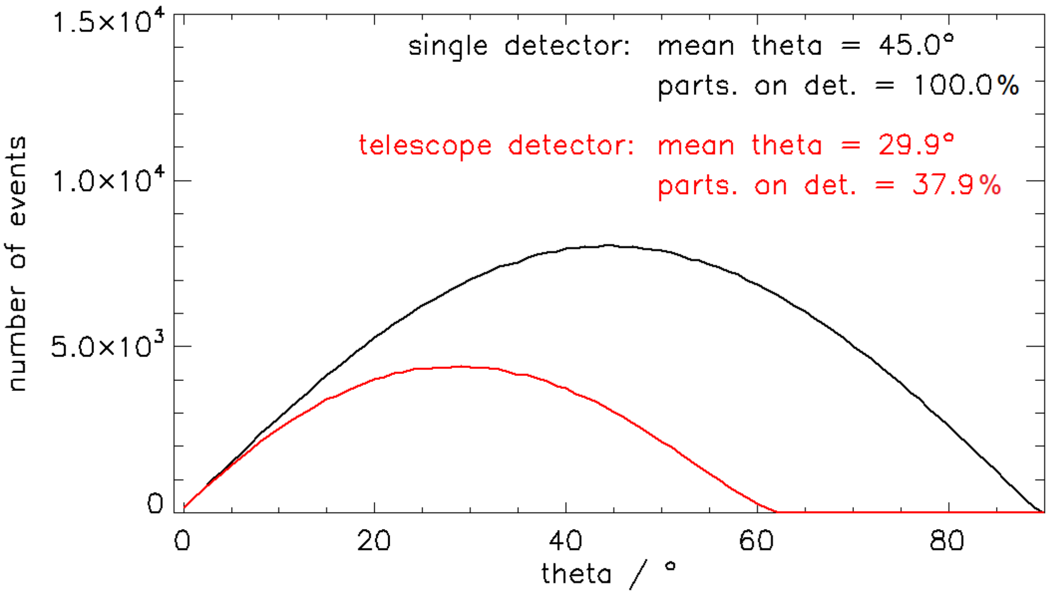

Figure 6.4.: θ distribution results for the DOSTEL PIPS detectors in single mode (black) and telescope mode (red) for isotropic particle incidence. The mean value of θ as well as the amount of particles which hit the detector in the two mentioned modes are given at the top right in the same colors.

6.1.4. Simulated Count Rate Ratios for Anisotropic Fields

To simulate anisotropic particle incidence the θ distribution has to be changed. Because the measured count rate ratio is smaller than the theoretical, the θ distribution has to be changed to a smaller θ cone, which means more particles are coming from above. This can be achieved by a distribution similar to the one for isotropic incidence, but with a higher power of the cosine. The first example (with c as a series of random numbers between 0 and 1) is:

$$P = \int \sin(\theta) \cdot \cos(\theta) \cdot \cos(\theta) \cdot d\theta = \frac{1}{3} \cdot \cos^3(\theta)$$

$$\theta \propto \arccos(\sqrt[3]{P})$$

$$\theta = \arccos(\sqrt[3]{c}) \tag{6.10}$$

This example can be generalized to any power of cosine:

$$P = \int \sin(\theta) \cdot \cos(\theta) \cdot \cos^n(\theta) \cdot d\theta = \frac{1}{n+2} \cdot \cos^{n+2}(\theta)$$

$$\theta \propto \arccos(\sqrt[n+2]{P})$$

$$\theta = \arccos(\sqrt[n+2]{c}) \tag{6.11}$$

In the following, $\cos^n$ will be used to name a $\sin(\theta) \cdot \cos(\theta) \cdot \cos^n(\theta)$ distribution. By using the described θ distributions it is assumed that the surface normal of the detector points in the direction of the zenith.

To find an explanation for the decreased measured count rate ratio, in comparison to the theoretical value, the model was used with different n (n=0.5, 1, 1.5, 2, 2.5). The results for the different θ distributions for a single PIPS detector are shown in figure 6.5. It can be seen, that the mean θ decreases for distributions with higher power of cosine. It should be pointed out, that the area under the different curves is not depending on the selected angular distribution. This is due to the model setup, where all particles hit the first detector. Figure 6.6 shows the model results for both PIPS detectors in telescope mode. Again, for a telescope detector the mean θ decreases for distributions with higher power of cosine. But this decrease is smaller than for a single detector. The area under the different curves increases with higher power of cosine. More particles hitting

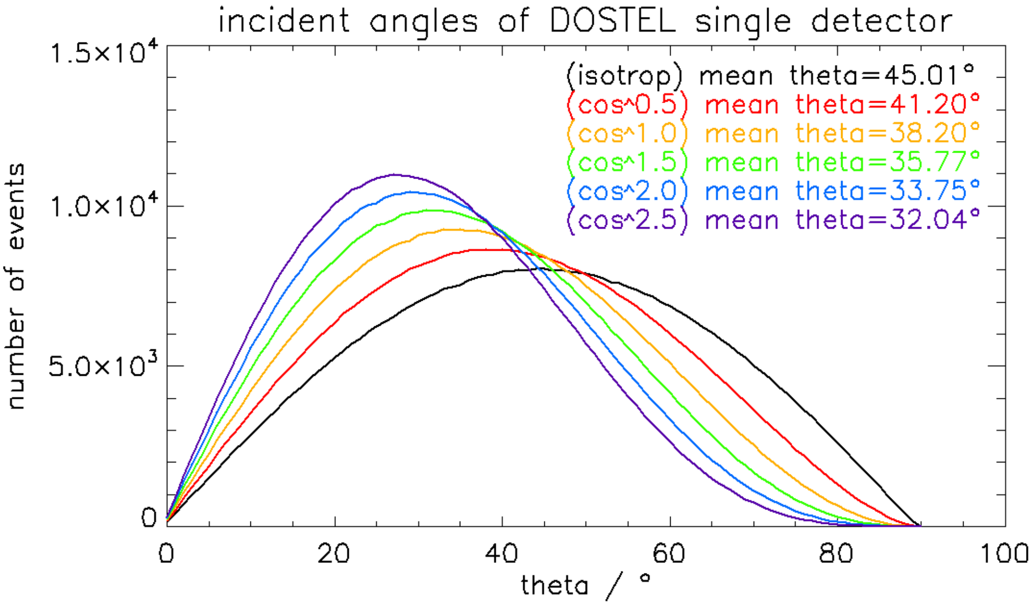

Figure 6.5.: Modeled θ distribution results for the DOSTEL PIPS detectors in single mode. For higher power of cosine, the distribution is shifted to lower incident angles. The mean θ angle for the different angular distributions are given in the same color as the graphs.

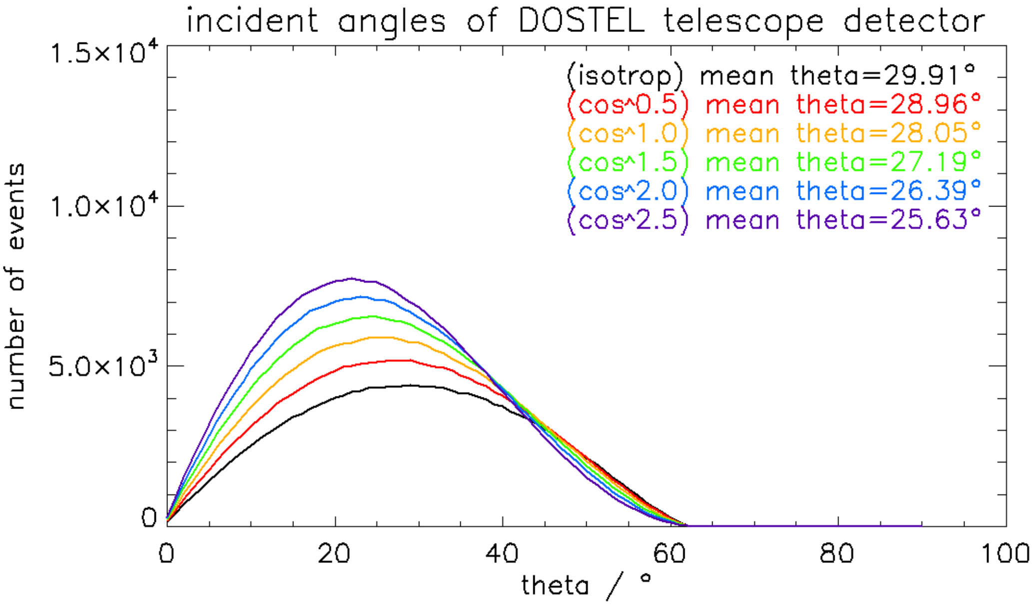

Figure 6.6.: Modeled θ distribution results for the DOSTEL PIPS detectors in telescope mode. For higher power of cosine, the distribution is shifted to lower incident angles and the area under the curves increases. The mean θ angle for the different angular distributions are given in the same color as the graphs.

Table 6.2.: Theoretical count rate ratios for different θ distributions.

θ distribution	$\frac{N_{single} \cdot \%}{N_{tele} \cdot \%}$	theo. count rate ratio
$isotrop$	$\frac{100}{37.9}$	2.64
$\cos^{0.5}$	$\frac{100}{43.4}$	2.30
$\cos^{1.0}$	$\frac{100}{48.0}$	2.08
$\cos^{1.5}$	$\frac{100}{51.8}$	1.93
$\cos^{2.0}$	$\frac{100}{55.0}$	1.82
$\cos^{2.5}$	$\frac{100}{57.7}$	1.73

the first detector also hit the second detector. For all different θ distributions the number of particles, which fulfill the coincidence condition, are counted. With these values the theoretical count rate ratio for the different distributions can be calculated like in formula 6.9. These theoretical count rate ratios of a single and a telescope detector are shown in table 6.2. The first column shows the name of the distribution and the second column the percentages of particles hitting a single and a telescope detector. The resulting theoretical count rate ratios for the different angular distributions are shown in the third column. The theoretical count rate ratio for a θ distribution following a $\sin(\theta) \cdot \cos(\theta) \cdot \cos^{1.0}(\theta)$ function is closest to the count rate ratio between a single and a telescope detector measured with DOSTEL.

6.2. Absorbed Dose Rate Differences

To get verified information about the angular distribution of the radiation field measured by MTR/DOSTEL during MTR-1 mission phase, a second measured quantity was used. There are two quantities directly measured by DOSTEL. The first one is the number of particles in a time interval - the count rate. The second one is the physical absorbed dose in silicon, which can be transferred to a dose rate by dividing it by the measured time of the interval. This absorbed dose rate

Table 6.3.: Measured absorbed dose rate (in silicon) ratios for the different DOSTEL detectors.

Detector Number	$\frac{\dot{D}_{single}}{\dot{D}_{tele}} \cdot \frac{\mu Gy \cdot day}{\mu Gy \cdot day}$	abs. dose rate ratio
Detector 1	$\frac{67.04}{28.86}$	2.32
Detector 2	$\frac{64.15}{65.80}$	0.97
Detector 3	$\frac{64.15}{63.37}$	1.01
Detector 4	$\frac{63.15}{26.83}$	2.35

in silicon can be used to compare measured results with the theoretical values obtained from the geometric Monte-Carlo model.

6.2.1. Measured Absorbed Dose Rate Ratio

In analogy to the calculation of the measured count rates (table 6.1), all GCR energy deposition spectra from April to July 2004 where used to calculated the measured absorbed dose rate to avoid geomagnetic differences between the different spectra types. The absorbed dose rate in silicon for the four detectors and the two different DOSTEL modes can be calculated from the energy deposition spectra measured with DOSTEL, as described in formula 5.1. The results of these calculations can be seen in table 6.3. The absorbed dose during single mode for the four detectors is comparable and varies within 5 % of its mean value. The values for the telescope mode differ obviously. The PIN diodes (D2,D3) measure the same absorbed dose as in single mode within the uncertainties. The values for the PIPS detectors (D4,D1) are lower for the telescope mode. This is due to the coincidence condition where only particles hitting both detectors are stored in the energy deposition spectra. As expected, the absorbed dose rate ratios are close to 1 for the PIN diodes. The ratios for the PIPS detectors are **2.32** and **2.35** for D1 and D4 and in good agreement. The lack of particles in detector D4 in single mode only leads to insignificant differences in the absorbed dose.

6.2.2. Simulated Absorbed Dose Rate Ratios for Anisotropic Fields

For this investigation the GCR component of the absorbed dose was analyzed. If one assumes that most of the particles contributing to the absorbed dose have high energies and can penetrate both detectors easily, this particles will have a nearly constant energy loss per distance. In this case the number of particles multiplied with the mean particle path length will be proportional to the absorbed dose. The model provides count rate ratios which were already used in the previous section. It also provides the angular distribution of the particles. The incident angle of a particle can be used to calculate its path length (l) in the detectors. Equation 6.12 shows this calculation. The resulting path length (l) is given in units of the detector thickness (d).

$$l = \frac{1}{cos(\theta)} \tag{6.12}$$

The mean path length $\langle l \rangle$ for different θ distributions can be calculated by building the mean value of the path length of all particles hitting the detector. The distribution of the path length for the different θ distributions for a single detector as well as their mean values can be seen in figure 6.7. The mean path length decreases significantly with higher power of the cosine used in the θ distribution. This strong decrease results from equation 6.12. If θ is 90° the path length of the particle is infinite. To avoid unrealistic long path lengths, only particles with incident angles below 87° were used to calculate $\langle l \rangle$ (this corresponds to $l \leq 20 \cdot d$). The mean path lengths for particles hitting both detectors are shown in figure 6.8. Only particles with incident angles below 62° can hit both detectors. This results in a maximum path length of 2.13 times the detector thickness. The angular restriction to 62° also leads to a less stronger decrease of the mean path length with higher power of cosine in the θ distribution. As mentioned above for particles which can easily penetrate both detectors the energy loss per distance is in good approximation constant. This means the count rate ratio multiplied with the path length ratio equals the absorbed dose rate ratio for these particles. The theoretical results of the absorbed dose rate ratios for the different θ distributions are shown in table 6.4. The first column shows the θ distribution and the second one shows the $\langle l \rangle$ ratio (in units of the detector thickness d) of particles hitting a single and a telescope detector multiplied with the theoretical count rate ratio of the detectors.

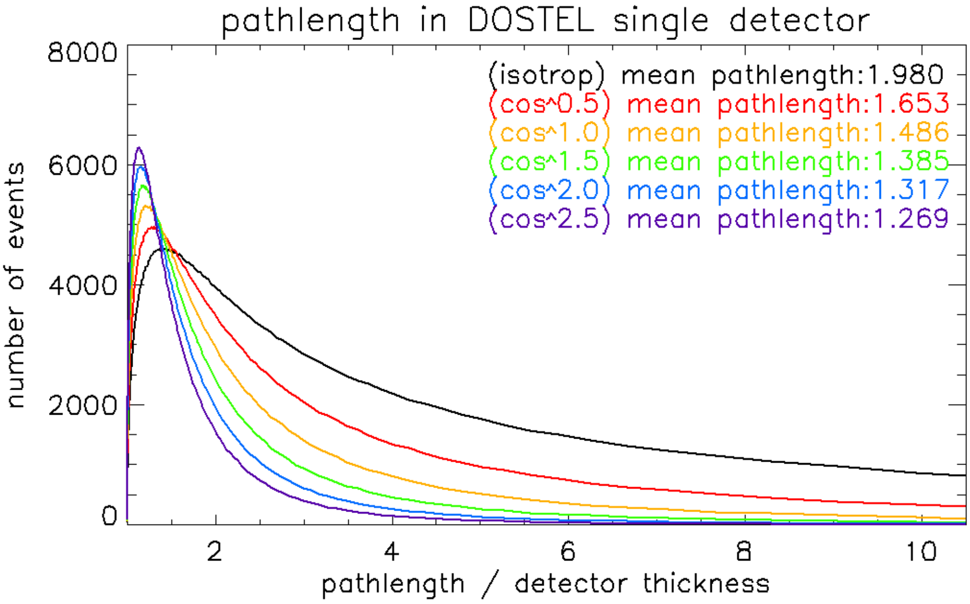

Figure 6.7.: Path length distribution for the DOSTEL PIPS detectors in single mode for different θ distributions. The mean path length divided by the detector thickness for the different angular distributions are given in the same color as the graphs.

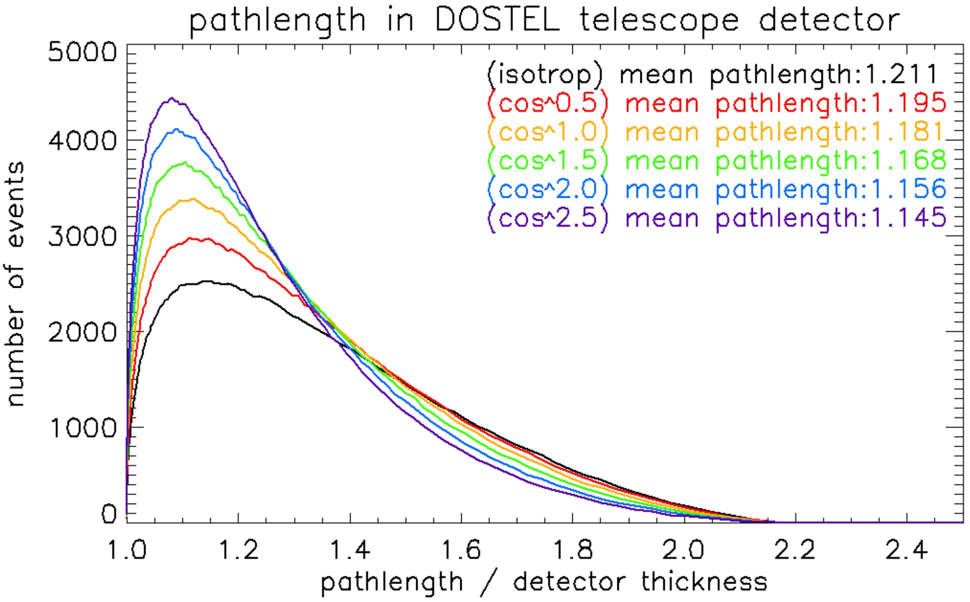

Figure 6.8.: Path length distribution for the DOSTEL PIPS detectors in telescope mode for different θ distributions. The mean path length divided by the detector thickness for the different angular distributions are given in the same color as the graphs.

Table 6.4.: Theoretical dose rate ratios for different θ distributions.

θ distribution	$\frac{\langle l\rangle_{single}}{\langle l\rangle_{tele}}\frac{d}{d} \cdot \frac{N_{single}}{N_{tele}}\frac{\%}{\%}$·theo. count rate ratio	theo. dose rate ratio
isotropic	$\frac{1.98 \cdot d}{1.21 \cdot d} \cdot 2.64$	4.32
$\cos^{0.5}$	$\frac{1.65}{1.20} \cdot 2.30$	3.17
$\cos^{1.0}$	$\frac{1.49}{1.18} \cdot 2.08$	2.63
$\cos^{1.5}$	$\frac{1.39}{1.17} \cdot 1.93$	2.29
$\cos^{2.0}$	$\frac{1.32}{1.16} \cdot 1.82$	2.09
$\cos^{2.5}$	$\frac{1.27}{1.15} \cdot 1.73$	1.91

The resulting theoretical dose rate ratios for the different angular distributions are shown in the third column. This ratio decreases for higher power of cosine in the θ distribution function. The theoretical ratio for a $cos^{1.5}$ distribution (**2.29**) is closest to the measured absorbed dose rate ratio of **2.32**. An isotropic incidence of GCR particles can not explain the count and dose rate ratios between a single and a telescope detector measured with DOSTEL. By using a $\sin(\theta) \cdot \cos(\theta) \cdot \cos^n(\theta)$ distribution with $1 \leq n \leq 1.5$ it is possible to reproduce the DOSTEL measurements. This result is an estimation of the angular GCR distribution. The azimuth angle was not changed during this analysis and the assumption that the detector surface normals are pointing toward zenith was made. In addition the theoretical absorbed dose rate ratio is based on the assumption of constant energy loss per distance for GCR particles.

To calculate an theoretical result for the anisotropy of GCR particles in LEO it would be necessary to calculate an azimuth and zenith angle depending cutoff rigidity (see chapter 2.2). With this cutoff rigidity it would be possible to calculate an angular depending theoretical count rate and to obtain the theoretical angular distribution of GCR particles.

The LET used in this work was calculated for an isotropic field in chapter 5. The discovered anisotropy leads to minor changes in the mean particle incident angle, and thus to minor changes in the mean path length and the LET. Nevertheless the effect on the LET is less than 2 % and can be neglected.

The LET is used for the calculation of the mean quality factor, where only energy losses above 10 $\frac{keV}{\mu m}$ are affected. The energy resolution in this range is worse than 3 % and thus the uncertainty in the energy is higher than the LET change due to the anisotropic field.

6.3. Distribution of SAA protons

Like for the GCR component above, the count rate ratios for the four DOSTEL detectors during SAA crossings were calculated for May 2004 (see table 6.5). It can be seen that the count rates of the PIN diodes (D2, D3) in single mode and telescope mode differ. Because they always measure as a single dose meter without any coincidence conditions, their count rates should be identical in both modes. For both diodes the count rates in single mode are higher (53.1, 54.8) than in telescope mode (44.5, 49.5). These count rate differences result from orbital differences during the SAA crossings. The mean geographical position for SAA transits differs between single and telescope mode. Even if, the data of all SAA crossings during May 2004 are used, the differences in the count rates in the two modes are significant. Du to this, a comparison of the single mode and telescope mode for the PIPS detectors (D1, D4) is meaningless.

Table 6.5.: Measured SAA count rate ratios between single mode and telescope mode for the four DOSTEL detectors. All transits though the SAA region during May 2004 were used.

Detector	$\frac{\text{count rate single mode}}{\text{count rate telescope mode}} \cdot \frac{sec}{sec}$	count rate ratio
D1 (lower PIPS)	$\frac{127.2}{62.7}$	2.03
D2 (PIN diode)	$\frac{44.5}{53.1}$	0.84
D3 (PIN diode)	$\frac{49.5}{54.8}$	0.90
D4 (upper PIPS)	$\frac{142.7}{62.2}$	2.30

6.3.1. Case study for SAA transits

As shown above, an analysis of the mean detector count rates in single and telescope mode is not sufficient. Therefore, each SAA transit in single mode is analyzed separately in this section. Only single mode transits were chosen to enable a direct comparison of the four DOSTEL detectors. To see, if there are different behaviors of the transits the total number of counts per cm^2 are plotted against the absorbed dose during each transit in figure 6.9. The black line shows the mean number of counts per dose. The SAA transits with absorbed dose less than 30 μGy were not further analyzed. For absorbed dose above 30 μGy, the red box separates cases where at least one detector shows a higher number of count needed to obtain a certain absorbed dose. A high number of counts per dose means that the particles have shorter path length in the detector, and thus,

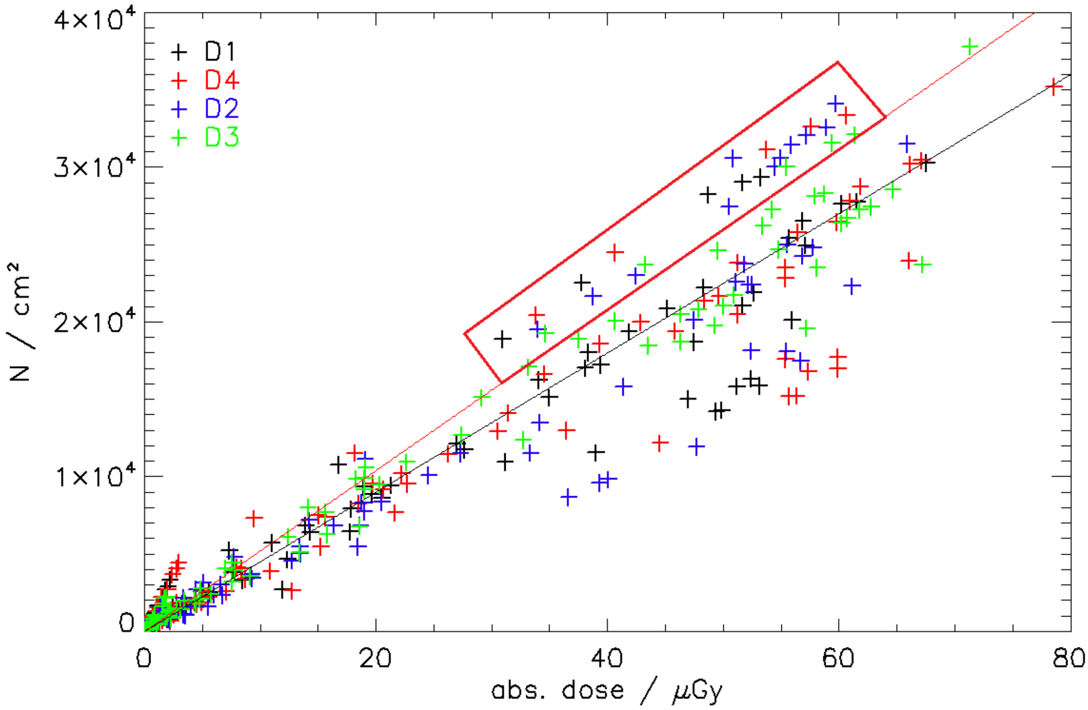

Figure 6.9.: Number of particles per cm^2 versus absorbed dose in μGy for single mode SAA crossings in May 2004. The results of the four DOSTEL detectors are shown in the color code shown in the upper left. The black and red lines show a constant number of counts per dose ($N(black) = \frac{D}{\mu Gy} \cdot 450 \mu Gy$, $N(red) = \frac{D}{\mu Gy} \cdot 520 \mu Gy$). The red box shows a population of SAA crossings with an absorbed dose above 30 μGy and count rates above the red line.

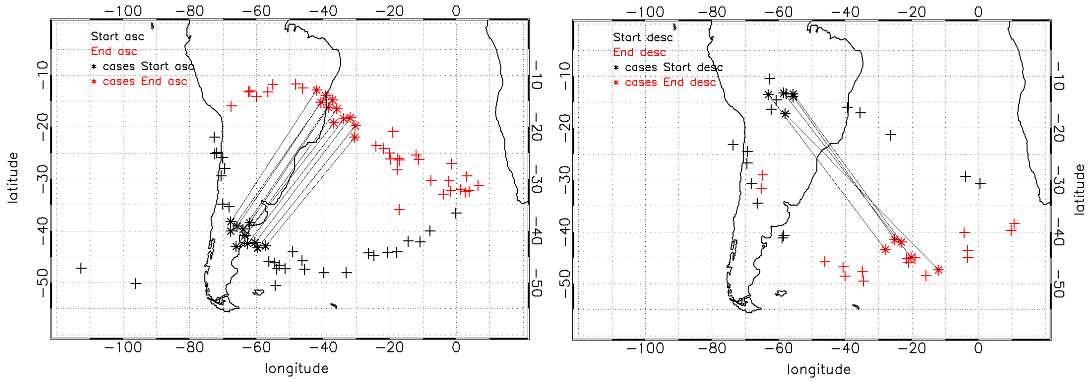

Figure 6.10.: Orbits of single mode SAA crossing in May 2004. The black crosses show the start position and the red crosses the end position of the SAA crossings for ascending transits in the left panel and descending transits in the right panel. The SAA crossings inside the red box from figure 6.9 are marked with asterisks and are connected with a black line.

a more vertical incidence on the detector. The SAA transits with counts per dose in the red box are further analyzed and in following called selected transits. The orbits of the selected transits are shown in figure 6.10. The left panel shows all single mode ascending SAA transits during May 2004. The black crosses mark the position of the start of data collection and the red crosses the end of data collection. The selected transits are marked with asterisks and are connected with black lines. These lines don not represent the exact ISS position during the SAA transit. Nevertheless, it can be seen that all ascending transits close to the center of the SAA region are selected transits. The same illustration can be seen in the right panel for descending crossings of the SAA region. The selected descending transits cross the center of the SAA region as well, but not all crossings of the center are selected transits.

The ISS coordinate system is defined like shown in figure 6.11. The x-axis shows towards the direction of movement and the z-axis is pointing to nadir (center of the Earth). The y-axis then points to the starboard side. Figure 6.11 shows the standard attitude of the ISS. The front of the ISS shows in x direction and the bottom in the z direction. Comparably to aircraft, the ISS attitude in respect to the shown ISS coordinate system is given by three angles – roll, pitch and yaw. The roll describes the rotation around the x-axis, the pitch the rotation around the y-axis and the yaw the rotation around the z-axis.

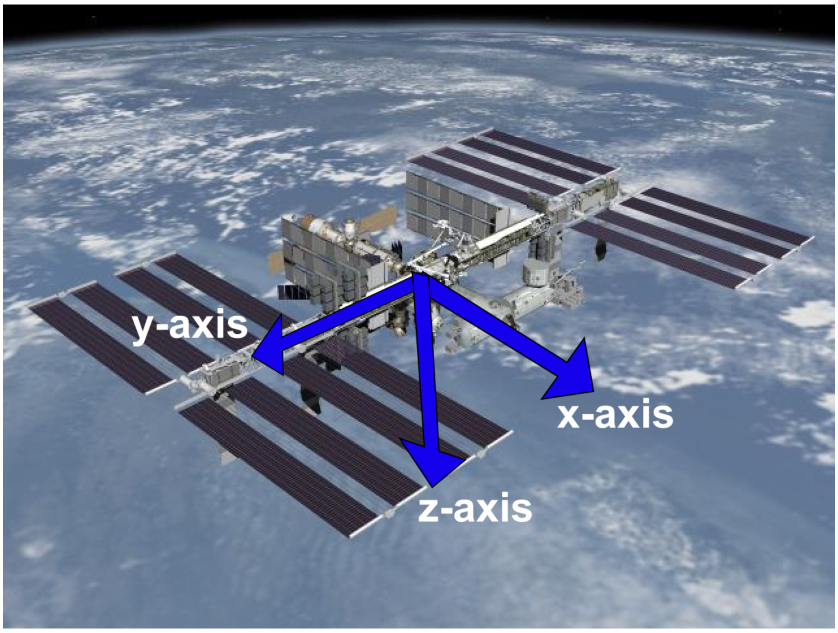

Figure 6.11.: Body coordinate system of the ISS. Shown is the standard configuration of the ISS attitude. ISS picture courtesy of NASA.

The standard ISS attitude (as shown in figure 6.11), thus is defined by roll pitch and yaw values close to zero.

The 16 selected SAA transits can be categorized in two cases of ISS attitude. In the first case, the attitude of the ISS was in standard configuration (roll, pitch and yaw are close to zero). Five of the selected transits show this configuration. In the second case, the ISS was turned 90° around the x-axis (roll $= 90°$). The pitch and yaw were still close to zero during this configuration. The remaining three selected transits are characterized by yaw values between 180° and 360° and are not further analyzed. The dose per count for the 13 selected transits from case one and two is shown in figure 6.12 in the upper panel. The four DOSTEL detectors are shown in the color code given in the upper left. The case two transits are marked with a red box (transit three to ten). The black line indicates if the transit is ascending or descending. The black line is low for ascending crossings and high for descending crossings of the SAA region. It can be seen that for case one (outside the red box) the roll pitch and yaw of the ISS are close to zero. The dose per count in this case is high for detector D2 which is one of the PIN diodes. The other three detectors show lower dose per count values and are comparable to each other. This means the particle path length is larger for detector D2 than

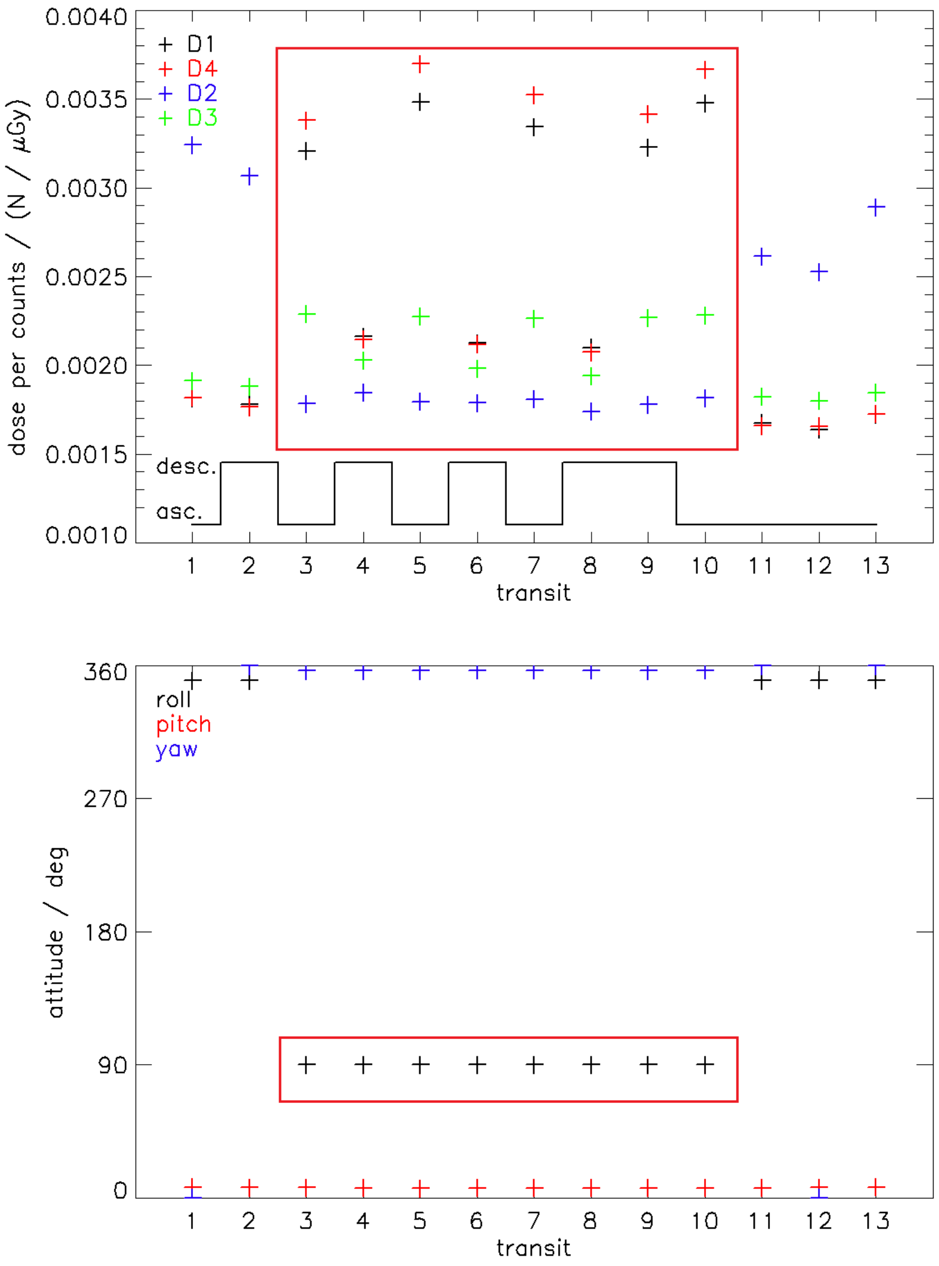

Figure 6.12.: Dose per count and ISS attitude for selected SAA transits in May 2004. The upper panel shows the dose per count for the four DOSTEL detectors in color code (upper left side). The black line is high for descending and low for ascending transits through the SAA region. The lower panel shows the corresponding ISS attitude (roll, pitch and yaw) in values from zero to 360°. The red boxes in both panels mark the cases where the ISS roll is close to 90°.

for the others. The inner radiation belt particles in ISS altitudes are close to their mirror point, and thus, the particles direction is highly anisotropic and the particles are entering the detectors from a plane perpendicular to the geomagnetic field lines (see figure 2.6). In an over simplified model the surface normals of the telescope detectors (D1 and D4) and the PIN diode D3 span a plane which is approximately the plane of particle incidence. The incoming particle have lower path length in these detectors. The PIN diode D2 is perpendicular to D3 and the telescope detectors, and thus, D2 is parallel to the particle incidence plane and the particles have longer path length in this detector.

During SAA transits with ISS roll angles close to 90° (marked with the red box in figure 6.12), the detectors which are now 90° rotated show a different behavior. In this case the dose per count is lowest for the PIN detector D2, which is in good agreement with simple model explained above. In case one D2 is parallel to the plane of particle incidence. This results in high particle path length and high dose per count values in D2. After the 90° rotation, D2 is perpendicular to the plane of particle incidence and the particles have a smaller path length in the detector resulting in a lower dose per count value.

The simple explanation that the detectors D1, D4 and D3 are perpendicular and detector D2 parallel to the plane of particle incidence in case one (roll, pitch and yaw close to zero) can not describe the behavior of the detectors D1, D4 and D3 after the 90° rotation (case two). Especially for ascending transits the dose per count values are not inverted compared to case one. The dose per count in D2 is lowest but the dose per count values in the other detectors are only slightly increased (compared to the D2 values in case one). For descending crossings which can be approximated by a -90° rotation around the z-axis (yaw=270°), the dose per count values for the telescope detectors (D1 and D4) are comparable to the D2 dose per count values from case one. This means the mean path length in the telescope detectors during descending crossings in case two conditions is comparable with the mean path length in D2 during ascending crossings in case one conditions. A 90° rotation around the x-axis and the z-axis brings the telescope detectors in a position, related to the particle incidence plane, which is comparable to the position of detector D2 before the rotation. This is not in agreement with the simplified model.

The dose per count values for detector D3 are much less influenced by rotations of the ISS than the other detectors. In the simple model explained above, this detector should not be influenced by a rotation around the x-axis if its surface normal is pointing in the direction of the x-axis. That this is true can be seen in the comparison of ascending SAA crossings for the two cases. But the 90° rotation around the z-axis from ascending to descending crossings in case two conditions should lead to long particle path length and high dose per count values in D3 (comparable to the values for D2 in case one). Figure 6.12 shows that this is not the case.

To explain the behavior of the dose per count of all detectors in dependence of the ISS attitude a more realistic model would be necessary. It is known that the incidence directions of SAA protons lie in a plane perpendicular to the magnetic field. Due to the East-West effect more particles are coming from western direction. SAA protons are effectively shielded by the ISS. This means protons can not reach the DOSTEL detectors if they would have to cross the ISS before. By using these information and the DOSTEL detectors orientation in respect to the ISS body coordinate system (figure 6.11) it would be possible to build a geometric model to analyze if the DOSTEL measurements can be explained by the established SAA particle distribution. From photographs of the MATROSHKA experiment outside ISS it can be estimated that the surface normals of the telescope detectors are pointing approximately towards nadir (∼20° tilt). Unfortunately, the data of the exact orientation of the detectors was not available to me. A deeper analysis of the direction of particle incidence was therefore not conducted in the frame of this thesis but was kept for possible future work.

7. Radiation Belt in the Slot Region

In this chapter the MTR - DOSTEL data obtained from September to October 2004 will be discussed. At the end of June 2004 a communication problem between the DOSTEL and the MTR data processing unit occurred, which led to incorrect storage and thus to the loss of most data packages from July and August 2004. Due to the problem that the MTR data processing unit did not start new files for new DOSTEL data packages, big DOSTEL data files containing multiple 6-hour data packages had been produced. For these data files only the download time of the last data package is available. It was possible to recover some of the DOSTEL data by separating the files in the 6-hour data packages and applying multiple times -6 hour time offsets to the data packages, starting with the last. These data sets were time corrected as described in chapter 4. The time corrected count rates were then used for further investigations. One of the restored data files contains 60 data packages covering the time between September 24th and October 8th 2004. The other restored data files are smaller and cover the time between July 19th and July 22nd 2004. The July data show no qualitative differences to the data obtained from April to June 2004 (see figure 4.4). The count rates for July 20th are shown as an example in figure 7.1. The dependence on the geomagnetic cutoff rigidity can be seen in the 45 minutes modulation of the data. This 45 minutes correspond to one half orbit of the ISS (e.g., maximum at highest latitude north, minimum at the equator, maximum at highest latitude south). The spikes with count rates up to 1000 counts per second result from crossings of the inner radiation belt in the region of the SAA. The modulation of the GCR component by Earth's magnetic field as well as the crossings of the inner radiation belt in the region of the SAA can clearly be seen. The radiation field at ISS altitudes has not changed between April 13th and July 22nd, as demonstrated by the data visualized in figure 4.4 and figure 7.1.

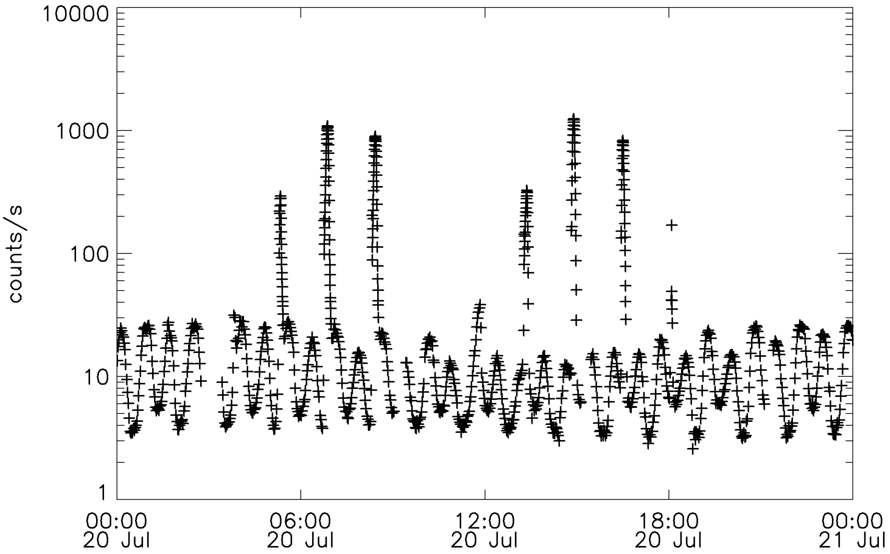

Figure 7.1.: Time profile of count rates measured by DOSTEL at July 20th 2004. The dependence on the geomagnetic cutoff rigidity can be seen in the 45 minutes modulation of the data. The spikes in the count rate result from crossings of the inner radiation belt in the region of the SAA.

7.1. DOSTEL Data of September and October 2004

For the time period after July 22nd, data are available from September 24th to October 8th. One example time profile of the DOSTEL count rates of this time period is shown in figure 7.2. A comparison with count rates from May and July 2004 (see figure 4.4 and 7.1) show the same modulation of the GCR component by Earth's magnetic field and the same increased count rates (up to 1000 counts per second) due to crossings of the inner radiation belt in the region of the SAA. The differences in the September and October data are additional count rate peaks with maximum count rates up to 6000 counts per second. These spikes can be seen shortly after the increased count rates belonging to inner radiation belt crossings. In figure 7.2 two of these additional spikes can be seen after the inner belt crossings at 1 am and 2:30 am. To identify the locations of increased count rates, the geographic distribution of the DOSTEL count rates can be used. This is depicted in figure 7.3. It can be seen that the additional spikes with more than 6000 particles per second are loacted in a bordered region south of South Africa.

The high count rates as well as the localized structure of the additional count

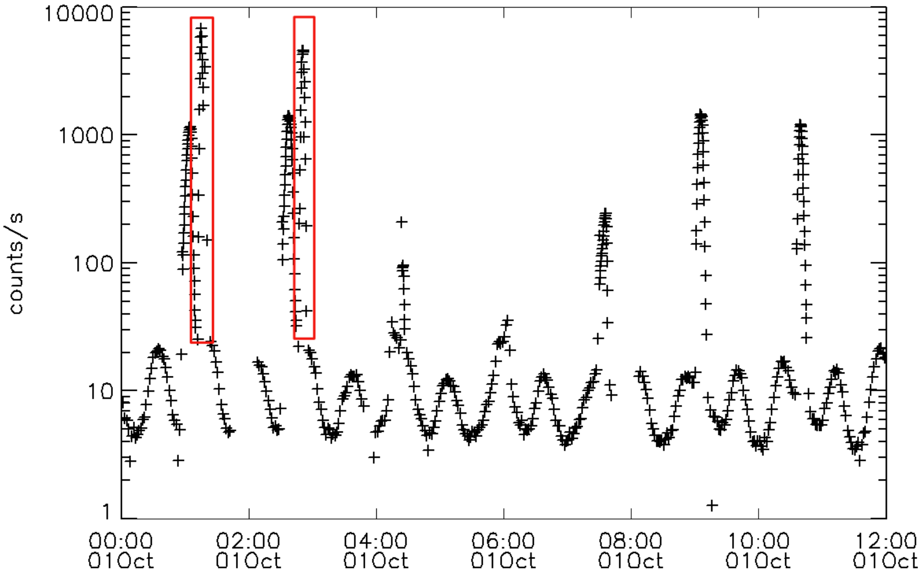

Figure 7.2.: Time profile of count rates measured by DOSTEL during October 1st 2004. Directly after the increased count rate due to inner radiation belt crossing at 1 am and 2:30 am two additional spikes with count rates up to 6000 particles per second can be seen (marked with the red boxes).

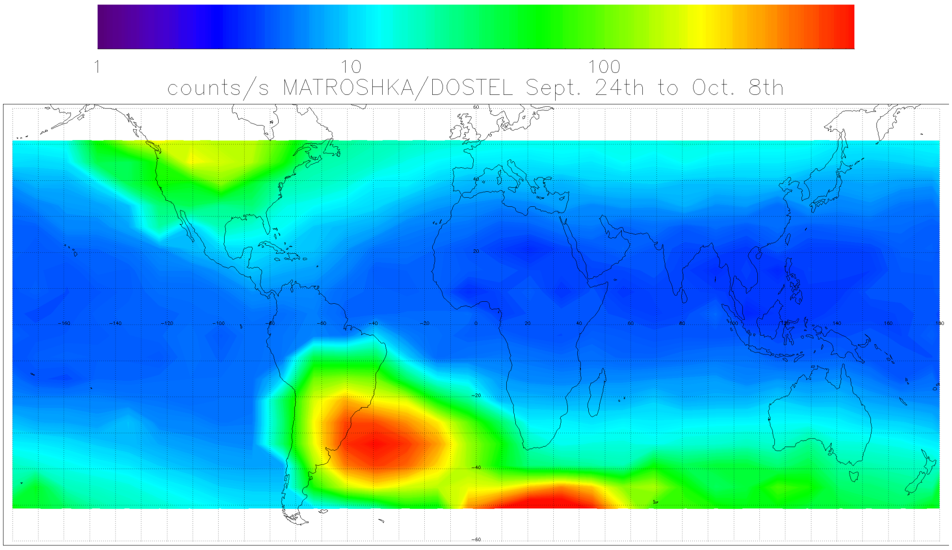

Figure 7.3.: Geographical count rate distribution for September and October 2004 during the MTR-1 mission phase. Beside the crossing of the inner radiation belt in the SAA region an additional region with enhanced count rate can be seen south of South Africa.

rate enhancement south of South Africa indicate that these trapped particles belong to a narrow L-parameter interval. To verify the L-parameter of the enhanced count rate region south of South Africa the count rate dependence on the L-parameter for the DOSTEL data of September and October is shown in figure 7.4. For this plot the same method was used as for count rate L-value dependence for the May data (figure 4.11). The GCR component (black) shows no differences in comparison to the May 2004 data. The trapped particles (in red) show one population with L-values between 1.2 and 2.0. These are particles of the inner radiation belt. The distribution of this particle population is comparable with the inner belt particle population measured in May 2004. The particles producing the additional count rate enhancement are connected to magnetic field lines with L-values between 2.5 and 3.5. This L-parameter interval forms the so called Slot region (chapter 2.3) which shows a low particle flux at normal conditions. The increased count rates at L-values greater 3.5 result from crossings of the edges of the outer radiation belt. The particle flux in the outer radiation belt is not very stable and can differ due to solar activity (chapter 2.3). The count rates observed during these outer belt crossings in September and October 2004 are higher than the ones observed in May 2004.

Changes in the radiation belt structure after solar events are known. One prominent example of such variations was observed during the Halloween storm in 2003 (*Baker et al.*, 2004). During this storm the position of the outer radiation belt shifted towards Earth and the Slot region was filled with relativistic electrons. It was first shown by *Shurshakov et al.* (1996), that such a new formed radiation belt in the Slot region can extend down to LEO. In that work the data obtained with a Silicon semiconductor dosimeter mounted outside the MIR station showed transits through a radiation belt in the Slot region. Unfortunately no other radiation detector was mounted outside the ISS in autumn 2004, and thus, observations of instruments on other space craft obtained during the time between July and November 2004 are shown in the next section to verify the DOSTEL data obtained during September and October 2004.

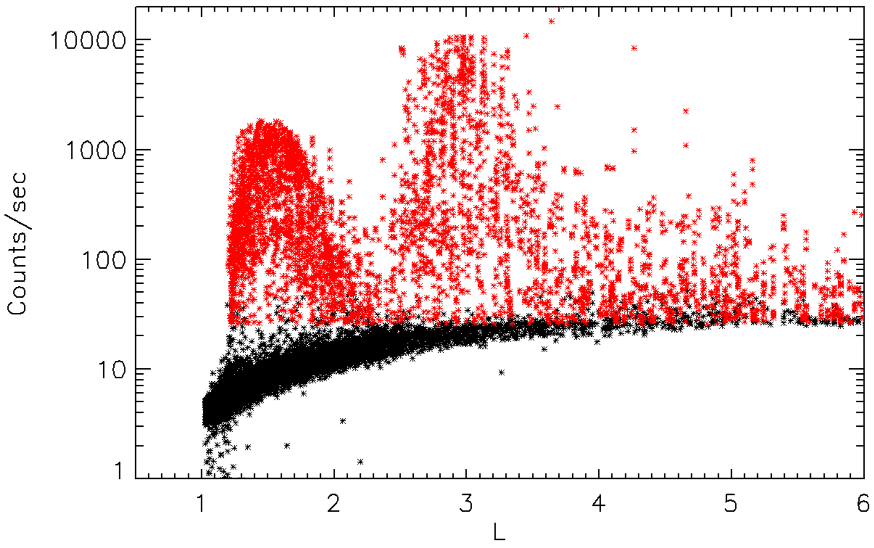

Figure 7.4.: MTR-DOSTEL count rate over the McIlwain L-parameter for September and October 2004 during the MTR-1 mission phase. The GCR component is shown in black. The trapped particle component is shown in red. The increased count rates from the region south of South Africa belong to L-values around L=3, the so called Slot region.

7.2. Observations of Other Instruments

Radiation belt observations are also performed by instruments especially designed for this purpose. During the second half of year 2004, when the MTR-DOSTEL observed the additional radiation belt in the Slot region, other experiments for radiation belt observations were in space, too. One of them was the Solar Anomalous and Magnetospheric Particle Explorer (SAMPEX) (*Baker et al.*, 1993). SAMPEX had a polar orbit around Earth and was able to measure charged particles at different L-parameters. A time profile of L-parameter spectra of electrons with energies between 3.5 MeV and 16 MeV is shown in figure 7.5. The region between L = 2 and 3 shows a low particle intensity until DOY 209 (July 27th, 2004). After that, a strong increase of relativistic electrons at L-parameters between 2.5 and 4 was observed. The intensity of these particles decayed in time but was observable until DOY 310. The DOSTEL data from 19th to 22nd of July show no differences to the data of May 2004, which is in good agreement with the electron flux measured by SAMPEX. Unfortunately, there are no DOSTEL data available between July 22nd (DOY 209) and September 24th (DOY 269), but the

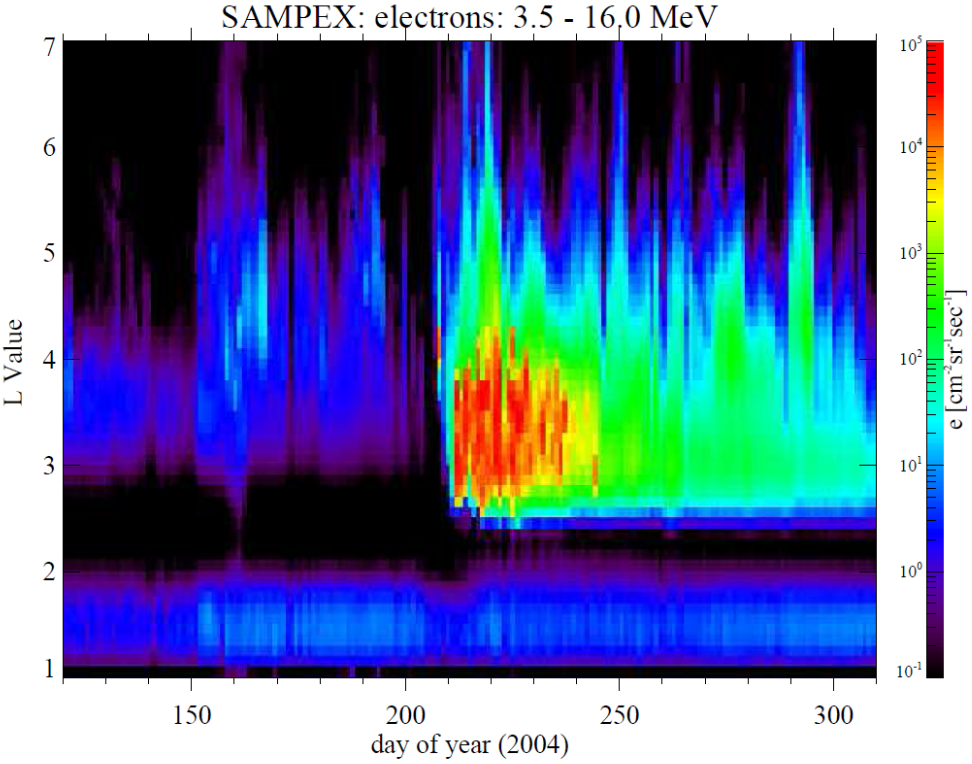

Figure 7.5.: SAMPEX measurements of 3.5 to 16.0 MeV electrons. This figure shows the flux of electrons in color code (right axis) over time (x-axis) and the McIlwain L-parameter (y-axis) for the year 2004. It can be seen that at DOY 209 the region between L=2.5 and L=4 was filled with relativistic electrons. The electron flux decreases in time but is observable until DOY 310. The picture was taken from http://lasp.colorado.edu:8080/sampex_jsp/elo-lsort.jsp in July 2010.

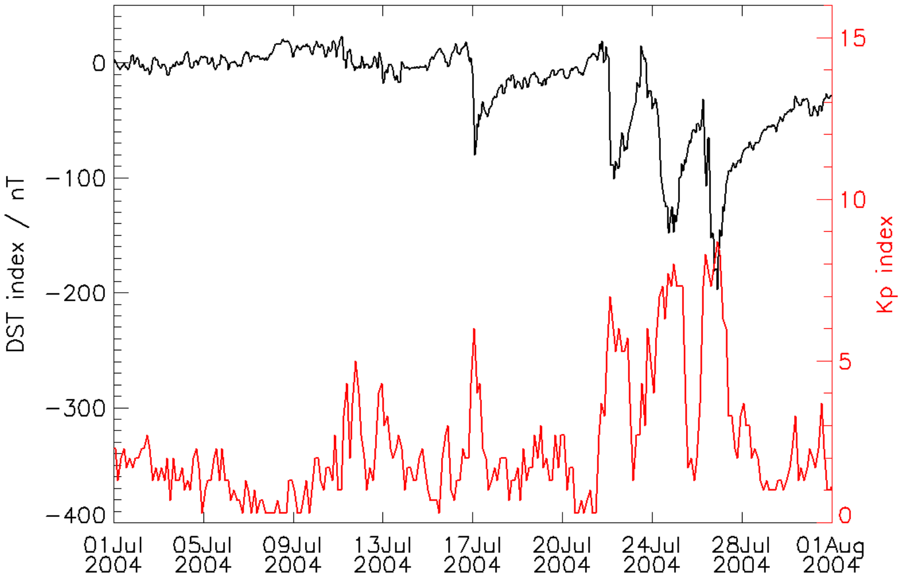

Figure 7.6.: DST index (black) and Kp index (red) of July 2004. The decreased DST and increased Kp index between July 23 and July 27 show the three geomagnetic storms correlated with the filling of the slot region with electrons on July 27th. The indices were taken from the NOAA homepage on April 3rd 2014 (ftp://ftp.ngdc.noaa.gov/STP/GEOMAGNETIC_DATA/INDICES/).

data from September 24 to October 8 show the additional radiation belt in the slot region (like shown in the previous section). The SAMPEX data has shown that this additional radiation belt in the slot region observed by MTR-DOSTEL results from a filling of Earth's magnetosphere with relativistic electrons at July 27th. At this time the last of three geomagnetic storms took place (see figure 7.6). The three storms were driven by interplanetary CMEs and showed DST indices of -101, -148 and -197 nT (*Zhang et al.*, 2007). The last of these three storms is characterized by high solar wind speeds combined with a southward interplanetary magnetic field component (*Kuznetsov et al.*, 2009). The electron filling of the slot region was also observed by the Japanese satellites USERS and SERVIS-1 (*Kodaira et al.*, 2005). A detailed analysis of the slot region for this time period can be found in *Lazutin* (2012). The DOSTEL is designed to measure absorbed dose and dose equivalent rates and is not able to identify particle types and fluxes. Due to this, a more detailed comparison with the results from SAMPEX, USERS and SERVIS-1 can not be done. In the next section the additional absorbed dose due to the Slot Region Belt (SRB) will be estimated.

7.3. Additional Absorbed Dose due to the Slot Region Belt

The DOSTEL measures energy deposition spectra. How dose values are calculated from these spectra is shown in chapter 5. This chapter will focus on the additional absorbed dose due to the Slot Region Belt. This dose contribution is not included in the results presented for the MTR-1 mission phase in table 5.1. The absorbed dose rate measured by DOSTEL between April and June 2004 (370 $\frac{\mu Gy}{day}$) showed strong differences to the dose rate measured with the passive detectors between February 2004 and August 2005 (540-940 $\frac{\mu Gy}{day}$). Because of the poor DOSTEL data coverage during the Slot Region Belt (SRB) presence it is not possible to directly estimate the total absorbed dose induced by the SRB from this data. Electron fluxes measured by SAMPEX are used to scale the absorbed dose measured by DOSTEL at end of September 2004 to the whole time of the SRB presence to analyze if the SRB induced dose could explain the differences between the passive detectors and DOSTEL.
Figure 7.7 shows two LET-spectra of ascending (south to north) inner radiation belt crossings in May (red) and September (black) 2004 in the lower panel. The ISS positions during the spectra recording are shown in the upper panel in the same color code. For the May spectrum the ISS crossed the inner radiation belt a few degrees east in comparison to the September spectrum. This means the May spectrum belongs to an ISS track which was closer to the maximum flux of the inner radiation belt (see figure 4.10). The shapes of the LET-spectra are comparable but due to higher flux induced by the geographical differences the spectrum of May 2004 shows a higher particle flux than the September spectrum.

The LET-spectra of descending inner belt crossings from May and September 2004 can be seen in figure 7.8. This figure shows two LET spectra in the lower panel, again in red, a spectrum of the inner radiation belt crossing in May 2004 is shown. The black spectrum belongs to a crossing of the inner belt and the SRB in September 2004. The separation of radiation belt spectra is done on board via the slope of the count rate and a count rate threshold. The count rate does not fall below this threshold between inner belt crossing and SRB crossing. Because of this there are no LET spectra of just SRB crossing available. The upper panel shows the ISS positions during the time the spectra were obtained in the same color code. The SRB spectrum shows a strong enhancement of particles with LET below 2 $\frac{keV}{\mu m}$. This high flux difference in comparison to the May spectrum

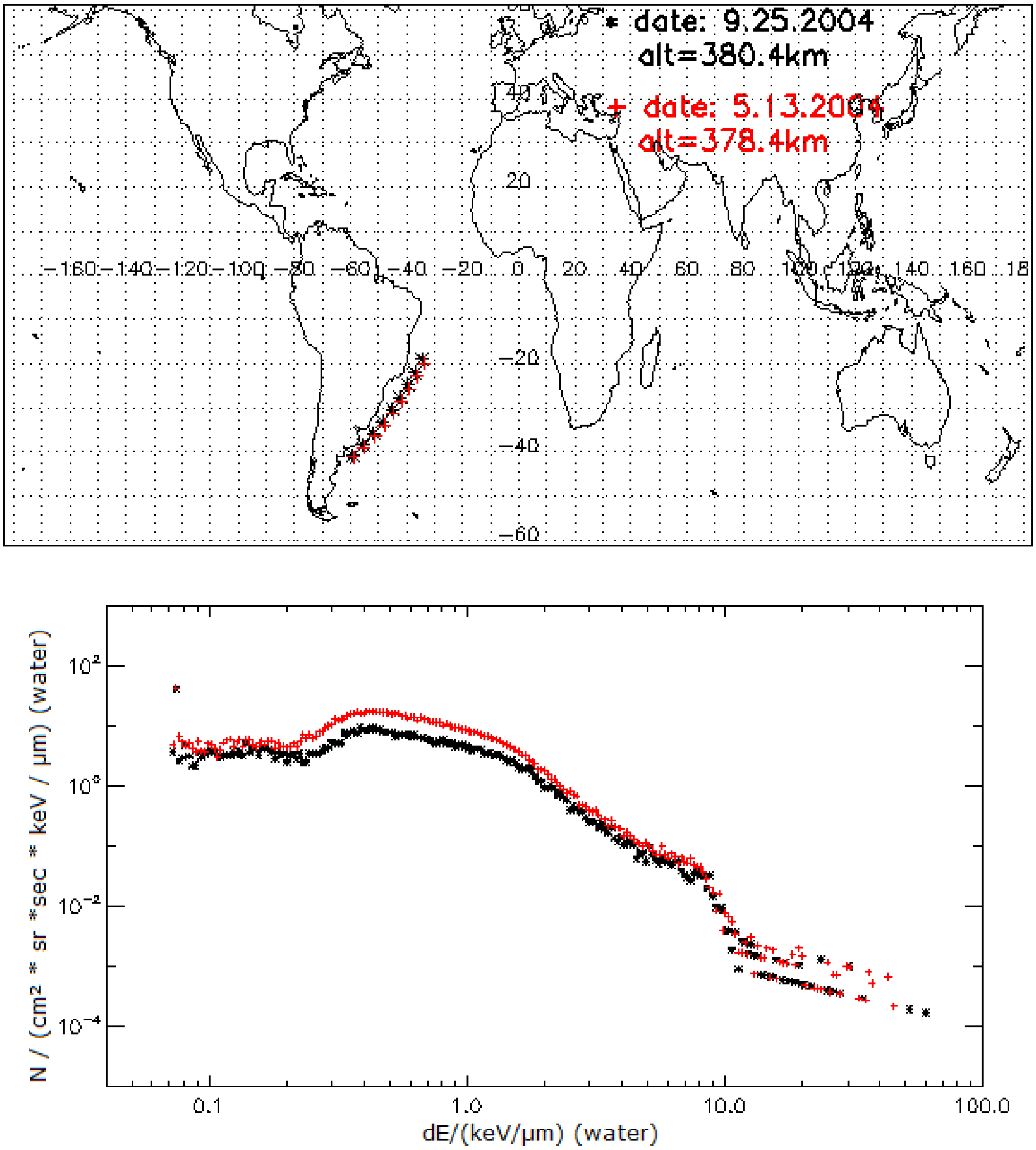

Figure 7.7.: The lower panel shows two LET-spectra of ascending inner radiation belt crossings measured by DOSTEL in May (red) and September (black) 2004. The upper panel shows the corresponding ISS orbits in the same color code.

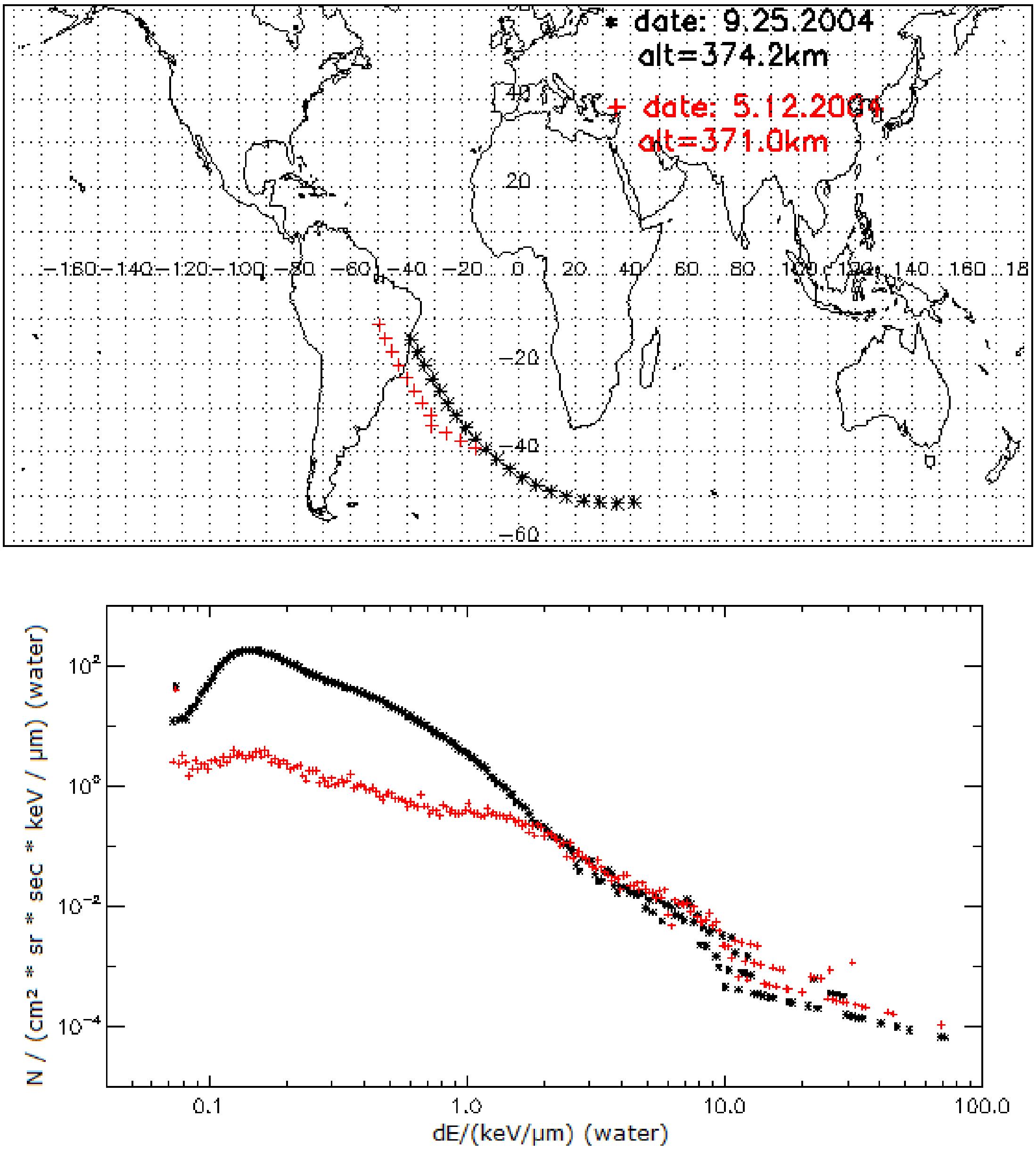

Figure 7.8.: The lower panel shows two LET-spectra measured by DOSTEL. In red, a spectrum of descending inner belt crossing in May 2004 is shown. The black spectrum shows the crossing of the inner belt and the Slot Region Belt (SRB) in September 2004. An enhancement of particles wit an LET below 2 $\frac{keV}{\mu m}$, which peaks at about 0.15 $\frac{keV}{\mu m}$, can be seen in the combined inner radiation belt and SRB spectrum.

can not result from changes of the inner radiation belt, whose flux did not change significantly (figure 7.7). This higher flux results from the crossing of the SRB. The comparison of the May and September spectrum shows that the particles in the SRB have an LET below 2 $\frac{keV}{\mu m}$. Most of these particles are minimal ionizing particles with an LET of ~0.18 $\frac{keV}{\mu m}$. This indicates that the particles in the SRB are mostly electrons. Minimal ionizing protons would also have an LET of ~0.18 $\frac{keV}{\mu m}$ but due to the higher mass of protons they have a higher rigidity and can not be trapped in Earth's magnetic field. Due to the high count rates during SRB crossings a dead time correction is necessary. The dead time correction was done for four example days of SRB and three example days of inner radiation belt crossings. The results can be seen in appendix B. The daily dose for these exemplary days was calculated (see table 7.1).

Table 7.1.: Mean corrected absorbed dose rates in water of radiation belt crossings during MTR-1 mission phase.

	undisturbed conditions April to June 2004	SRB presence September and October 2004
ascending	166.4 $\frac{\mu Gy}{day}$	160.4 $\frac{\mu Gy}{day}$
descending	122.2 $\frac{\mu Gy}{day}$	258.5 $\frac{\mu Gy}{day}$
total	288.6 $\frac{\mu Gy}{day}$	418.9 $\frac{\mu Gy}{day}$

The measured absorbed dose during ascending inner radiation belt crossings in the undisturbed conditions between April and June is 166 $\frac{\mu Gy}{day}$, which is comparable to the one measured during the SRB presence (160 $\frac{\mu Gy}{day}$). For the descending crossings of the inner radiation belt during undisturbed condition the mean daily absorbed dose is 122 $\frac{\mu Gy}{day}$. During September and October when the SRB was present the daily absorbed dose for descending crossings of inner belt and SRB is 259 $\frac{\mu Gy}{day}$. The SRB led to a daily absorbed dose enhancement of $\sim$ 130 $\frac{\mu Gy}{day}$. A temporal change in this value could not be resolved. There is only one day with total data coverage in September (25th) and the days with total data coverage in October (4th, 6th, and 7th) are too close to show temporal effects. The changes of the ISS tracks trough the SRB lead to stronger differences in the absorbed

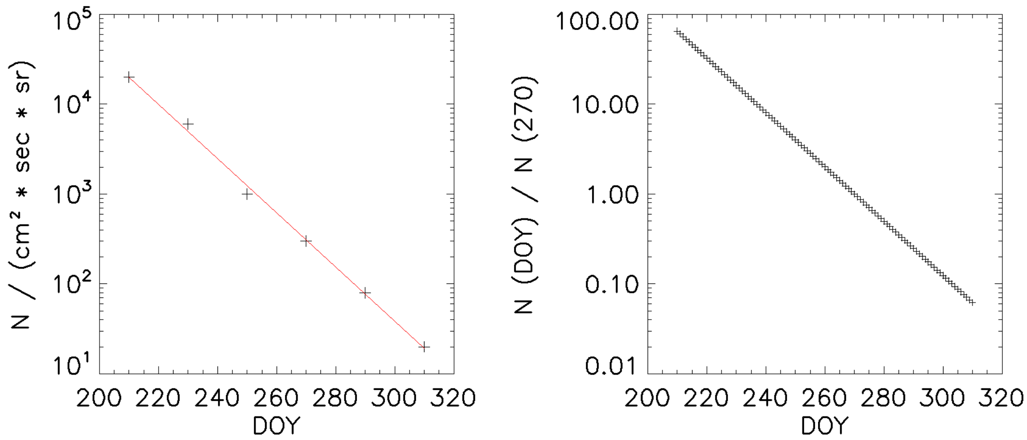

Figure 7.9.: The left panel shows a logarithmic time profile of the electron intensity at L=3. The values were adapted from figure 7.5. A least chi-square fit through the data points is shown in red. The right panel shows the electron intensity normalized to DOY 270 (end of September).

dose than the temporal decrease of the dose. Due to this the mean additional absorbed dose rate for the exemplary days is used for further analysis.

To estimate the absorbed dose resulting from the SRB from July to November 2004 the electron intensity measured by SAMPEX was used. The LET-spectra measured with DOSTEL showed that the SRB is dominated by high energy electrons. For the estimation of the absorbed dose during the whole presence of the SRB the SAMPEX electron intensity for electrons between 3.5 and 16 MeV (as shown in figure 7.5) was used to scale the DOSTEL measurements from September/October 2004 to the whole time period of the SRB presence. The electron intensity at L=3 was estimated by eye and the logarithmic values are plotted on the left panel of figure 7.9. The fitting function (red) was used to normalize the intensities to DOY 270 by dividing the fitting function in the right panel by the intensity of DOY 270. The daily normalized electron intensities are shown on the right panel. These normalized values are the factors which have to be multiplied to the intensity of DOY 270 to obtain the intensity of the belonging DOY. The values are greater than one for days before DOY 270 and lower than one for days after DOY 270. The sum of the normalized intensities indicates the total electron intensity in numbers of electrons at DOY 270. The DOSTEL measurements for September/October 2004 have shown an additional absorbed dose due to the

SRB of $\sim 130\ \frac{\mu Gy}{day}$. The number of electrons at DOY 270 lead to an absorbed dose of $\sim$130 μGy. To obtain the total absorbed dose, one would measure during the whole presence of the SRB, this value has then to be multiplied with the sum of the normalized electron intensity ($I_{e,n}$). This calculation is shown in equation 7.1.

$$\sum_{DOY} I_{e,n}(DOY) = 966 \tag{7.1}$$

$$D_{SRB} \approx 966 \cdot 130\mu Gy = 125568\mu Gy$$

To compare this total absorbed dose with the results obtained with the passive detectors of MTR an absorbed dose rate has to be calculated. This is done in equation 7.2. The total absorbed dose is divided by the mission time of MTR-1 which was roughly 1.5 years.

$$\dot{D}_{SRB} \approx \frac{125568\mu Gy}{365 * 1.5 days} \approx 230 \frac{\mu Gy}{day} \tag{7.2}$$

The SRB crossings between July and November 2004 lead to an absorbed dose rate enhancement of $\sim 230\ \frac{\mu Gy}{day}$ for the MTR passive detectors. An additional by eye estimation of the electron intensity in figure 7.5 led to a comparable result for the additional absorbed dose. Intentional high and low estimations result in ± 35 % differences to the shown result which can be taken as the uncertainty in the SRB dose. There was a second filling of the Slot region with electrons observed by SAMPEX at DOY 318 of 2004 (see figure 7.10). These two radiation belts in the Slot region can explain differences between DOSTEL absorbed dose measurements from April to June 2004 (370 $\frac{\mu Gy}{day}$) and passive detector measurements from February 2004 to August 2005 (540-940 $\frac{\mu Gy}{day}$) up to $2 \cdot 230\ \frac{\mu Gy}{day} \approx 460\ \frac{\mu Gy}{day}$. An overview of these absorbed dose values is presented in table 7.2.

Table 7.2.: Additional absorbed dose rate D induced by particle from the SRB in comparison to the MTR-1 results of DOSTEL and passive detectors.

	DOSTEL MTR-1 without SRB dose	passive detectors MTR-1 with SRB dose	SRB dose
$\dot{D}$ / ($\frac{\mu Gy}{day}$)	370	540-970	$\sim$ 460

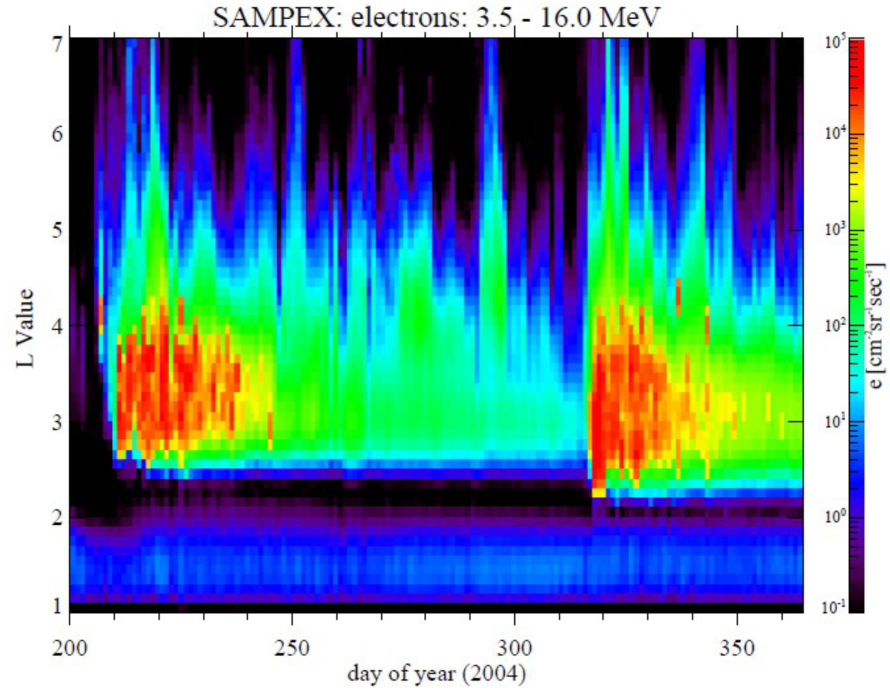

Figure 7.10.: SAMPEX measurements of 3.5 to 16.0 MeV electrons from DOY 200 to DOY 365 of year 2004. From DOY 209 on and also from DOY 318 on the Slot region was filled with relativistic electrons as seen in the increase of the electron flux. The picture was taken from http://lasp.colorado.edu:8080/sampex_jsp/elo-lsort.jsp in July 2010.

8. Conclusion

In this work the data obtained with the active Dosimetry Telescope (DOSTEL), which was a part of the MATROSHKA (MTR) experiment, was analyzed. The count rate dependence on the Effective Vertical Geomagnetic Cutoff Rigidity (R_c) was analyzed and compared with the theoretical relation derived from Galactic Cosmic Ray (GCR) energy spectra (*Usoskin et al.*, 2005). This comparison led to a rigidity depending yield function (formula 4.8) which is a measure for the number of secondary particles per primary particle. Furthermore the count rate R_c relation was used to correct the imprecise DOSTEL data time. By use of the time corrected DOSTEL data and ISS orbit data it was possible to derive the geographical count rate distribution (figure 4.10), as well as the count rate dependence on the McIllwain L-parameter (figure 4.11). The crossings of the inner radiation belt in the region of the SAA could be linked to L-values between 1.2 and 2.0 which is the typically L-value for the inner radiation belt.

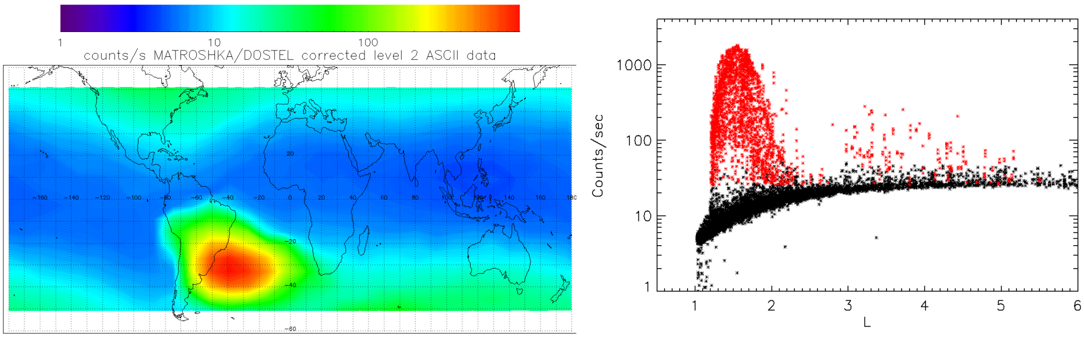

Geographical (left side) and L-parameter (right side) count rate distribution for May 2004 during the MTR-1 mission phase.

By using the two different DOSTEL modes it was possible to analyze the angular distribution of GCR particles for the MTR-1 mission phase. The count and dose rate ratios of a single and a telescope detector could not be explained with isotropic particle incidence. With a geometric Monte-Carlo simulation it was possible to estimate the zenith angle distribution. A $\sin(\theta) \cdot \cos(\theta) \cdot \cos^n(\theta)$ distribution with $1 \leq n \leq 1.5$ could reproduce the DOSTEL measurements. The distribution of SAA protons was analyzed in a case study. A simple model of particle incidence from a plane perpendicular to the magnetic field could not explain the observations. The East-West effect and the shielding of the ISS would have to be considered for a deeper analysis in the future.

The dose values were calculated from the energy deposition spectra measured with DOSTEL and are shown in table 8.1.

Table 8.1.: Absorbed dose rate $\dot{D}$ and the dose equivalent rate $\dot{H}$ for the GCR and the SAA component as well as the sum of both (total) for the time period of April 13th to June 30th 2004 during the MTR-1 mission phase and April 8th to June 15th 2008 during MTR-2B mission phase.

MTR 1	$\dot{D}$ / $(\mu Gy \cdot day^{-1})$	$\dot{H}$ / $(\mu Sv \cdot day^{-1})$	$\langle Q \rangle$
GCR	77.6	245.5	3.16
SAA	296.1	367.1	1.24
total	373.7	612.3	1.64
MTR 2B			
GCR	115.6	309.8	2.79
SAA	45.8	72.4	1.58
total	161.4	382.2	2.37

The uncertainty (± 5 %) of the presented dose values is dominated by the uncertainty of the conversion from deposited energy in silicon to deposited energy in water. In this work a constant conversion factor was used. An LET dependent conversion factor could minimize the uncertainty of the conversion and should be taken into account for future analysis.

During the outside measurements (MTR-1) the radiation exposure is dominated by trapped particles of the inner radiation belt (SAA). Even if the exposure time of trapped particles of the inner radiation belt is only 1.2 hours, these particles contribute 80 % to the total daily absorbed dose. The GCR contribution has a higher biological effectiveness which results in a higher mean quality factor. The contribution of trapped particles to the total dose equivalent rate thus decreases and accounts for 60 % of the total daily dose equivalent.

For the inside measurements (MTR-2B) the contribution of trapped particles strongly decreases. The protons of the inner radiation belt are effectively shielded by the space craft hull. While the daily absorbed dose induced by GCR particles increased during the inside exposure (solar cycle variation), the contribution of trapped particles accounted only 30 % to the total absorbed dose. Due to the lower mean quality factor the contribution of the trapped particles to the daily dose equivalent is less than 20 %. The dose values measured during MTR-2B are in good agreement with the results of the passive radiation detectors of MTR (*Berger et al.*, 2013) and the Russian DB-8 units at comparable locations (*Lishnevskii et al.*, 2010).

The comparison of the MTR-1 DOSTEL findings with those obtained with passive dosimeters have shown discrepancies. These discrepancies result from an additional radiation belt in the slot region. This region between the L-values 2 and 3 is characterized by a low flux of trapped particles under normal conditions. DOSTEL data from September to October 2004 have shown that the region between L-values of 2.5 and 3.5 was populated with relativistic electrons during this time period. These electrons formed a quasi-stable Slot Region Belt (SRB) which reached down to ISS altitudes in the region south of South Africa.

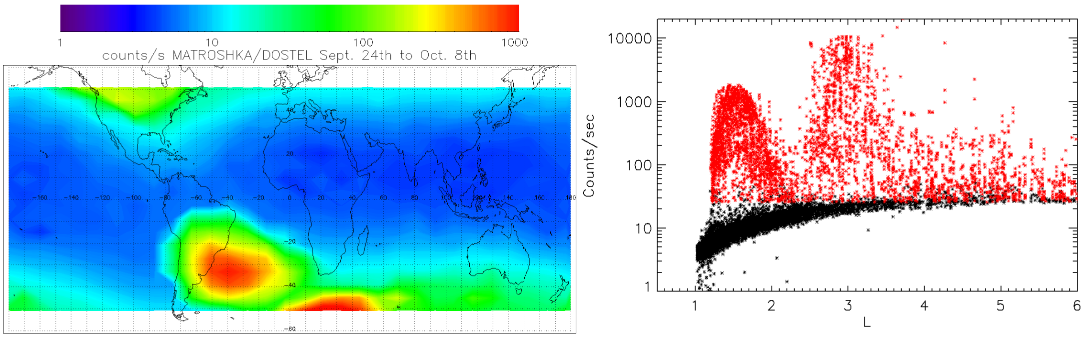

Geographical(left side) and L-parameter (right side) count rate distribution for September and October 2004 during the MTR-1 mission phase. Besides the crossing of the inner radiation belt in the SAA region ($1 < L < 2$) an additional region with enhanced count rate can be seen south of South Africa ($2.5 < L < 3.5$).

The MTR DOSTEL data allowed dose measurements during ISS crossings of the SRB for the first time. The SRB led to a daily absorbed dose enhancement of $\sim 130\ \frac{\mu Gy}{day}$ for the time of September 24th to October 8th 2004. Measurements of the Solar Anomalous and Magnetospheric Particle Explorer (SAMPEX) have shown a filling of the slot region with particles at July 27th 2004. The particle intensity decreased in time but was observable until November 2004. The intensity of electrons from 3.5 to 16 MeV measured by SAMPEX were used to scale the absorbed dose measured with DOSTEL to the total time of the SRB presence. This estimation led to an additional dose due to the SRB of $125mGy$ which results in an additional absorbed dose rate observed by the passive detectors of MTR of $230\frac{\mu Gy}{day}$. This additional dose, combined with a second slot region filling in November 2004, explains the discrepancies between the DOSTEL and passive detector measurements during the outside exposure. The DOSTEL measurements have shown that the passive detectors have not measured during undisturbed conditions in Low Earth Orbit (LEO). This led to a better understanding of the the MTR-1 results obtained with the passive detectors.

Bibliography

Allkofer, O. C., *Teilchen Detektoren*, Verlag Karl Thiemig KG München, 1971.

Badavi, F. F., J. E. Nealy, and J. W. Wilson, The Low Earth Orbit validation of a dynamic and anisotropic trapped radiation model through ISS measurements, *Advances in Space Research*, *48*(8), 1441 – 1458, 2011.

Badhwar, G., W. Atwell, G. Reitz, R. Beaujean, and W. Heinrich, Radiation measurements on the Mir Orbital Station, *Radiation Measurements*, *35*(5), 393 – 422, 2002.

Baker, D., G. Mason, O. Figueroa, G. Colon, J. Watzin, and R. M. Aleman, An overview of the Solar Anomalous, and Magnetospheric Particle Explorer (SAMPEX) mission, *IEEE Transactions on Geoscience and Remote Sensing*, *31*(3), 531–541, 1993.

Baker, D. N., S. G. Kanekal, X. Li, S. P. Monk, J. Goldstein, and J. L. Burch, An extreme distortion of the Van Allen belt arising from the Halloween solar storm in 2003, *Nature*, *432*(7019), 878–881, 2004.

Baker, D. N., S. G. Kanekal, R. B. Horne, N. P. Meredith, and S. A. Glauert, Low-altitude measurements of 2-6 MeV electron trapping lifetimes at $1.5 \leq$ L ≤ 2.5, *Geophysical Research Letters*, *34*(20), 2007.

Beaujean, R., J. Kopp, and G. Reitz, Radiation Exposure in Civil Aircraft, *Radiation Protection Dosimetry*, *85*, 287–290, 1999a.

Beaujean, R., J. Kopp, and G. Reitz, Active dosimetry on recent space flights, *Radiation protection dosimetry*, *85*(1-4), 223–226, 1999b.

Beaujean, R., G. Reitz, and J. Kopp, Recent European measurements inside Biorack, *Mutation Research/Fundamental and Molecular Mechanisms of Mutagenesis*, *430*(2), 183 – 189, 1999c.

Beaujean, R., J. Kopp, S. Burmeister, F. Petersen, and G. Reitz, Dosimetry inside MIR station using a silicon detector telescope (DOSTEL), *Radiation Measurements*, *35*(5), 433 – 438, 2002.

Berger, T., P. Bilski, M. Hajek, M. Puchalska, and G. Reitz, The MATROSHKA Experiment: Results and Comparison from Extravehicular Activity (MTR-1) and Intravehicular Activity (MTR-2A/2B) Exposure, *Radiation Research*, *180*(6), 622–637, 2013.

Beringer et al. (Particle Data Group), J., *Phys. Rev. D86, 010001*, 2012.

Brueckner, G. E., et al., Geomagnetic storms caused by coronal mass ejections (CMEs): March 1996 through June 1997, *Geophysical Research Letters*, *25*(15), 3019–3022, 1998.

Burmeister, S., T. Berger, G. Reitz, R. Beaujean, M. Boehme, L. Haumann, J. Labrenz, and O. Kortmann, The DOSIS and DOSIS 3D Experiments onboard the International Space Station - Results from the Active DOSTEL Instruments, in *39th COSPAR Scientific Assembly*, *COSPAR Meeting*, vol. 39, p. 261, 2012.

Caballero-Lopez, R. A., and H. Moraal, Cosmic-ray yield and response functions in the atmosphere, *Journal of Geophysical Research (Space Physics)*, *117*, A12103, 2012.

Cane, H. V., and D. Lario, An Introduction to CMEs and Energetic Particles, *Space Science Reviews*, *123*, 45–56, 2006.

Casolino, M., N. De Simone, D. Bongue, M. De Pascale, V. Di Felice, L. Marcelli, and the PAMELA Group, Two Years of Flight of the Pamela Experiment: Results and Perspectives, *ArXiv:0810.4980v1*, 2008.

Dettmann, J., G. Reitz, and G. Gianfiglio, MATROSHKA-The first ESA external payload on the International Space Station, *Acta Astronautica*, *60*(1), 17 – 23, 2007.

Doke, T., T. Hayashi, and T. B. Borak, Comparisons of LET Distributions Measured in Low-Earth Orbit Using Tissue-Equivalent Proportional Counters and the Position-Sensitive Silicon-Detector Telescope (RRMD-III), *Radiation Research*, *156*(3), 310 – 316, 2001.

Dresing, N., R. Gómez-Herrero, A. Klassen, B. Heber, Y. Kartavykh, and W. Dröge, The large longitudinal spread of solar energetic particles during the 17 january 2010 solar event, *Solar Physics*, *281*(1), 281–300, 2012.

Durante, M., and F. A. Cucinotta, Physical basis of radiation protection in space travel, *Rev. Mod. Phys.*, *83*, 1245–1281, 2011.

Grupen, C., *Teilchendetektoren*, Bibliographisches Institut & F.A. Brockhaus AG, Mannheim, 1993.

Heber, B., Energetic Particles in the Heliosphere, *International Journal of Modern Physics A*, *20*, 6621–6632, 2005.

Heber, B., and M. S. Potgieter, Cosmic Rays at High Heliolatitudes, *Space Science Reviews*, *127*, 117–194, 2006.

Herbst, Computed vertical cutoff rigidity, private correspondence, 2009.

Herbst, K., Interaction of Cosmic Rays with The Earth' Magnetosphere and Atmosphere - Modeling the Cosmic Ray Induced Ionization and the Production of Cosmogenic Radionuclides, Ph.D. thesis, Christian-Albrechts-Universität zu Kiel, Germany, 2012.

Hess, V., Über Beobachtungen der durchdringenden Strahlung bei sieben Freiballonfahrten, *Physikalische Zeitschrift*, *13*, 1084–1091, 1912.

ICRP, 1990 Recommendations of the International Commission on Radiological Protection, *Pergamon Press, Oxford, United Kingdom*, *ICRP Publication 60, Ann. ICRP 21(1-3)*, 1991.

ICRU, *Stopping Powers for Electrons and Protons*, Report 37, International Commission on Radiation Units and Measurement Bethesda, MD:ICRU, 1984.

International Association of Geomagnetism and Aeronomy, Working Group V-MOD. Participating members, et al., International geomagnetic reference field: the eleventh generation, *Geophysical Journal International*, *183*(3), 1216–1230, 2010.

Knoll, G. F., *Radiation Detection and Measurement*, John Wiley & Sons, Inc., 2000.

Kodaira, S., et al., Space and Time Correlations of Particle Fluxes after Giant Flares in Radiation Belts Observed by Two Satellites, USERS and SERVIS-1, in *Proceedings of the 29th International Cosmic Ray Conference, Pune, 101 - 104*, 2005.

Kress, B. T., M. K. Hudson, and P. L. Slocum, Impulsive solar energetic ion trapping in the magnetosphere during geomagnetic storms, *Geophysical Research Letters*, *32*(6), L06 108, 2005.

Kuznetsov, S., L. Lazutin, M. Panasyuk, L. Starostin, Y. Gotseliuk, N. Hasebe, K. Sukurai, and M. Hareyama, Solar particle dynamics during magnetic storms of July 23 - 27, 2004, *Advances in Space Research*, *43*(4), 553 – 558, 2009.

Lazutin, L., On radiation belt dynamics during magnetic storms, *Advances in Space Research*, *49*(2), 302 – 315, 2012.

Lishnevskii, A., M. Panasyuk, V. Benghin, V. Petrov, A. Volkov, and O. Nechayev, Variations of radiation environment onboard the ISS in the year 2008, *Cosmic Research*, *48*(3), 206–210, 2010.

Lyons, L. R., and R. M. Thorne, Equilibrium structure of radiation belt electrons, *Journal of Geophysical Research*, *78*, 2142–2149, 1973.

McIlwain, C. E., Coordinates for mapping the distribution of magnetically trapped particles, *Journal of Geophysical Research*, *66*(11), 3681–3691, 1961.

Meredith, N. P., R. B. Horne, S. A. Glauert, and R. R. Anderson, Slot region electron loss timescales due to plasmaspheric hiss and lightning-generated whistlers, *Journal of Geophysical Research (Space Physics)*, *112*, A08214, 2007.

Meredith, N. P., R. B. Horne, S. A. Glauert, D. N. Baker, S. G. Kanekal, and J. M. Albert, Relativistic electron loss timescales in the slot region, *Journal of Geophysical Research (Space Physics)*, *114*, A03 222, 2009.

Millan, R., and R. Thorne, Review of radiation belt relativistic electron losses, *Journal of Atmospheric and Solar-Terrestrial Physics*, *69*(3), 362 – 377, 2007.

Miyoshi, Y., A. Morioka, and H. Misawa, Long term modulation of low altitude proton radiation belt by the Earth's atmosphere, *Geophysical Research Letters*, *27*(14), 2169–2172, 2000.

Pazmandi, S., T.; Deme, Tissue dose conversion factors for protons and alpha particles in case of different detector materials, in *In: Proceedings of IRPA Regional Congress on Radiation Protection in Central Europe, Bratislava, September 2003. Published on CD-ROM ISBN 80-88806-43-7*, 2003.

Proelss, G. W., *Physik des erdnahen Weltraums. Eine Einfuehrung*, Springer, Berlin, 2008.

Reames, D. V., Solar energetic particle variations, *Advances in Space Research*, *34*, 381–390, 2004.

Reitz, G., Characteristic of the radiation field in low earth orbit and in deep space, *Zeitschrift für Medizinische Physik*, *18*(4), 233 – 243, 2008.

Reitz, G., and T. Berger, The MATROSHKA facility - dose determination during an EVA, *Radiation Protection Dosimetry*, *120*(1-4), 442 – 445, 2006.

Reitz, G., R. Beaujean, E. Benton, S. Burmeister, T. Dachev, S. Deme, M. Luszik-Bhadra, and P. Olko, Space radiation measurements on-board ISS - the DOSMAP experiment, *Radiation Protection Dosimetry*, *116*(1-4), 374 – 379, 2005.

Reitz, G., et al., Astronaut's Organ Doses Inferred from Measurements in a Human Phantom Outside the International Space Station, *Radiation Research*, *171*(2), 225 – 235, 2009.

Sakaguchi, T., et al., Measurement of the directional distribution of incident particles in the shuttle-mir mission orbit, *Journal of Geophysical Research (Space Physics)*, *104*(A10), 22,793–22,799, 1999.

Shea, M., D. Smart, and L. Gentile, Estimating cosmic ray vertical cutoff rigidities as a function of the McIlwain L-parameter for different epochs of the geomagnetic field, *Physics of the Earth and Planetary Interiors*, *48*(3 - 4), 200 – 205, 1987.

Shurshakov, V., V. Petrov, N. Panova, Y. Ivanov, V. Makhmutov, T. Dachev, and J. Semkova, Experimental investigations of quasistable radiation belts formed after solar proton events in September & October 1989 and March 1991 based on measurements made by "Liulin" dosimeter-radiometer on board the "MIR" space station, *Advances in Space Research*, *18*(12), 251–257, 1996.

Simpson, J., Elemental and Isotopic Compostion of the Galatic Cosmic Rays, *Annual Reviews of Nuclear and Particle Science*, *33*, 323–381, 1983.

Singh, A., R. Singh, and D. Siingh, State studies of earth's plasmasphere: A review, *Planetary and Space Science*, *59*(9), 810 – 834, 2011.

Smart, D., and M. Shea, Fifty years of progress in geomagnetic cutoff rigidity determinations, *Advances in Space Research*, *44*(10), 1107 – 1123, 2009.

Størmer, C., On the Trajectories of Electric Particles in the Field of a Magnetic Dipole with Applications to the theory of Cosmic Radiation. First Communication., *Publications of the Oslo Observatory, vol. 1, Ji-JPIX*, *1*, J1, 1933.

Sugiura, M., Hourly values of equatorial dst for the igy, *Annals of the IGY*, *35*, 9 – 45, 1964.

Sullivan, J., Geometric factor and directional response of single and multi-element particle telescopes, *Nuclear Instruments and Methods*, *95*(1), 5 – 11, 1971.

Sullivan, J. D., Erratum: Geometrical factor and directional response of single and multi-element particle telescopes., *Nuclear Instruments and Methods*, *98*, 187, 1972.

Usoskin, I. G., K. Alanko-Huotari, G. A. Kovaltsov, and K. Mursula, Heliospheric modulation of cosmic rays: Monthly reconstruction for 1951-2004, *Journal of Geophysical Research (Space Physics)*, *110*(A12), 108, 2005.

Van Allen, J. A., and L. A. Frank, Radiation Around the Earth to a Radial Distance of 107,400 km., *Nature*, *183*(4659), 430 – 434, 1959.

White, R. S., High-energy proton radiation belt., *Reviews of Geophysics and Space Physics*, *11*, 595 – 632, 1973.

Yermolaev, Y. I., N. S. Nikolaeva, I. G. Lodkina, and M. Y. Yermolaev, Geoeffectiveness and efficiency of cir, sheath, and icme in generation of magnetic storms, *Journal of Geophysical Research (Space Physics)*, *117*(A9), A00L07, 2012.

Zhang, J., et al., Solar and interplanetary sources of major geomagnetic storms (Dst $\leq$ -100 nT) during 1996-2005, *Journal of Geophysical Research (Space Physics)*, *112*, A10102, 2007.

Zheng, Y., A. T. Y. Lui, X. Li, and M.-C. Fok, Characteristics of 2-6 MeV electrons in the slot region and inner radiation belt, *Journal of Geophysical Research (Space Physics)*, *111*, A10204, 2006.

Zhou, D., E. Semones, D. OSullivan, N. Zapp, M. Weyland, G. Reitz, T. Berger, and E. Benton, Radiation measured for MATROSHKA-1 experiment with passive dosimeters, *Acta Astronautica*, *66*(1-2), 301 – 308, 2010.

List of Figures

List of Tables

A. Additional Plots

A.1. Energy Deposition Spectra of GCR Component April to June 2004

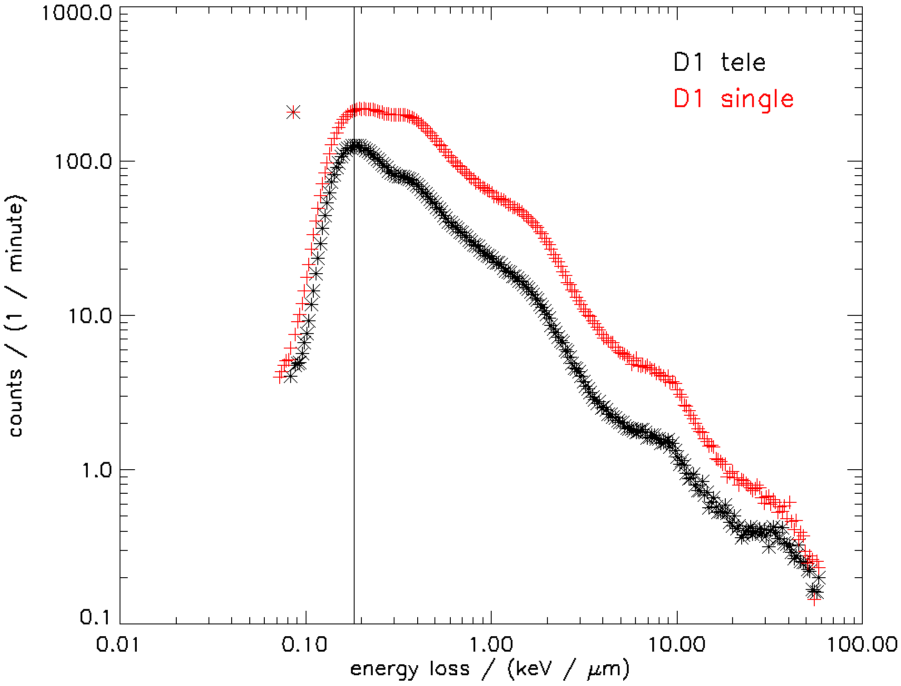

Figure A.1.: Count rate per minute in dependence of the LET for the lower PIPS detector D1. The data from April to June 2004 were used for this plot. The count rate for the detector in single mode is shown red. The count rate in telescope mode (black) is lower than in single mode. Both count rates have their maximum at LET $= 0.18\ \frac{keV}{\mu m}$.

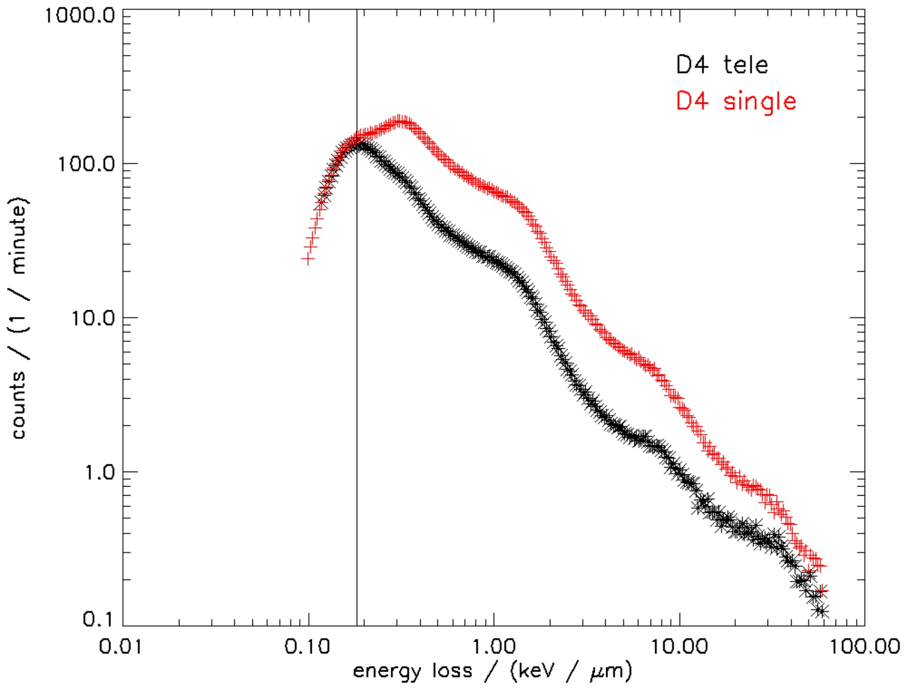

Figure A.2.: The count rates over LET for detector D4 (upper PIPS) is shown for single mode (red) and telescope mode (black). For LET's below 0.18 $\frac{keV}{\mu m}$ both count rate are identical. The energy loss in this detector is too low to trigger the electronics. The particles have to hit the other PIPS detector to be counted. Due to this the count rates for single mode and telescope mode are identical.

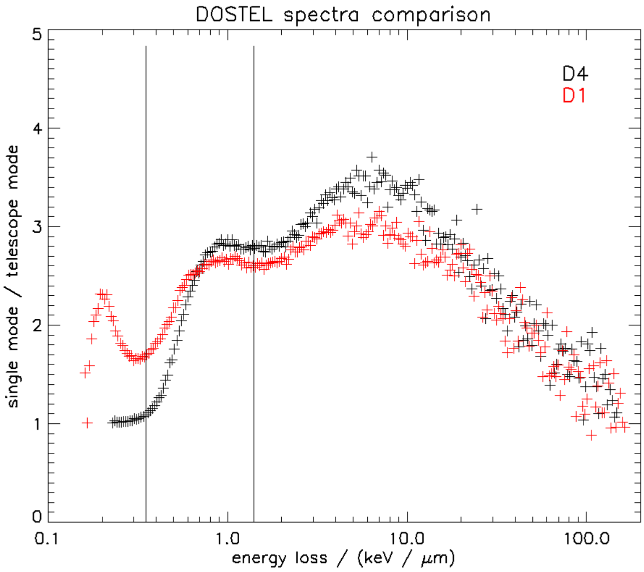

Figure A.3.: Count rate ratio of single and telesope mode over dE/dx for detector D4 (upper PIPS in black) and detector D1 (lower PIPS in red). For dE/dx below 0.34 $\frac{keV}{\mu m}$ the count rate ratio is 1 for D4 (see figure A.2). The D1 detector shows a minimum at 0.34 $\frac{keV}{\mu m}$ (black line). At $4 \cdot 0.34 \frac{keV}{\mu m}$ (energy loss of minimal ionizing Helium) a local minumum can be seen (second black line).

A.2. DOSTEL Dose Values

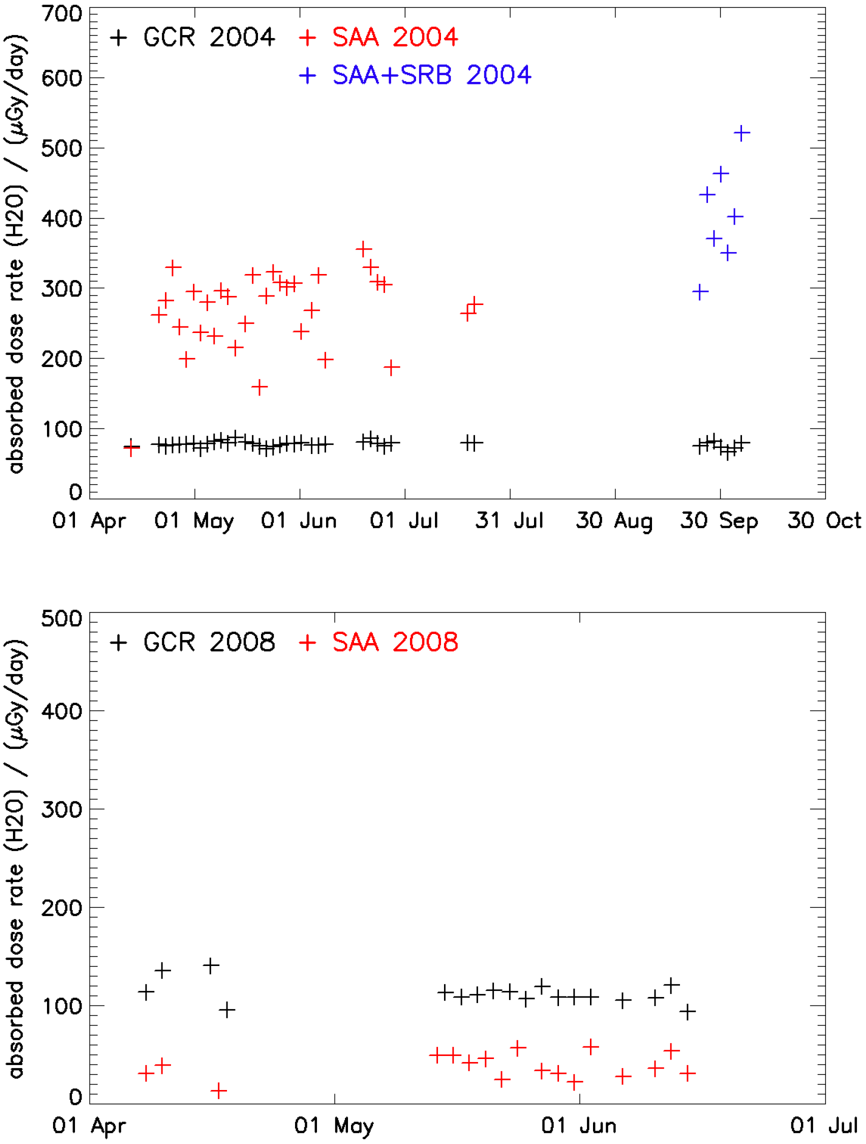

Figure A.4.: 2-daily averaged absorbed dose rate for the total time coverage of the MTR-1 (upper pannel) and MTR-2B (lower pannel) mission. The absorbed dose rates for SAA (red) and SRB crossings (blue) during MTR-1 were corrected by use of the dead time correction factors presented in appendix B (1.17 for SAA and 1.41 for SRB).

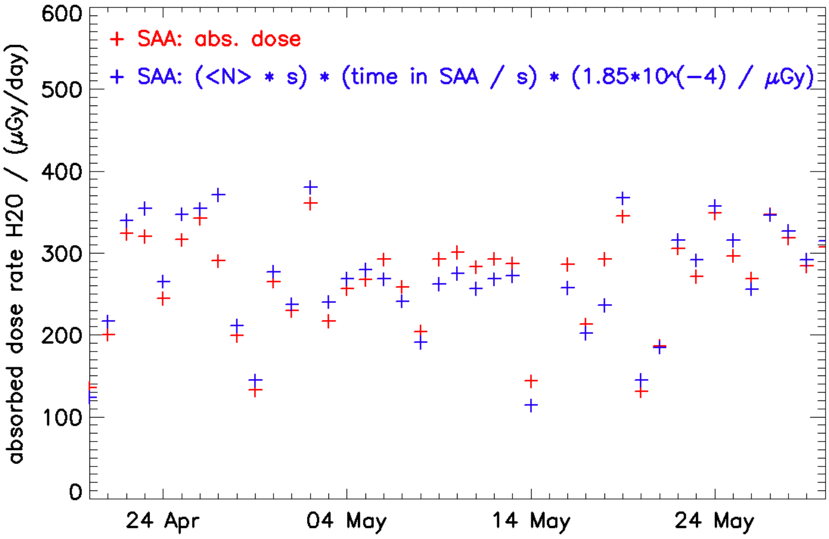

Figure A.5.: MTR-1 daily absorbed SAA dose rate and SAA counts times a constant dose per counts. The red crosses show the daily absorbed dose rate in the SAA region. The total daily count rate (from the sum counter) in the SAA region multiplied with a dose per count of 0.185 nGy is shown in blue. The good agreement between these two values shows that a constant dose per count for SAA crossings is suitable. The daily absorbed dose in the SAA region as a first approximation only depends on the number of particles measured during SAA region crossings.

B. Dead Time Correction

The dead time of the DOSTEL electronics is $\tau = 200\ \mu\text{s}$. This means the electronics needs 200 μs to process one event. During this time no other event can be counted. Due to this it is necessary to make a dead time correction, especially during high count rates (SAA crossing). The corrected count rate N_C can be calculated by the following formula.

$$N_C = \frac{N_M}{1 - \tau \cdot N_M} \tag{B.1}$$

N_C = corrected count rate
N_M = measured count rate
τ = dead time = 200 μs

For the GCR component during MTR-1 a dead time correction is not necessary. The average measured count rate is around 10 particles per second. This leads to a corrected count rate of 10.02 particles per second. This small correction can be neglected. For SAA crossing the measured count rate goes up to 1000 particles per second. In this case the corrected count rate is 1250 counts per second, showing a significant enhancement and, thus, making the dead time correction necessary.

B.1. Dead Time Correction for SAA Crossings

For the dead time correction of the SAA energy deposition spectra, which are integrated over several minutes, the count rate measurements for the same time period have to be used. These count rate measurements have a time resolution of 20 seconds. For every SAA crossing all counted particles from the count rate data are summed up over the integration period of the energy deposition spectrum to get the total number of measured counts. After the time correction for every 20 seconds count rate interval the corrected counts are again summed up to get the total number of corrected counts. The ratio between total counts corrected and total counts measured is used as the correction factor for this energy deposition spectrum.

$$F_{corr} = \frac{\sum N_C}{\sum N_M} \tag{B.2}$$

There is no information available which part of the energy deposition spectrum was recorded during which time of the measurement interval. Due to this the correction factor for the absorbed dose from an energy deposition spectrum is a mean value over the total time interval. The dead time correction was done for the three following examples days.
Day1: 27.04.2004
Day2: 13.05.2004
Day3: 05.06.2004
For each of these days seven energy deposition spectra in SAA-mode were measured. This means total data coverage of the SAA crossing. For example day 1 the tracks of the spectra are shown in figure B.1. The upper panel of figure B.1 shows the 4 ascending crossing of the SAA region. They are counted from west to east with type 1 to type 4. The 3 descending crossings of the SAA region (type 5 to type 7) are shown in the lower panel.

Table B.1.: Dead time correction factors for the seven inner radiation belt crossing in the region of the SAA for example day 1.

Type	1	2	3	4	5	6	7
F_{corr}	1.02	1.17	1.23	1.05	1.22	1.10	1.02

The correction factors for all SAA-mode spectra of example day 1 are shown in table B.1. To get the dead time correction factor for the whole example day the absorbed dose for every SAA-crossing was calculated as described in chapter 5.1. To correct these results the corresponding correction factor was used. The correction factor for the whole day is then obtained by dividing the sum of the

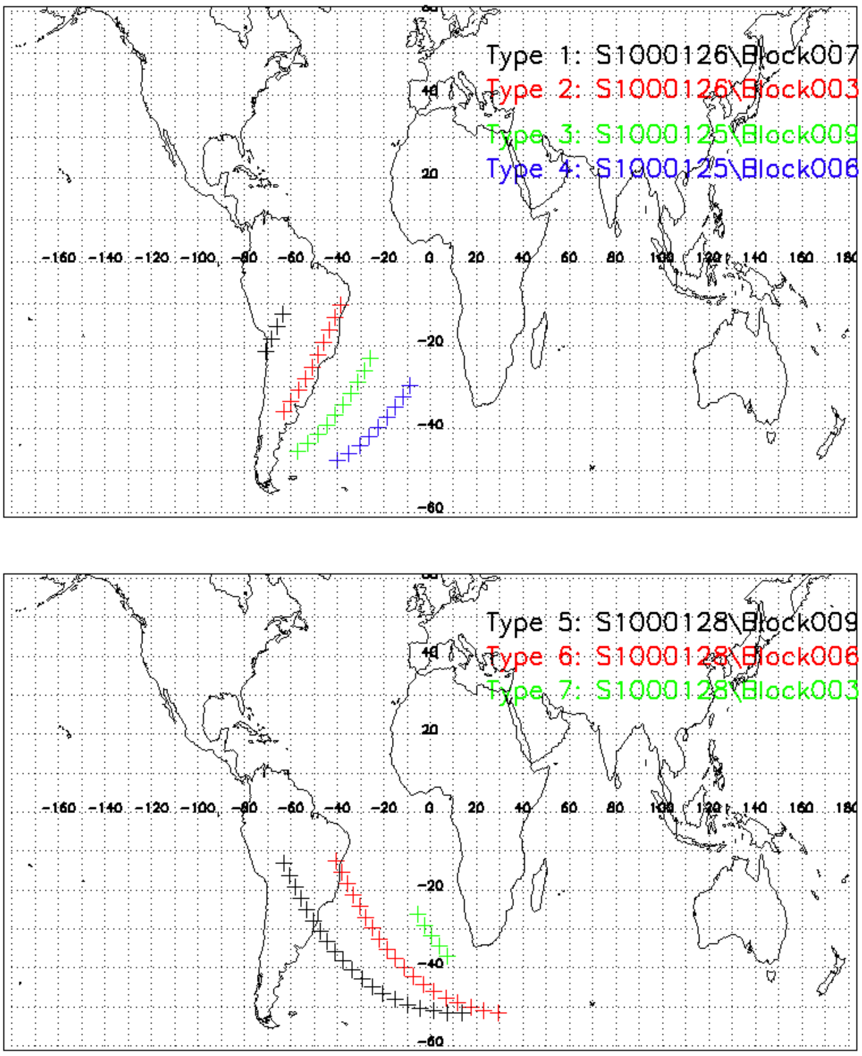

Figure B.1.: Crossings of the inner radiation belt in the SAA region on example day 1. The upper panel shows the ascending and the lower panel the descending crossings. The tracks and the belonging spectra are labeled with $type_i$ in the same color code.

corrected absorbed dose (D_{corr}) by the sum of the uncorrected absorbed dose (D).

$$F_{corr-day} = \frac{\sum D_{corr-i}}{\sum D_i} \tag{B.3}$$

Table B.2.: Daily dead time correction factors for the three example days. The correction factors are given for all ascending SAA crossing, all descending SAA crossing and all SAA crossings of the day. Because of different number of total counts in the different crossings, the combined factor is not the mean of ascending and descending SAA crossings.

Example day	1	2	3
$F_{corr-day}$ ascending	1.18	1.16	1.21
$F_{corr-day}$ descending	1.18	1.11	1.12
$F_{corr-day}$ all	1.18	1.14	1.18

The results of the correction factors for all example day are shown in table B.2. The mean value of the correction factors for all SAA crossings is:

$$\langle F_{corr-day} \rangle = 1.17 \ \pm 0.03$$

This factor was used to correct the daily absorbed dose values during SAA crossing for the MTR 1 mission phase in 2004 (see table 5.1). For the MTR 2B mission phase a dead time correction like this is not feasible. Because of noise in one of the PIPS detectors, a correction of the starting time of DOSTEL data packages, and, thus, a verification of tracks like in figure B.1 is not possible. Nevertheless, the normal observed peak heights in the count rates during SAA crossings are less than 500 counts per second. The mean dead time correction factors for the MTR 2B SAA spectra are shown in figure B.2. The minimum correction factor is 1.017 and the maximum value is 1.091. The mean of all correction factors is 1.048. This means the average dead time correction leads to 4.8% higher results for the absorbed dose rate.

Due to the noise in one of the detectors, the count rate during GCR mode is increased for MTR 2B. The average measured count rate is around 130 particles

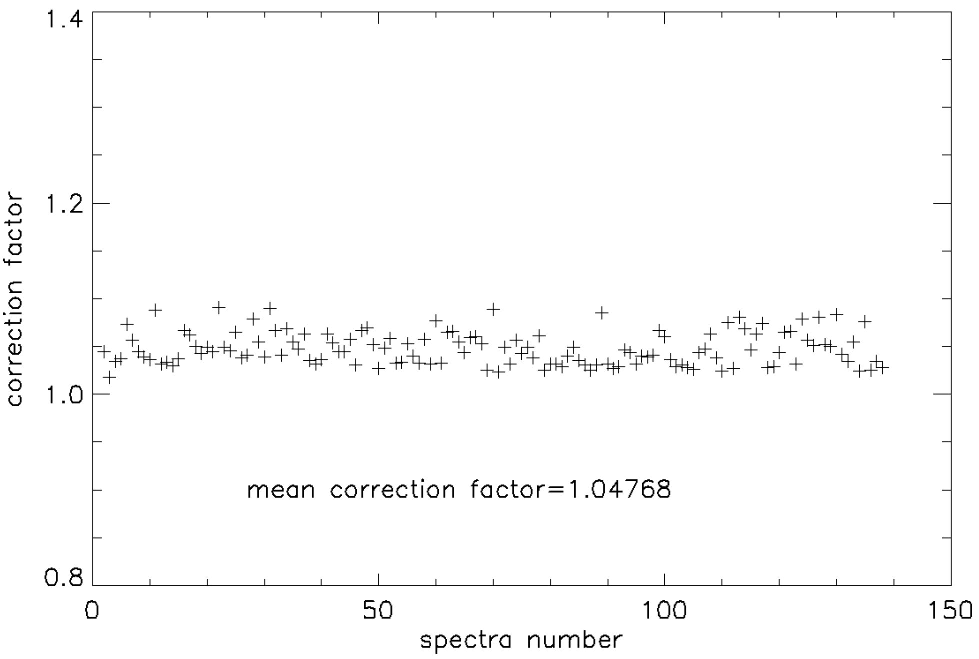

Figure B.2.: Dead time correction factors for all energy deposition spectra measured during MTR-2B. The mean value of these correction factors is 1.048.

per second. This leads to a corrected count rate of 133.5 particles per second. The corrected count rate is 2.7% higher than the uncorrected. An overview of the calculated daily dead time correction factors which were used in chapter 5 are shown in table B.3.

Table B.3.: Daily dead time correction factors for correction of the absorbed dose measured with MTR-DOSTEL for MTR-1 and MTR-2B mission phase.

	MTR-1	MTR-2B
GCR	1.00	1.03
SAA	1.17	1.05

B.2. Dead Time Correction for SAA and Slot Region Belt Crossings

In the September and October data of the MTR-DOSTEL a crossing of an additional so called Slot Region Belt (SRB) could be observed. This can be clearly seen in the count rate distribution of this time period shown in figure 7.2. During the crossings of the SRB the count rates increases up to 10000 particles per second. Due to these high count rates a dead time correction is needed for these data sets. The correction for these data was done the same way as described in the previous section. This time four example days were used:
Day1: 09.25.2004
Day2: 10.04.2004
Day3: 10.06.2004
Day4: 10.07.2004
Two of these days had 7 crossings of SAA and Slot region and the other two days had 8 crossing of these regions. Figure B.3 shows the tracks of SAA and SRB crossings for the example day 3. The upper panel shows the ascending tracks. These tracks are just crossing the SAA region and are used for a comparison with SAA crossings from the time between April and June 2004. The descending tracks are shown in in the lower panel of figure B.3. They are crossing the SAA region and the SRB. The count rates between the SAA and the SRB crossing do not decrease enough (fig. 7.2) to make the DOSTEL switch the mode. It stays in SAA mode. The correction factors for all SAA-mode spectra of example day 3 are shown in table B.4. The correction factors for the descending crossings are higher than for the ascending tracks. This is due to the higher count rates during the crossings of the SRB. The correction factors for the whole example days were calculated the same way as in the previous section.

Table B.4.: Dead time correction factors for the seven radiation belt crossings for October 6th 2004.

Type	1	2	3	4	5	6	7
F_{corr}	1.05	1.26	1.18	1.02	1.90	1.88	1.21

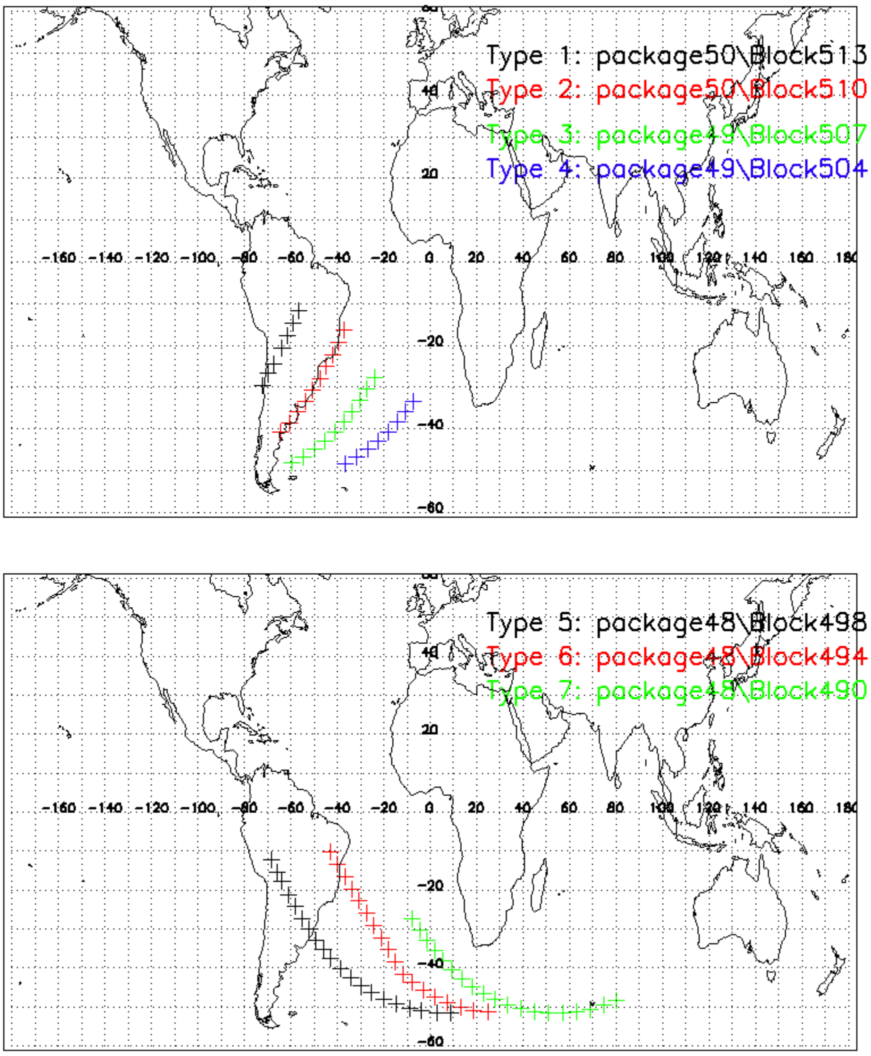

Figure B.3.: Crossings of the inner radiation belt in the SAA region and the crossings of the SRB on example day 3. The upper panel shows the ascending and the lower panel the descending crossings. The tracks and, thus, the belonging spectra are labeled with $type_i$ in the same color code. The ascending crossings should be comparable with the SAA crossings between April and June 2004. For the descending tracks the energy deposition spectra contain particles from SAA and SRB crossings.

The results of the daily correction factors are shown in table B.5. The correction factors are given for the ascending SAA crossings, the descending SAA and SRB crossings and all SAA-mode spectra of the day. Because of the different number of total counts during different crossings, the factor for all spectra is not the mean of ascending and descending spectra. The correction factors for only the ascending SAA crossings are comparable to the results from table B.2.

Table B.5.: Daily dead time correction factors for the four example days of radiation belt crossings in September and October 2004 during MTR-1.

Example day	1	2	3	4
$F_{corr-day}$ ascending	1.12	1.17	1.20	1.18
$F_{corr-day}$ descending	1.52	1.66	1.85	1.39
$F_{corr-day}$ all	1.38	1.45	1.51	1.28

The mean corrected absorbed dose rate for ascending SAA crossing is 166.4 $\frac{\mu Gy}{day}$ for the example day between April and June 2004. For the example day in September and October 2004 the mean absorbed dose rate is 160.4 $\frac{\mu Gy}{day}$ and in good aggreement with the result for the undisturbed conditions between April and May 2004. The mean absorbed dose rate for descending SAA crossings in undisturbed conditions is 122.2 $\frac{\mu Gy}{day}$. The result for the September and October descending crossing is 258.5 $\frac{\mu Gy}{day}$ and has doubled in comparison with the undisturbed conditions. The results for the mean corrected absorbed dose rate for the two time periods are shown in table B.6.

Table B.6.: Mean corrected absorbed dose rates in water for example days of radiation belt crossings during MTR-1 mission phase. Three example days of the undisturbed conditions in LEO between April and June 2004 and four example days during SRB presence from September and October 2004 were used.

	undisturbed conditions April to June 2004	SRB presence September and October 2004
ascending	166.4 $\frac{\mu Gy}{day}$	160.4 $\frac{\mu Gy}{day}$
descending	122.2 $\frac{\mu Gy}{day}$	258.5 $\frac{\mu Gy}{day}$
total	288.6 $\frac{\mu Gy}{day}$	418.9 $\frac{\mu Gy}{day}$

C. Table of time offsets

Table C.1.: This table shows the time offsets for all MTR-1 data files. The time offset here is given in real time offset due to different durations of data download plus -120 minutes time offset due to the transformation to UTC (Coordinated Universal Time).

File name	timedelay/min	File name	timedelay/min
S1000040	-125	S1000116	-115
S1000044	-125	S1000117	-120
S1000047	-129	S1000118	-118
S1000073	-122	S1000120	-118
S1000077	-125	S1000121	-116
S1000080	-124	S1000122	-120
S1000083	-122	S1000123	-118
S1000086	-121	S1000124	-117
S1000089	-119	S1000125	-116
S1000092	-125	S1000126	-120
S1000095	-122	S1000127	-118
S1000098	-122	S1000128	-118
S1000102	-120	S1000129	-117
S1000105	-125	S1000130	-121
S1000108	-122	S1000131	-118
S1000111	-117	S1000132	-118
S1000112	-115	S1000133	-116
S1000113	-120	S1000134	-120
S1000114	-118	S1000135	-119
S1000115	-117	S1000148	-124

File name	timedelay/min	File name	timedelay/min
S1000151	-122	S1000235	-124
S1000154	-120	S1000242	-123
S1000157	-124	S1000245	-123
S1000160	-124	S1000248	-127
S1000163	-124	S1000257	-125
S1000166	-122	S1000260	-127
S1000169	-127	S1000263	-127
S1000172	-118	S1000266	-127
S1000173	-128	S1000269	-124
S1000176	-124	S1000272	-122
S1000179	-123	S1000275	-128
S1000187	-122	S1000278	-126
S1000190	-124	S1000281	-125
S1000198	-122	S1000284	-128
S1000206	-124	S1000287	-126
S1000216	-122	S1000291	-125
S1000219	-124	S1000294	-124
S1000223	-124	S1000297	-128
S1000226	-123	S1000300	-128
S1000229	-124	S1000303	-126

File name	timedelay/min	File name	timedelay/min
S1000306	-124	S1000367	-123
S1000309	-122	S1000369	-118
S1000312	-125	S1000370	-121
S1000315	-125	S1000376	-121
S1000318	-125	S1000382	-118
S1000321	-128	S1000383	-116
S1000324	-129	S1000385	-115
S1000327	-120	S1000386	-117
S1000335	-115	S1000387	-119
S1000336	-119	S1000388	-117
S1000337	-119	S1000389	-115
S1000338	-117	S1000390	-120
S1000339	-115	S1000391	-118
S1000340	-119	S1000392	-116
S1000341	-118	S1000394	-119
S1000342	-118	S1000395	-118
S1000343	-115	S1000396	-116
S1000344	-120	S1000397	-120
S1000345	-117	S1000398	-118
S1000346	-117	S1000399	-119
S1000347	-115	S1000400	-116
S1000365	-119	S1000401	-116

File name	timedelay/min	File name	timedelay/min
S1000402	-119	S1000428	-122
S1000403	-120	S1000429	-120
S1000404	-116	S1000430	-118
S1000405	-115	S1000431	-118
S1000406	-121	S1000432	-121
S1000407	-120	S1000433	-119
S1000408	-118	S1000435	-117
S1000409	-116	S1000436	-117
S1000410	-120	S1000438	-117
S1000411	-118	S1000439	-122
S1000413	-120	S1000440	-120
S1000414	-119	S1000441	-118
S1000415	-116	S1000445	-128
S1000416	-114	S1000457	-125
S1000417	-122	S1000459	-125
S1000418	-118	S1000461	-125
S1000419	-116	S1000469	-125
S1000421	-121	S1000472	-125
S1000422	-119	S1000481	-128
S1000424	-123	S1000483	-128
S1000425	-120	S1000485	-128
S1000426	-118	S1000489	-128
S1000427	-121	S1000504	-130

Danksagung

An dieser Stelle möchte ich mich bei all den lieben Menschen bedanken, die mich tatkräftig bei der Fertigstellung dieser Arbeit unterstützt haben. Mein besonderer Dank gilt dabei...

- Herrn Prof. Dr. Bernd Heber, der mir die Möglichkeit gab an diesem Thema zu arbeiten und jederzeit bereit war über Ergebnisse zu diskutieren.
- Herrn Dr. Sönke Burmeister für die Anregungen und wissenschaftlichen Diskussionen zu dieser Arbeit.
- dem HAMLET Konsortium für die gute Zusammenarbeit im Rahmen des HAMLET Projektes (finanziert von der Europäischen Kommission im Rahmen des Seventh Framework Programme (FP7) und koordiniert vom Zentrum für Luft- und Raumfahrt (DLR) Köln).
- dem SpaceLife Programm für den interdisziplinären Einblick in den Bereich LifeScience. Außerdem möchte ich mich an dieser Stelle bei meinem DLR Betreuer und HAMLET Projekt Manager Herrn Dr. Thomas Berger für die wissenschaftlichen Diskussionen bedanken.
- der gesamten Abteilung der Extraterrestrischen Physik der CAU für das gute und angenehme Arbeitsklima und den vielen Diskussionen zwischen Tür und Angel(n).
- Dr. Bent Ehresmann, Dr. Lauri Panitzsch, Dr. Konstantin Herbst,Dr. Lars Berger und Dr. Thomas Möller für das kritische Durchsehen meiner Arbeit und die vielen guten anregenden Diskussionen.
- meiner Familie für die Unterstützung während des gesamten Studiums.
- und natürlich bei meiner lieben Freundin Lorraine-Carol Eleazar - Du bist mein Lieblingsmensch.

Eidesstattliche Versicherung

Hiermit versichere ich an Eides Statt, dass ich die vorliegende Arbeit abgesehen vom Rat meiner akademischen Lehrer ohne fremde Hilfe und lediglich unter der Verwendung der angegebenen Literatur sowie den bekannten Nachschlagewerken der Naturwissenschaften angefertigt habe, und sie nach Inhalt und Form meine eigene ist. Diese Arbeit ist unter Einhaltung der Regeln guter wissenschaftlicher Praxis entstanden. Des Weiteren versichere ich, dass diese Arbeit weder ganz noch teilweise an anderer Stelle zur Prüfung vorlag. Frühere Promotionsversuche wurden von mir nicht vorgenommen.

Kiel, den

Johannes Labrenz